Theoretical and numerical modelling of the anisotropic behaviour of jointed rocks

By

Changtai Zhou

School of Civil, Environmental & Mining Engineering

The University of Adelaide

This thesis is submitted in fulfilment of the requirements for the degree of

Doctor of philosophy

in the Faculty of Engineering, Computer and Mathematical Sciences

February 2019

Theoretical and numerical modelling of the anisotropic behaviour of jointed rocks

By:

Changtai Zhou

Supervised by:

Associate Professor Chaoshui Xu, Ph.D.,
School of Civil, Environmental & Mining Engineering,
The University of Adelaide
Associate Professor Murat Karakus, Ph.D.,
School of Civil, Environmental & Mining Engineering,
The University of Adelaide
and
Associate Professor Jiayi Shen, Ph.D.,
Institute of Port, Coastal and Offshore Engineering,
Zhejiang University

Thesis submitted in fulfillment of the requirements for the degree of
Doctor of Philosophy

School of Civil, Environmental & Mining Engineering
Faculty of Engineering, Computer and Mathematical Sciences
The University of Adelaide North Terrace, Adelaide, SA 5005, Australia
Email: changtai.zhou@adelaide.edu.au

Table of contents

Abstract

In nature, various forms of rock anisotropy are widely pre-existing discontinuities such as bedding planes, joints, weak layers and cleavages. Rock anisotropic characteristics are in general critical for the stability of surface or underground rock excavations. The goal of this work is to investigate the anisotropic behaviour of jointed rock masses using theoretical and numerical modelling methods. In particular, discrete element modelling using flat jointed bonded particle model (FJM) was used in this research. A systematic micro-parameter calibration method for FJM was proposed first in this work to overcome the limitations of traditional approach, which essentially is a time-consuming tedious trial and error process. The relationships between the FJM micro-parameters and constitutive parameters, as well as macro-mechanical rock properties were first established through dimensionless analysis. Sensitivity and regression analyses were then conducted to quantify their relationships, using results from numerical simulations. The proposed method was demonstrated to be robust and effective based on the macro-mechanical property validation of four different types of rocks. The application of FJM to capture the load rate-dependent mechanical properties of rock materials was investigated. The results were cross-validated with experimental measurements, which indicated that FJM can model the dynamic behaviour of rocks from quasi-static to medium strain rate range. FJM, in combination with smooth joint model (SJM) used to model discontinuities, were then used to study the dynamic behaviour of rocks with a persistent joint at different orientations. A strength prediction model for dynamic UCS of a specimen containing a persistent joint at different orientations were proposed and the coefficients of the proposed equation were quantified based on numerical simulation results. The proposed model was shown to be capable of predicting

the rate-dependent UCS of a jointed rock. Finally, the strength reduction of a jointed rock was further investigated using the statistical damage model approach based on the commonly used Weibull distribution, where the Jaeger's and modified Hoek-Brown failure criteria were incorporated in the derived model. The proposed damage model was validated using published experimental data and numerical simulation results of FJM. Results indicated that parameter m only depends on strain parameter k, which is directly proportional to the increase of the failure strain, while parameter F_0 is indirectly related to the strength of the jointed rock. In addition, joint stiffness can be easily incorporated in the proposed damage model, which has significant influence on the damage variable D, damage evolution rate D_r and rock mass deformation modulus. Outcomes of this research help us to understand better the influences of discontinuities on the mechanical behaviour of jointed rock masses.

Statement of originality

I, Changtai Zhou, certify that this work contains no material which has been accepted for the award of any other degree or diploma in any university or other tertiary institution and, to the best of my knowledge and belief, contains no material previously published or written by another person, except where due reference has been made in the text. In addition, I certify that no part of this work will, in the future, be used in a submission for any other degree or diploma in any university or other tertiary institution without the prior approval of the University of Adelaide and where applicable, any partner institution responsible for the joint-award of this degree.

I give consent to this copy of my thesis, when deposited in the library of the University of Adelaide, being made available for loan and photocopying, subject to the provisions of the Copyright Act 1968.

The author acknowledges that copyright of published works contained within this thesis resides with the copyright holder(s) of those works.

I also give permission for the digital version of my thesis to be made available on the web, via the University's digital research repository, the Library catalogue and also through web search engines, unless permission has been granted by the University to restrict access for a period of time.

Name: Date:17/02/2019

Acknowledgements

First, my sincerest gratitude goes to my supervisors A. Professor Chaoshui Xu, A. Professor Murat Karakus and A. Professor Jiayi Shen, for their invaluable guidance and assistance. This thesis would not have been possible without their generous encouragements and support. I am particularly grateful to A. Professor Chaoshui Xu for providing such an opportunity to pursue my research and guiding me patiently and responsibly. Many thanks go to Murat Karakus for his flexible schedule and encouragement providing a wonderful atmosphere for the academic discussion and collaboration. Many thanks go to Jiayi Shen for his encouragements and sharing his own experience with me.

I am very grateful for the financial support for my PhD from the China Scholarship Council and the University of Adelaide.

I would like to thank Leticia Mooney for her editorial support during the preparation of the first paper.

I would like to thank technical staffs including Glenn Sharrock, Ben Harris, David Wines and Mark Christianson from Itasca Consulting Group for their supports and technical advice on PFC simulations.

I appreciate the discussions with my colleagues at The University of Adelaide: Dr. Xianqun He, Mr Zhihe Wang, Mr Zhongyuan Fu, Mr Can Wang, Mr Yang Liu, Miss. Hang Wang, Mr Rupesh Kumar Verma, Mr Selahattin Akdag and Mr Aminhossein Safarizadeh.

I would like to thank my parents and my siblings for their encouragement and love throughout my PhD research. Finally, I would like to thank my girlfriend and my love, Dr.

Wenhui Liu, for her motivation and love. This research could not have been accomplished without her continuous encouragement and understanding.

List of tables

List of Figures

Chapter 1 Introduction

1.1 Research background

A thorough understanding of mechanical properties and failure behaviours of rock masses is fundamental in rock engineering applications. The knowledge together with local stress conditions are the most critical inputs needed for the design and stability assessment of rock excavations (Zhu and Zhao 2004).

Rock anisotropy is an important feature generally associated with rock masses. The anisotropy is caused by different planes of weaknesses such as fractures/joints, bedding planes, layering and stratifications (Shea and Kronenberg 1993). Studies have shown that the rock anisotropy plays a vital role in analyses such as the evaluation of the damage zone in deep underground excavations (Jia et al. 2012), coal pillar stability (Gao 2013), borehole stability in sedimentary rocks (Gaede et al., 2012), exploitation of shale gas (Harris et al., 2011). In particular, large and persistent discontinuities could critically affect the stability of surface or underground rock structures such as slopes and caverns (Hudson and Harrison 2000; Jia et al. 2012; Kostić 2017). Kostić (2017) stated that failure through large fracture planes is the dominant failure mechanism in rock slopes in civil and mining engineering. The main focus of this research is to investigate the anisotropic behaviours of a rock mass containing a single persistent discontinuity under both static and dynamic loading conditions. The rock mass model considered is simplistic, but a comprehensive understanding of such a simple case will be able to help build more sophisticated rock mass models more closely resembling the reality.

Many experimental studies have been published on the strength of anisotropic rock masses (Bagheripour and Mostyn 1996; Yasar 2001; Maji and Sitharam 2012; Wasantha et al. 2013; Moomivand 2014; Jin et al. 2016), which is normally represented using the ratio of the failure strength to the minimum failure strength (R_c) of all cases (Saroglou and Tsiambaos 2008). These results indicated that the mechanical behaviours such as deformation, strength and failure modes are largely influenced by the principal loading direction in relation to the weakness orientation, as well as the confining pressure (Jaeger 1959, 1960). Three failure modes are normally observed in experiments (Tien and Tsao 2000): sliding mode (along the discontinuity or joint), shearing mode (along the intact rock) and mixed mode. The failure mode can be further influenced by the confining pressure (Wasantha et al. 2014). These experimental results provide some very useful data for further theoretical studies, numerical modelling analysis and field applications.

However, experimental tests are always limited due to cost, time and availability of different rock samples. In addition, the results may also be biased towards a particular type of rock and are difficult to generalise (Shen and Karakus 2014; Jiang et al. 2016). Numerical modelling offers an alternative flexible approach. It provides a general platform for the studies of rock mechanical behaviours of any type of rocks at any scale as long as a representative numerical model can be constructed. Numerical modelling can be roughly classified into two groups: continuum method and discontiuum method (Jing and Hudson 2002; Jing 2003; Owen et al. 2007; Lisjak and Grasselli 2014). More recently, one of the dicontinuum method, namely the bonded particle model (BPM), has been favoured by many researchers as it can explicitly present the weakness structures in rock masses together with the micro-structure of the rocks (Mas Ivars et al. 2011; Potyondy 2012; Poulsen et al. 2015; Vallejos et al. 2016; Wu and Xu 2016; Mehranpour and Kulatilake 2017). There are already

no shortage of published works using BPMs to investigate the failure mechanism and behaviours of rock masses (Tang et al. 2006; Zhang et al. 2011, 2017; Ghazvinian et al. 2012; Duan and Kwok 2015; Jiang et al. 2015; Duan 2016; Wang et al. 2017). However, the tedious and time-consuming calibration process required for BPM poses a significant restriction on the wide spread of the application of BPM (Huang 1999; Huang et al. 2013; He 2015; He and Xu 2015). Therefore, there is a need to develop a novel calibration procedure that can simplify the calibration process and the derivation of micro-mechanical parameters for BPM.

Rock mass dynamic properties are attracting more and more attentions as rock excavations get deeper below the surface. Majority of the researches on rock dynamic behaviours focus on the studies of intact rock. However, in engineering applications, rock masses with discontinuities have to be dealt with and the discontinuities normally have the critical influences on the dynamic behaviours of excavations. Investigations on the dynamic properties of rocks containing discontinuities/fractures are still very limited based on the literature review. Therefore, there is a need to study the rock mass mechanical behaviours in response to different strain rates corresponding to different dynamic activities (Cadoni 2010). For intact rocks, previous studies demonstrated that the mechanical properties such as strength (Doan and Billi 2011), elastic modulus (Brace and Jones 1971) and fracture toughness (Kim and Chao 2007; Feng et al. 2017) are positively correlated with the strain rate. No publications have been found in the literature for similar studies on the anisotropic behaviours of rock masses. However, this knowledge is needed to help the stability assessment of deep underground rock excavations when a dynamic failure such as rock burst needs to be considered.

BPM provides an excellent platform to investigate the failure mechanism of the anisotropic rock mass (Ghazvinian et al. 2012), but it still can be time-consuming particularly when the number of particles is significantly large in order to model field applications (Jing 2003). A different simpler approach to model the rock anisotropic behaviours is the statistical damage model, which has been used by many researchers for different applications (Tang et al. 1998; Cao et al. 2010, 2018; Deng and Gu 2011; Li et al. 2012; Liu and Yuan 2015). Previous damage models cover many complex mechanical responses such as strain softening (Li et al. 2012), residual strength (Zhao et al. 2016), dynamic (Liu et al. 2015), hydraulic (Zhang et al. 2016) and thermal damage (Yu et al. 2015; Peng et al. 2016; Xu and Karakus 2018). But no works have been done to investigate the rock anisotropic characteristics using statistical damage model. Therefore, the development of such a statistical damage model for anisotropic rock masses considering joint orientations will be very useful.

1.2 Research objectives

The overall goal of this thesis is to model the anisotropic characterisation of a jointed rock mass using theoretical analysis and numerical simulation. In particular, the following objectives are derived based on the literature review:

Objective 1: To develop a systematic approach to simplify the calibration procedure for bonded particle numerical modelling. The proposed calibration procedure will avoid the tedious and time-consuming micro-parameter derivation process of BPMs. BPM will also be the numerical modelling tool used in this research for the studies of other topics.

Objective 2: To establish a BPM that can simulate the mechanical behaviours of rocks containing one persistent joint. The model is to be cross-validated by published

experimental results. The validated BPM will then be used to investigate the effect of the persistent joint on the rate-dependent mechanical properties of jointed rock masses.

Objective 3: Based on the simulation results from BPMs, to propose a dynamic failure criterion for rocks containing a single persistent joint, considering different joint orientations.

Objective 4: To propose a new statistical damage model for anisotropic rock masses, taking into account the effects of joint orientations on the failure behaviours. The model will be verified and validated using both BPM modelling results and experimental data.

1.3 Thesis structure

This thesis has 6 chapters. The main body of the thesis is a literature review followed by three journal publications arising from the research. Chapter 6 presents the conclusions from the research and the recommendations for future works.

Chapter 2 provides a comprehensive review of works relevant to this study, i.e., theoretical studies, experimental investigations and numerical modelling related to the static and dynamic behaviours of anisotropic rocks. Statistical rock damage models are also reviewed. The merits and limitations of existing studies are discussed within the context of the current research.

Chapter 3 presents a systematic approach to simplify the calibration procedure for a flat-joint bonded-particle model (BPM). The initial relationships between the microscopic, constitutive parameters and macro-rock properties are determined through dimensionless analysis. Sensitivity analyses and regression analyses are then conducted to quantify the relationships using numerical results. Four BPMs for four different types of rocks are used to demonstrate the effectiveness and the robustness of the proposed approach.

Chapter 4 presents the study of rate-dependent mechanical properties of rocks with a pre-existing persistent joint at different orientations. BPM is used as the numerical tool for this study and the constructed model is validated using published experimental results. A dynamic failure strength model considering joint orientations and strain rates is proposed based on Jaeger's criterion. The proposed model is then validated using an extensive set of BPM simulations by conducting numerical UCS tests on the numerical models at different dynamic loading rates. The failure characteristics of the specimens at different strain rates are also discussed.

In Chapter 5, a new statistical damage model is proposed for jointed rock masses using the Weibull distribution which takes into account the joint orientations by incorporating the Jaeger's and modified Hoek-Brown failure criteria. The proposed damage model is verified and validated using BPM simulations and published experimental results.

Chapter 6 summarises the major contributions of this research and some recommendations for future works in this research area. The future work to advance the current research is also discussed.

References

Bagheripour MH, Mostyn G (1996) Prediction of the strength of jointed rock - Theory and practice. In: ISRM International Symposium-EUROCK 96. International Society for Rock Mechanics and rock engineering. Torino, Italy; p. 231-8.

Brace WF, Jones AH (1971) Comparison of uniaxial deformation in shock and static loading of three rocks. J Geophys Res 76:4913–4921

Cadoni E (2010) Dynamic characterization of orthogneiss rock subjected to intermediate and high strain rates in tension. Rock Mech Rock Eng 43:667–676

Cao W, Tan X, Zhang C, He M (2018) A constitutive model to simulate the full deformation and failure process for rocks considering initial compression and residual strength behaviors. Can Geotech J 54:1–51

Cao W, Zhao H, Li X, Zhang Y (2010) Statistical damage model with strain softening and hardening for rocks under the influence of voids and volume changes. Can Geotech J 47:857–871

Deng J, Gu D (2011) On a statistical damage constitutive model for rock materials. Comput Geosci 37:122–128

Doan ML, Billi A (2011) High strain rate damage of Carrara marble. Geophys Res Lett 38:

Duan K (2016) Micromechanical modeling of inherently anisotropic rock and its application in borehole breakout analyses (Doctoral dissertation). The University of Hong Kong

Duan K, Kwok CY (2015) Discrete element modeling of anisotropic rock under Brazilian test conditions. Int J Rock Mech Min Sci 78:46–56

Feng P, Ayatollahi MR, Dai F, Xu NW, Wei MD (2017) DEM investigation on fracture mechanism of the CCNSCB specimen under intermediate dynamic loading. Arab J Geosci 10:48

Gao F (2013) Simulation of Failure Mechanisms around Underground Coal Mine Openings Using Discrete Element Modelling (Doctoral dissertation). Simon Fraser University

Ghazvinian A, Sarfarazi V, Schubert W, Blumel M (2012) A study of the failure mechanism of planar non-persistent open joints using PFC2D. Rock Mech Rock Eng 45:677–693

He X (2015) Failure Mode Transition for Rock Cutting: Theoretical, Numerical and Experimental Modelling (Doctoral dissertation). The University of Adelaide

He X, Xu C (2015) Discrete element modelling of rock cutting: from ductile to brittle transition. Int J Numer Anal Methods Geomech 39:1331–1351

Huang H (1999) Discrete element modeling of tool-rock interaction (Doctoral dissertation). The University of Minnesota.

Huang H, Lecampion B, Detournay E (2013) Discrete element modeling of tool-rock interaction I: Rock cutting. Int J Numer Anal Methods Geomech 37:1913–1929

Hudson JA, Harrison JP (2000) Engineering rock mechanics: an introduction to the principles. Oxford; New York, Elsevier.

Jaeger JC (1959) The frictional properties of joints in rock. Pure Appl Geophys 43:148–158

Jaeger JC (1960) Shear failure of anisotropic rocks. Geol Mag 97:65–72

Jia P, Yang TH, Yu QL (2012) Mechanism of parallel fractures around deep underground excavations. Theor Appl Fract Mech 61:57–65

Jiang C, Zhao GF, Zhu J, Zhao YX, Shen L (2016) Investigation of Dynamic Crack Coalescence Using a Gypsum-Like 3D Printing Material. Rock Mech Rock Eng 49:3983–3998

Jiang M, Jiang T, Crosta GB, Shi Z, Chen H, Zhang N (2015) Modeling failure of jointed rock slope with two main joint sets using a novel DEM bond contact model. Eng Geol 193:79–96

Jin C, Li S, Liu J (2016) Anisotropic mechanical behaviors of columnar jointed basalt under compression. Bull Eng Geol Environ 77:1–14

Jing L (2003) A review of techniques, advances and outstanding issues in numerical modelling for rock mechanics and rock engineering. Int J Rock Mech Min Sci 40:283–353

Jing L, Hudson JA (2002) Numerical methods in rock mechanics. Int J Rock Mech Min Sci 39:409–427

Kim Y, Chao YJ (2007) Effect of loading rate on dynamic fracture initiation toughness of brittle materials. Int J Fract 145:195–204

Kostić S (2017) Analytical Models for Estimation of Slope Stability in Homogeneous Intact and Jointed Rock Masses with a Single Joint. Int J Geomech 17:04017089

Li X, Cao W, Su Y (2012) A statistical damage constitutive model for softening behavior of rocks. Eng Geol 143–144:1–17

Lisjak A., Grasselli G (2014) A review of discrete modeling techniques for fracturing processes in discontinuous rock masses. J Rock Mech Geotech Eng J 6:301–314

Liu H, Yuan X (2015) A damage constitutive model for rock mass with persistent joints considering joint shear strength. Can Geotech J 52:1136–1143

Liu HY, Lv SR, Zhang LM, Yuan XP (2015) A dynamic damage constitutive model for a rock mass with non-persistent joints under uniaxial compression. Int J Rock Mech Min Sci 75:132–139

Maji VB, Sitharam TG (2012) Testing and evaluation of strength and deformation behaviour of jointed rocks. Geomech Geoengin 7:149–158

Ivars DM, Pierce ME, Darcel C, Reyes-Montes J, Potyondy DO, Young RP, Cundall PA (2011) The synthetic rock mass approach for jointed rock mass modelling. Int J Rock Mech Min Sci 48:219–244

Mehranpour MH, Kulatilake PHSW (2017) Improvements for the smooth joint contact model of the particle flow code and its applications. Comput Geotech 87:163–177

Moomivand H (2014) Effects of orientation, frequency, and number of sets of discontinuities on rock strength under triaxial stresses. Arab J Geosci 7:5345–5352

Owen DRJ, Coggan JS, Rance JM, Pine RJ (2007) A new discrete fracture modelling approach for rock masses. Géotechnique 57:757–766

Peng J, Rong G, Cai M, Yao MD, Zhou CB (2016) Physical and mechanical behaviors of a thermal-damaged coarse marble under uniaxial compression. Eng Geol 200:88–93

Potyondy DO (2012) A flat-jointed bonded-particle material for hard rock. In: 46th US Rock mechanics/geomechanics symposium. American Rock Mechanics Association

Poulsen BA, Adhikary DP, Elmouttie MK, Wilkins A (2015) Convergence of synthetic rock mass modelling and the Hoek-Brown strength criterion. Int J Rock Mech Min Sci 80:171–180

Saroglou H, Tsiambaos G (2008) A modified Hoek-Brown failure criterion for anisotropic intact rock. Int J Rock Mech Min Sci 45:223–234

Shea WT, Kronenberg AK (1993) Strength and anisotropy of foliated rocks with varied mica contents. J Struct Geol 15:1097–1121

Shen J, Karakus M (2014) Simplified method for estimating the Hoek-Brown constant for intact rocks. J Geotech Geoenvironmental Eng 140:04014025

Tang CA, Yang WT, Fu YF, Xu XH (1998) A new approach to numerical method of modelling geological processes and rock engineering problems-continuum to discontinuum and linearity to nonlinearity. Eng Geol 49:207–214

Tang CA, Zhang YB, Liang ZZ, Xu T, Tham LG, Lindqvist PA, Kou SQ, Liu HY (2006) Fracture spacing in layered materials and pattern transition from parallel to polygonal fractures. Phys Rev E - Stat Nonlinear, Soft Matter Phys 73:1–9

Tien YM, Tsao PF (2000) Preparation and mechanical properties of artificial transversely isotropic rock. Int J Rock Mech Min Sci 37:1001–1012

Vallejos JA, Salinas JM, Delonca A, Mas Ivars D (2016) Calibration and verification of two bonded-particle models for simulation of intact rock behavior. Int J Geomech 17:06016030

Wang P, Ren F, Miao S, Cai M, Yang T (2017) Evaluation of the anisotropy and directionality of a jointed rock mass under numerical direct shear tests. Eng Geol 225:29–41

Wasantha PLP, Ranjith PG, Viete DR (2013) Specimen slenderness and the influence of joint orientation on the uniaxial compressive strength of singly jointed rock. J Mater Civ Eng 26:2–5

Wasantha PLP, Ranjith PG, Viete DR (2014) Effect of joint orientation on the hydromechanical behavior of singly jointed sandstone experiencing undrained loading. J Geophys Res Solid Earth 119:1701–1717

Wu S, Xu X (2016) A study of three intrinsic problems of the classic discrete element method using flat-joint model. Rock Mech Rock Eng 49:1813–1830

Xu XL, Karakus M (2018) A coupled thermo-mechanical damage model for granite. Int J Rock Mech Min Sci 103:195–204

Yasar E (2001) Failure and failure theories for anisotropic rocks. 17th Int Min Congr Exhib Turkey-IMCET 417–424

Yu QL, Ranjith PG, Liu HY, Yang TH, Tang SB, Tang CA, Yang SQ (2015) A Mesostructure-based Damage Model for Thermal Cracking Analysis and Application in Granite at Elevated Temperatures. Rock Mech Rock Eng 48:2263–2282

Zhang N, Li X, Cheng H, Teng T (2016) A coupled damage-hydro-mechanical model for gas drainage in low-permeability coalbeds. J Nat Gas Sci Eng 35:1032–1043

Zhang Q, Zhu H, Zhang L, Ding X (2011) Study of scale effect on intact rock strength using particle flow modeling. Int J Rock Mech Min Sci 48:1320–1328

Zhang X, Zhang Q, Wu S (2017) Acoustic emission characteristics of the rock-like material containing a single flaw under different compressive loading rates. Comput Geotech 83:83–97

Zhao H, Shi C, Zhao M, Li X (2016) Statistical Damage Constitutive Model for Rocks Considering Residual Strength. Int J Geomech 16:1–9

Zhu W, Zhao J (2004) Stability Analysis and Modelling of Underground Excavations in Fractured Rocks. Amsterdam, Elsevier.

Chapter 2 Literature review

Rock anisotropy caused by different planes of weaknesses such as fractures/joints, bedding planes, layering, and stratifications (Shea and Kronenberg 1993) is a fundamental issue for rock engineering applications (Gao 2013). Published experimental results of anisotropic rock masses indicated that mechanical behaviours such as deformation, strength, and failure modes are largely influenced by loading direction relative to weakness orientation (Jaeger 1959, 1960) together with confining pressure.

Although experimental results provide some very useful data for further theoretical studies, numerical modelling analysis, and field applications, results may be limited due to cost, experimental run-time, and bias towards a particular type of rock (Shen and Karakus 2014; Jiang et al. 2016). On the other hand, numerical modelling provides a general platform to investigate the mechanical behaviours of any type of rocks at any scale. The bonded particle model (BPM) has been favoured by many researchers as it can explicitly present the weakness structures in rock masses together with the micro-structure of the rocks (Mas Ivars et al. 2011). However, the tedious and time-consuming calibration process required for BPM significantly limits the wide-spread application of BPM.

In addition, the dynamic properties of rock masses are attracting more and more attention as rock excavations proceed deeper below the surface. To date, the majority of research on rock dynamic behaviour focuses on studies of intact rock. A review of the current literature reveals that investigations on the dynamic properties of rocks containing discontinuities/fractures are still very limited.

BPM provides an excellent platform to investigate the failure mechanisms of anisotropic rock masses but can still be time-consuming, particularly when the number of particles is significantly large for field applications (Jing 2003). The model within the framework of the statistical damage model (SDM) provides a different simpler approach to modelling rock anisotropic behaviours.

In this chapter, a comprehensive critical review of works relevant to these three topics are conducted. The merits and limitations of existing studies are discussed within the context of the current research.

2.1 Intact rock simulation using the flat joint model (FJM)

The discrete element method (DEM) has become a powerful planform for a variety of numerical modelling applications in soil mechanics, fluid mechanics and rock mechanics. The basic idea of DEM is that the material can be represented by an assembly of deformable or rigid particles or blocks, interacting through contacts by proper constitutive models. This representation leads to three fundamental issues in rock mechanics modelling (Jing 2003):

(a) Identification of suitable particle or block shapes and sizes, as well as the system topology for practical engineering applications;
(b) Formulation and solution of the motion equations for the particle or block system;
(c) Recognition and updating of the contacts between particles or blocks due to deformations and motions of particles or blocks.

In DEM, the interaction between particles or blocks is regarded as a dynamic process that will eventually approach an equilibrium state. During this process, the motion calculations are performed on particles or blocks following Newton's second law and the contact forces are evaluated following the pre-defined contact constitutive law, see Fig. 2.1. The dynamic behaviour is represented numerically by a time-marching approach based on a dynamic or

static relaxation scheme where the velocity and acceleration are assumed to be constant in each time step.

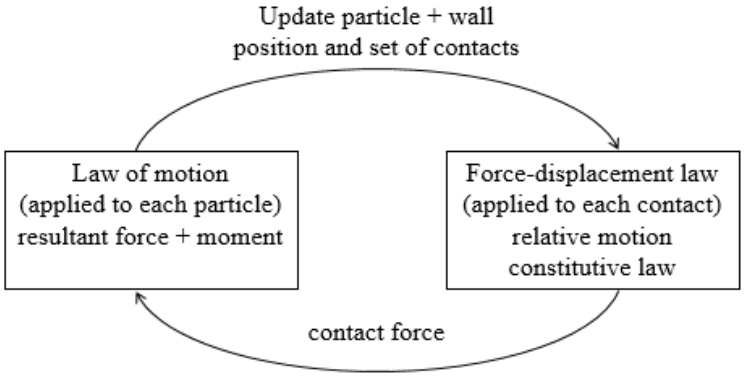

Figure 2.1 The calculation cycle for Discrete Element Method (After Itasca Consulting Group Inc 2014)

The explicit DEM is divided into two groups: block-based model and particle-based model. The most representative block-based model is the universal distinct element code (UDEC). In UDEC, the media is discretised into an assemblage of discrete blocks interacting with each other through discontinuity interfaces. The contacts between blocks at discontinuity interfaces in UDEC are treated as boundaries, and therefore mechanical behaviours can be achieved by assigning mechanical parameters, such as normal stiffness, shear stiffness, friction angle, cohesion and tensile strength. However, this approach in general has difficulty in modelling non-persistence fractures as discrete blocks within the model must be convex. This limitation makes it difficult to incorporate more realistic fracture systems in the model.

For particle-based models, the most notable implementations include particle flow code (PFC), Yade, EDEM, Smoothed Discrete Element Method (SDEM), LIGGGHTS, MechSys and Distinct Lattice Spring Model (DLSM). However, most open source DEM codes have difficulty in modelling rock discontinuities, particularly fracture systems.

Therefore, PFC incorporating discrete fracture network (DFN) with different contact models is used as the numerical tool for this study.

It was first proposed to simulate mechanical behaviours of non-cohesive media like soils and sands using an assembly of particles with varying diameters interacting with each other through physical contact (Cundall and Strack 1979). The movement of these particles follows Newton's laws of motion while the interaction at contacts is determined by the normal stiffness, shear stiffness, and friction coefficient. Contact forces arise when two particles come into contact and can be resolved into normal and shear components at the contact point (Fig. 2.2). The normal force and shear force can be calculated by:

$$F_n = k_n u_n \tag{2.1}$$

$$\Delta F_s = -k_s \Delta u_s \tag{2.2}$$

where k_n and k_s are the normal and shear stiffness of the contact, u_n is the overlap between two particles, and Δu_s is shear displacement increment.

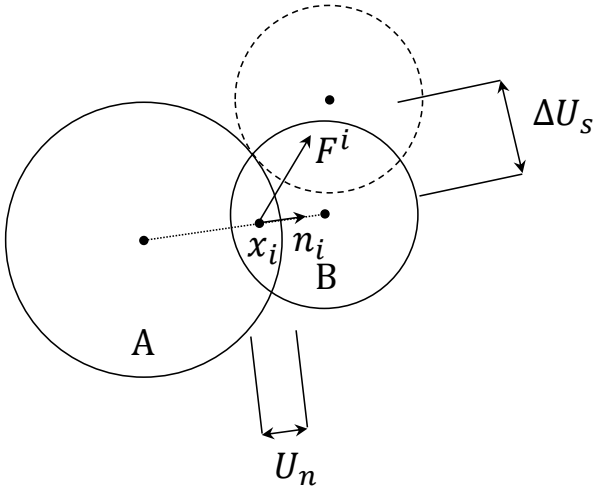

Figure 2.2 Force-displacement behaviour at a contact between two particles. Modified after Potyondy and Cundall (2004)

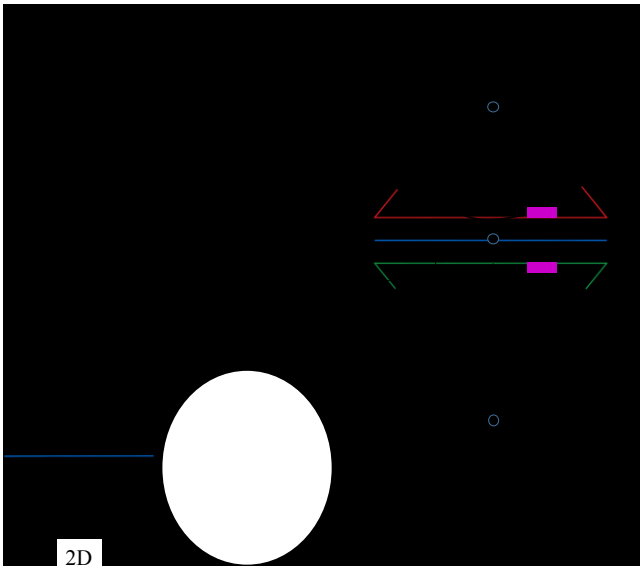

Figure 2.3 A typical schematic diagram of the FJM (Potyondy 2012)

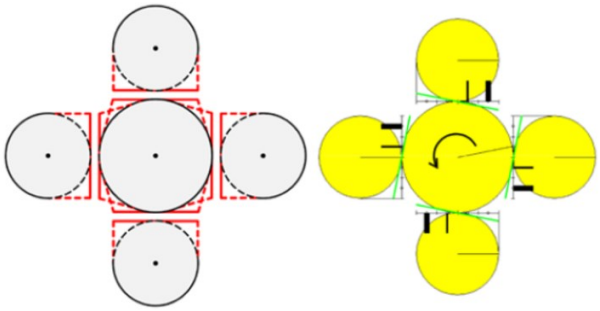

Figure 2.4 Interface geometry of four un-bonded flat joint contacts (left). Surrounding particles resist the central particle rotation through un-bonded interfaces (right) (Potyondy 2012)

To simulate a brittle solid material, Potyondy and Cundall (2004) extended the cohesionless model to the BPM in order to examine crack nucleation and fracture propagation. Three types of contact models, i.e., contact bond model (CBM), parallel bond model (PBM), and flat joint model (FJM), are implemented in the commonly used particle-based modelling tool, particle flow code (PFC). Among them, the most widely used are PBM and FJM (Vallejos et al. 2016). Although the PBM can simulate various mechanical responses including elasticity (Schöpfer et al. 2007), fracturing (Farahmand et al. 2015), damage zone

(Fakhimi and Villegas 2007), rock cutting (Huang et al. 2013; He and Xu 2015), and crack initiation process (Zhang and Wong 2012), it suffers from three intrinsic problems: the unrealistic ratio of uniaxial compressive strength (UCS) to tensile strength (TS), unrealistic low internal friction angle, and unrealistic linear failure envelope (Potyondy and Cundall 2004; Cho et al. 2007; Schöpfer et al. 2007; Vallejos et al. 2013; Wu and Xu 2016). To overcome these limitations in PBM, Potyondy (2012) introduced a grain-based model, the FJM, with a fictitious notional contact surface (Fig. 2.3). This fictitious notional surface can increase the ratio of UCS to TS by grain interlocking, which reflects rock behaviour more realistically at the micro-scale and is more advantageous compared to other bonded particle models. Additionally, it is worthwhile to note that for the FJM, the interface may evolve from a fully bonded state to a fully un-bonded and frictional state; however, the fully un-bonded interface is not removed during the simulation, so the interface will continue to resist relative rotation (Fig. 2.4).

Table 2.1 Comparison between PBM and FJM, modified after Wu and Xu (2016).

		PBM	FJM
Similarities	Interface	Finite-length	Finite-length
	Model	Bond models	Bond models
Differences	Bond	Bonded across the entire length	Bonded or unbonded in the initial stage
	Rotation resistance	Moment contribution to stress	Its special structure
	Deformation	Deformable and breakable	Deformable, partial damage, breakable
	Breaking	Entire interface breaks	Elements break
	Interface	Interface vanishes after breaking	Interface still exists after breaking
	Post-peak behaviour	Cannot resist rotation after breaking	Can resist rotation after breaking

The similarities and differences between PBM and FJM in terms of micro-structures and micro-parameters are summarized in Table 2.1. Compared with PBM, the FJM was found

to better capture the failure envelope of rocks in the laboratory and was recommended by Vallejos et al. (2016).

Within the FJM, each element with a force (F^e) and a moment (M^e) acting at the contact location on the equal and opposite notional surfaces obeys the force-displacement law. The normal force (F_n^e) and moment (M^e) can be updated in the normal direction, and the shear force (F_s^e) can be calculated in the tangent direction. Therefore, the element normal stress and shear stress are given by:

$$\sigma^e = \frac{F_n^e}{A^e} \tag{2.3}$$

$$\tau^e = \frac{F_s^e}{A^e} \tag{2.4}$$

where A^e is the element area which equals to its length in 2D.

FJM bonded elements and unbonded elements have distinctive mechanical behaviours governed by microscopic parameters. The strength envelope of bonded elements is shown in Fig. 2.5.

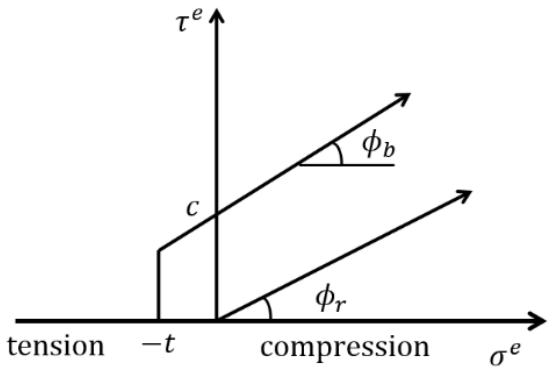

Figure 2.5 Failure envelopes for bonded elements and unbonded elements (Labuz and Zang 2012)

Under tension, bonded elements are sustained by the tensile strength of the bonds until the tensile stress exceeds the critical value, at which point the bonded element becomes an unbonded element and forms a micro-tensile crack. Under compression, FJM bonded elements and unbonded elements follow the Mohr-Coulomb (MC) criterion with a tension cut-off and the Coulomb sliding criterion, respectively:

$$\tau^e = c_b + \sigma^e tan\phi_b \tag{2.5}$$

$$\tau^e = \sigma^e tan\phi_r \tag{2.6}$$

where c_b is the bond cohesion; ϕ_b and ϕ_r are local friction angle and residual friction angle, respectively. Bonded elements will form a micro-shear crack when the shear strength of the bond is exceeded.

For element elasticity representation, the commonly used deformability method is employed to define contact model properties in the latest version of PFC. In this approach, contact elastic deformable properties such as k_n and k_s are not specified directly, rather the k_n and k_s of contacts are modified in the programme simultaneously so the specified effective modulus (E^*) and stiffness ratio (k^*) defined through the deformability method are matched. The relationships between the E^*, k^*, and contact parameters can be expressed as:

$$E^* = k_n L \tag{2.7}$$

$$k^* = \frac{k_n}{k_s} \tag{2.8}$$

where $L = \{R^1 + R^2,$ for ball-ball contacts; *or* $R^1,$ for ball-facet contacts$\}$, in which R^1 and R^2 are radii of the particles interacting in ball-ball or ball-facet contacts. In this research, the deformability method is used.

The above-mentioned background theory demonstrates the formulation of the FJM model, assisting us to understand the macro-behaviours of BPM from a micro-perspective. As expected, micro-mechanical and constitutive parameters between particles, boundary

conditions (e.g. the size of a BPM specimen and loading rate), the micro-structure, and geometrical parameters of particles can all influence the macro-mechanical behaviour of the numerical specimen (He and Xu 2015). In particular, parameters required for FJM can be divided into three groups: boundary conditions, micro-structure and geometrical parameters, and micro-mechanical and constitutive parameters between particles, as shown in Table 2.2.

Table 2.2 Parameters required for FJM

Groups	Parameters	Symbol	Unit	Base unit
Boundary condition parameters	Specimen width	w	mm	L
	Specimen height	l	mm	L
	Loading rate	V	m/s	$L \cdot T^{-1}$
Micro-structures and geometrical parameters	Ratio of maximum to minimum ball radius	r_{max}/r_{min}	[-]	[-]
	Ratio of specimen width to the median ball diameter	w/d	[-]	[-]
	Bond surface gap	g_0	m	L
	Porosity of the synthetic the numerical specimen	n	[-]	[-]
	Number of elements in each bond	N_r	[-]	[-]
Micro-mechanical and constitutive parameters	Effective modulus of bond	E^*	GPa	$F \cdot L^{-2}$
	Stiffness ratio of contact	k^*	[-]	[-]
	Tensile strength of contact	t	MPa	$F \cdot L^{-2}$
	Cohesion of bond	c	MPa	$F \cdot L^{-2}$
	Friction angle of bond	ϕ_b	°	[-]
	Residual friction coefficient of bond	μ	[-]	[-]

Note: [*F, L, T*] represent the primary dimension of force, length and time respectively.

Table 2.3 Summary of calibration methods for BPMs

References	Dimensions	Bond model	Calibration method
(Huang 1999)	2D	CBM	The dimensionless method
(Potyondy and Cundall 2004)	2/3D	CBM	The trial-and-error method
(Yoon 2007)	2D	CBM	The statistical CCD method
(Fakhimi and Villegas 2007)	2D	CBM	The dimensionless method
(Tawadrous et al. 2009)	3D	CBM	The artificial neural networks
(Wang and Tonon 2010)	3D	CBM	The SNOBFIT method
(Yang et al. 2006)	2D	PBM	The dimensionless method
(Sun et al. 2013)	3D	PBM	The artificial neural networks
(Chehreghani et al. 2017)	3D	PBM	The response surface method
(Itasca Consulting Group Inc 2014)	2D	PBM, FJM	The trial-and-error method
(Chen 2017)	2D	FJM	The trial-and-error method
(Castro-Filgueira et al. 2017)	3D	FJM	The trial-and-error method
(Shu et al. 2018)	3D	FJM	The trial-and-error method

Note: SNOBFIT: stable noisy optimization by branch and fit; CCD: central composite design.

Despite the successful applications of simulating complex mechanical rock behaviours using BPMs, the calibration procedure is still a challenge for researchers as there are no direct relationships between BPM micro-parameters, especially for FJM, and rock macro-properties to be modelled. Numerous studies have attempted to simplify the calibration procedure for different BPMs (Table 2.3). Currently, the trial-and-error method is still widely used for calibration of all BPMs (Potyondy and Cundall 2004; Itasca Consulting Group Inc 2014), which can be tedious and time-consuming (He and Xu 2015). A dimensionless method proposed by Huang (1999) was proven to be capable of simplifying the calibration procedure for CBM and PBM (Yang et al. 2006). For these two contact models, optimization methods such as the artificial neural networks method and response surface method were employed in the calibration procedure. However, for FJM, very

limited studies (Castro-Filgueira et al. 2017; Chen 2017; Shu et al. 2018) have been published using the trial-and-error method to derive the relationships between micro-parameters and the macro-rock properties to be modelled. Without these quantitative relationships, it remains a challenging task to derive a set of micro-parameters in the FJM for the desired macro-rock properties. Apparently, there is a need to develop a novel calibration procedure for the FJM, which is expected to be different compared to those for the CBM and PBM due to different mechanism and parameters involved (Potyondy 2012; Vallejos et al. 2016).

2.2 Anisotropic rock mass simulation using the smooth joint model (SJM)

Anisotropic characteristics of rock masses are mainly the result of the sliding behaviour along joint faces. Many techniques using BPMs have been proposed to simulate and capture the sliding behaviours of anisotropic rock masses (Cundall 2000; Mas Ivars et al. 2008; Park and Song 2009)(Fig. 2.6). Descriptions of these methods together with their advantages and disadvantages are summarized in Table 2.4. In order to evaluate these approaches in rock mass modelling, Chiu et al. (2013) compared the strength and deformability of jointed rock masses using these models. Their results indicated that the bond-elimination model overestimated the strength of the jointed rock mass in the sliding mode. Although the band-elimination model can reflect the strength reduction in the sliding mode, it slightly overestimates the failure strength and cannot simulate sliding failure behaviours of jointed rock masses. The overestimated strength of these two models mainly results from the roughness caused by the particle arrangement on the joint face. On the other hand, the SJM (SJM) can produce results in good agreement with experiments (Chiu et al.

2013). Clearly, the SJM provides an effective tool for simulating the anisotropic characteristics of jointed rock masses.

Table 2.4 The comparison study of joint behaviour by Chiu et al. (2013)

Models	Description	Comments	References
Bond-elimination model	Elimination of bonds intersected by the joint plane	Easy implementation, but the joint face may have undesirable roughness	(Cundall 2000)
Band-elimination model	Elimination of bonds and particles within a band defined by the joint plane	Joint face roughness is less an issue, but the band can be different from the actual joint and it is difficult to control the behaviour in the normal direction	(Park and Song 2009)
Smooth-joint model	Replacement of contact models with the smooth-joint model on the joint plane	Elimination of joint face roughness, which is also its weakness as it cannot model joint roughness explicitly or geometry variation	(Mas Ivars et al. 2008)

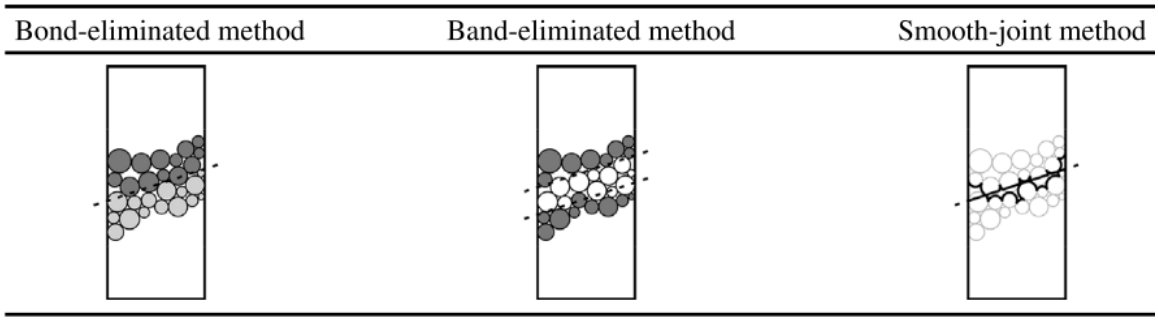

Figure 2.6 The comparison of different techniques in BPM to model rock joints (Chiu et al. 2013)

The concept of SJM was firstly proposed by Mas Ivars et al. (2008) and further developed by Mas Ivars et al. (2011) to simulate jointed rock masses. Unlike the flat joint contact model, the interface in SJM does not resist the relative rotation of particles (Figure 2.7). Therefore, the two particles using the SJM may slide past each other instead of moving around each other. A SJM can be inserted into a linear bond contact model, linear parallel bond contact model, or flat joint contact model to simulate fracture behaviour within a rock mass. The combination of FJM and SJM provides possibility very effective tool to simulate anisotropic characteristics of jointed rock masses (Mas Ivars et al., 2011).

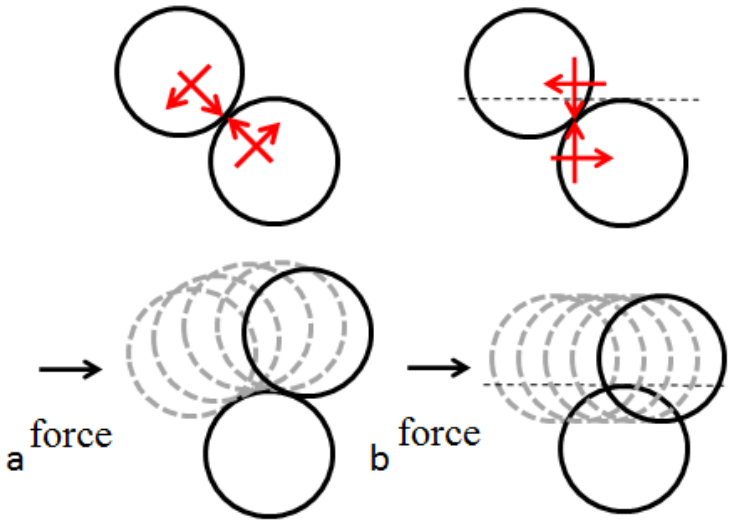

Figure 2.7 Kinematic models, (a) FJM. (b) SJM.

The SJM can be both bonded and unbonded (Fig. 2.8). When the SJM is bonded, the behaviour of the bonded interface is linear elastic until the strength limit is exceeded and the bond breaks, resulting in an unbonded interface. When the SJM is unbonded, the behaviour of the interface is linearly elastic and frictional with dilation, with slip accommodated by imposing a Coulomb limit on the shear force.

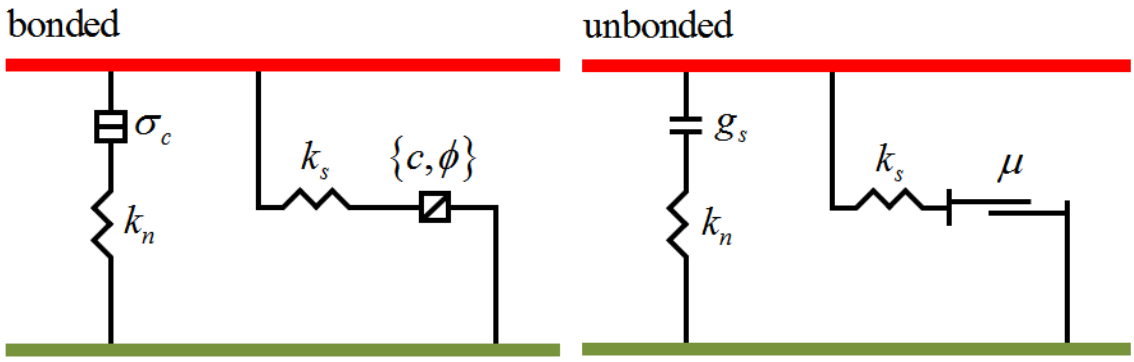

(a) (b)

Figure 2.8 Rheological components of the SJM

When the SJM is inserted into a BPM, the original contact microscopic properties including stiffness, friction coefficient, tensile strength, and cohesion along the defined joint plane will be replaced by SJM properties. Then the normal force and shear forces of the SJM can be calculated according to the force-displacement law:

$$F_n = k_n A \Delta\widehat{\delta_n^e} \tag{2.9}$$

$$F_s^* = k_s A \Delta\widehat{\delta_s^e} \tag{2.10}$$

where F_n and F_s^* are the normal and shear forces of the SJM; k_n and k_s are the normal stiffness and shear stiffness of the SJM; $\Delta\widehat{\delta_n^e}$ and $\Delta\widehat{\delta_s^e}$ are the normal and shear displacement increments of the SJM,; and A is the bond cross-sectional area.

If the SJM is unbonded, the shear force can be updated using the following equation:

$$F_s = \begin{cases} F_s^*, \|F_s^*\| \le F_s^\mu \\ F_s^\mu \left(\dfrac{F_s^*}{\|F_s^*\|}\right), \text{otherwise} \end{cases} \tag{2.11}$$

where $F_s^\mu = \mu F_n$ and μ is the friction coefficient. When slipping along the joint occurs, the shear displacement can produce the increment in the normal force due to dilation, i.e.,:

$$F_n = F_n + \left(\frac{|F_s^*| - F_s^\mu}{k_s} \right) k_n \tan \psi \tag{2.12}$$

where ψ is the dilation angle. If the SJM is bonded, the SJM will form a tensile crack under tension when:

$$F_n \geq \sigma_c A \tag{2.13}$$

where σ_c is the bond normal strength of the SJM. On the other hand, the SJM will form a shear crack under shear conditions when:

$$|F_s^*| \geq \tau_c A \tag{2.14}$$

where τ_c is the bond shear strength of the SJM.

Like the FJM, no comprehensive relationships between microscopic parameters and macroscopic properties of joint in anisotropic rocks exist. Xia and Zeng (2018) investigated some of these relationships between SJM microscopic parameters and macroscopic characteristics of anisotropic rock masses and suggested a calibration procedure.

By combining FJM and SJM, various mechanical responses of jointed rock masses including peak strength, scale effect, anisotropy, and fracturing have been successfully captured and modelled (Martin et al. 2012; Zhang et al. 2015; Zhang and Zhao 2016). Table 2.5 summarizes the previous studies adopting the SJM to investigate the anisotropic characteristics of jointed rock masses. Using a single persistent joint, Chiu et al. (2016) proposed a method to model the joint roughness using SJM while Hu et al. (2017) studied the effects of microscopic parameters of SJM on the mechanical responses of jointed rock masses. Using a set of persistent parallel joints, other studies investigated different mechanical properties of anisotropic rock masses such as uniaxial compressive strength (Park and Min 2015; Wang et al. 2016a; Park et al. 2018), direct tensile strength (Park et al.

2018; Shang et al. 2018), and fracturing (Park and Min 2015; Aziznejad et al. 2018), and deformation modulus (Zhao et al. 2015). Duan et al. (2015) and Duan and Kwok (2015) also studied the uniaxial compressive strength and tensile strength using a set of microscopic joints modelled by SJM. On the other hand, Bahaaddini et al. (2015) explored the effects of geometrical parameters of a set of non-persistent joints on the mechanical behaviour of a jointed rock mass under uniaxial compression.

Table 2.5 Summary of previous studies adopting the SJM to investigate the anisotropic characteristics of jointed rock masses

References	Method	Joint types	Research scope
Park et al. 2018	PFC3D	A set of parallel persistent joints	Modelling anisotropic uniaxial compressive and tensile strength
Shang et al. 2018	PFC3D	A set of parallel persistent joints	Modelling direct tensile behaviour of anisotropic rocks
Aziznejad et al. 2018	PFC2D	A set of parallel persistent joints	Static and dynamic responses of the anisotropic rock foundation
Hu et al. 2017	PFC2D	A single persistent joint	Parametric studies of SJM on mechanical properties of jointed rock masses
Chiu et al. 2016	PFC2D	A single persistent joint	Modelling a joint with different roughness
Wang et al. 2016b	PFC2D	A set of parallel persistent joints	Modelling of strength variations for anisotropic rock masses under uniaxial compression
Duan et al. 2015	PFC2D	A set of micro-parallel joints	Modelling anisotropic rock behaviours under uniaxial compression
Duan and Kwok 2015	PFC2D	A set of micro-parallel joints	Modelling anisotropic rock behaviours under Brazilian test conditions
Huang et al. 2015	PFC3D	A single non-persistent joint	Studies of the effects of micro-parameters of SJM on the macro-properties of rocks under uniaxial compression
Park and Min 2015	PFC2D	A set of parallel persistent joints	Modelling mechanical properties of anisotropic rocks and the rock foundation.

Zhao et al. 2015	PFC2D	A single or a set of parallel persistent joints	Studies of the deformation and failure modes of a rock mass containing different number of concentrated parallel joints at different spacing
Bahaaddini et al. 2015	PFC3D	A set of non-persistent joints	Effects of joint geometrical parameters on the uniaxial compressive strength (UCS) and the deformation modulus
Chiu et al. 2013	PFC2D	A set of parallel joints	A comparison study of different joint models

Although the anisotropic mechanical behaviours of jointed rock masses are extensively investigated under static conditions, the dynamic behaviours of anisotropic rock masses have not been widely studied in numerical models. To date, the majority of numerical studies on rock dynamic behaviours focus on intact rock (Zhang and Zhao 2014). In engineering applications, however, discontinuities have a critical influence on the dynamic behaviour of rock masses, which is vital for engineering applications. The numerical modelling works related to the dynamic properties of rock masses containing discontinuities are still very limited.

Previous studies demonstrated that mechanical properties such as strength (Doan and Billi 2011), elastic modulus (Brace and Jones 1971), and fracture toughness (Kim and Chao 2007; Feng et al. 2017) of intact rocks are largely influenced by strain rate. On the basis of experimental results, several semi-empirical relationships for the estimation of the rate-dependent dynamic strength of rock-like materials were proposed by different researchers (Grady and Lipkin 1980; Masuda et al. 1987; Olsson 1991; Malvar et al. 1998; Zhao et al. 1999), see Table 2.6. Results indicated that the dynamic uniaxial compressive strength can be related to the normalized strain rate and the static rock uniaxial compressive strength (Masuda et al. 1987). For dynamic failure criteria, Zhao (2000) modified and extended the classic failure criteria, such as the Mohr-Coulomb (MC) and Hoek-Brown (HB) criteria, to incorporate the dynamic strength of rocks (Table 2.7).

Table 2.6 Semi-empirical relationships for the estimation of the rate-dependent dynamic strength of intact rock-like materials

Material type	Semi-empirical equation	$\dot{\varepsilon}$ (s^{-1})	Material constants	References
Granite	$\sigma_{ud} = Clog(\varepsilon) + \sigma_{us}$	10^{-8}-10^{-4}	C=13 MPa/log(s^{-1}), σ_{ud}=340 MPa	(Masuda et al. 1987)
Granite	$\sigma_{ud} = RSC_d log\left(\frac{\varepsilon}{\varepsilon_s}\right) + \sigma_{us}$	10^{-8}-10^{0}	RSC_d=11.9 MPa, σ_{us}=170 MPa, $\varepsilon_s = 0.5 - 1\ s^{-1}$	(Zhao et al. 1999)
Rocks	$\sigma_{ud} = a\varepsilon^n$	10^{0}-10^{5}	$n_{max} = \frac{1}{3}$	(Grady and Lipkin 1980)
Granites	$\sigma_{ud} \propto \varepsilon^{\frac{1}{1+n}} (\varepsilon < 10^2 s^{-1})$ $\sigma_{ud} \propto \varepsilon^{0.3} (\varepsilon \geq 10^2 s^{-1})$	10^{-6}-10^{3}	n=130	(Lankford 1981)
Basalts	$\sigma_{ud} \propto \varepsilon^{\frac{1}{1+n}} (\varepsilon < 10^2 s^{-1})$ $\sigma_{ud} \propto \varepsilon^{0.3} (\varepsilon \geq 10^2 s^{-1})$	10^{-6}-10^{3}	n=130	(Lankford 1981)
Limestone	$\sigma_{ud} \propto \varepsilon^{\frac{1}{144}} (\varepsilon < 10^2 s^{-1})$ $\sigma_{ud} \propto \varepsilon^{0.31} (\varepsilon \geq 10^2 s^{-1})$	10^{-4}-10^{4}		(Green and Perkins 1968)
Tuff	$\sigma_{ud} \propto \varepsilon^{0.007} (\varepsilon < 76 s^{-1})$ $\sigma_{ud} \propto \varepsilon^{0.35} (\varepsilon \geq 76 s^{-1})$	10^{-6}-10^{3}		(Olsson 1991)
concrete	$\sigma_{ud} = \sigma_{us}\left(\frac{\varepsilon}{\varepsilon_s}\right)^{1.026\alpha_s} (\varepsilon < 30 s^{-1})$ $\sigma_{ud} = \sigma_{us}\gamma_s\left(\frac{\varepsilon}{\varepsilon_s}\right)^{\frac{1}{3}} (\varepsilon \geq 30 s^{-1})$	10^{-5}-10^{3}	$\alpha_s = \frac{1}{5 + \frac{\sigma_{us}}{10}}$ $\gamma_s = 10^{6.156\alpha_s - 2.0}$ $\varepsilon_s = 3.0 \times 10^{-5} s^{-1}$	(Malvar et al. 1998)

Note: σ_{ud} and σ_{us} are uniaxial dynamic compressive strength and uniaxial static compressive strength; C is a material parameter; RSC_d is the dynamic rock strength constant; ε_s is the static strain rate, which has different values in different studies, but falls in the range between 10^{-5} to 10^{-1} s^{-1}; a and n are constants; $\dot{\varepsilon}$ is the valid range of strain rate.

Table 2.7 Dynamic failure criterion for intact rock

Failure criterion	Modified equation	Comments	References
Mohr-Coulomb criterion	$\sigma_{1d} = \sigma_{ud} + \sigma_3 \frac{1+sin\varphi}{1-sin\varphi}$ $c_d = \frac{\sigma_{ud}(1-sin\varphi)}{2cos\varphi}$	φ is hardly influenced by ε only applicable for low confining stress	(Zhao 2000)
Hoek-Brown criterion	$\sigma_{1d} = \sigma_3 + \sigma_{ud}\left(\frac{m\sigma_3}{\sigma_{ud}} + 1.0\right)^{0.5}$	m is not affected by ε	(Zhao 2000)

Note: σ_{1d} and σ_{ud} are the dynamic triaxial compressive strength and the dynamic uniaxial compressive strength respectively; c_d is the dynamic cohesion; φ is the internal friction angle of intact rock; m is the Hoek-Brown constant for rock material.

In addition to the experimental and theoretical studies mentioned above, BPM was employed to investigate on the effect of strain rate on the mechanical behaviour of intact rocks (Jacson et al. 2008; Zhang and Wong 2013; Zhang et al. 2017). Using a BPM, Jackson et al. (2008) found that both the energy needed to bring a specimen to failure and the degree of fragmentation increase with increasing strain rate. Zhang and Wong (2013) demonstrated that, with increasing strain rate, the dynamic compressive strength and crack coalescence stress significantly increase, while crack initiation stress slightly increases, for rock specimens containing a non-persistent joint. In their further study, Zhang et al. (2017) indicated that numbers of shear and tensile cracks, together with acoustic emissions, increase with increasing strain rate. However, these studies mainly focus on fragmentation and cracking process, and there is no systematic numerical study using BPM to establish the relationship between the dynamic strength and the strain rate, either for intact or jointed rock.

2.3 Statistical damage model (SDM)

In addition to the use of BPM for modelling the anisotropic characteristics of rock masses, the statistical damage model (SDM) may provide an alternative but the simpler approach, which has not been tried in previous studies.

Damage mechanics (DM) has been widely employed to describe the stress-strain relationship of various mechanical responses for rocks in different applications. By combining statistical theory and continuum damage mechanics, Krajcinovic and Silva (1982) explored the mechanical responses of concretes and proposed a statistical damage model (SDM) to reflect the process of micro-crack initiation, propagation, and coalescence. Within the framework of the original SDM, the model was adopted and extended to study various mechanical responses of rocks (Tang et al. 1998; Cao et al. 2010, 2018; Deng and Gu 2011; Li et al. 2012; Liu and Yuan 2015). These SDMs can be divided into two main approaches based on their assumptions. The chain model assumes that rocks consist of a series of mechanical components (e.g. spring, stick, and slider) to simulate the failure behaviour (Zhou et al. 2001). The other SDM assumes that rocks contain numerous microscopic elements, and the damage process can be regarded as the damage accumulation of these microscopic elements (Tang et al. 1997). In this work, the concept of SDM refers to the latter damage model mentioned-above and the schematic of these models is demonstrate in Fig. 2.9.

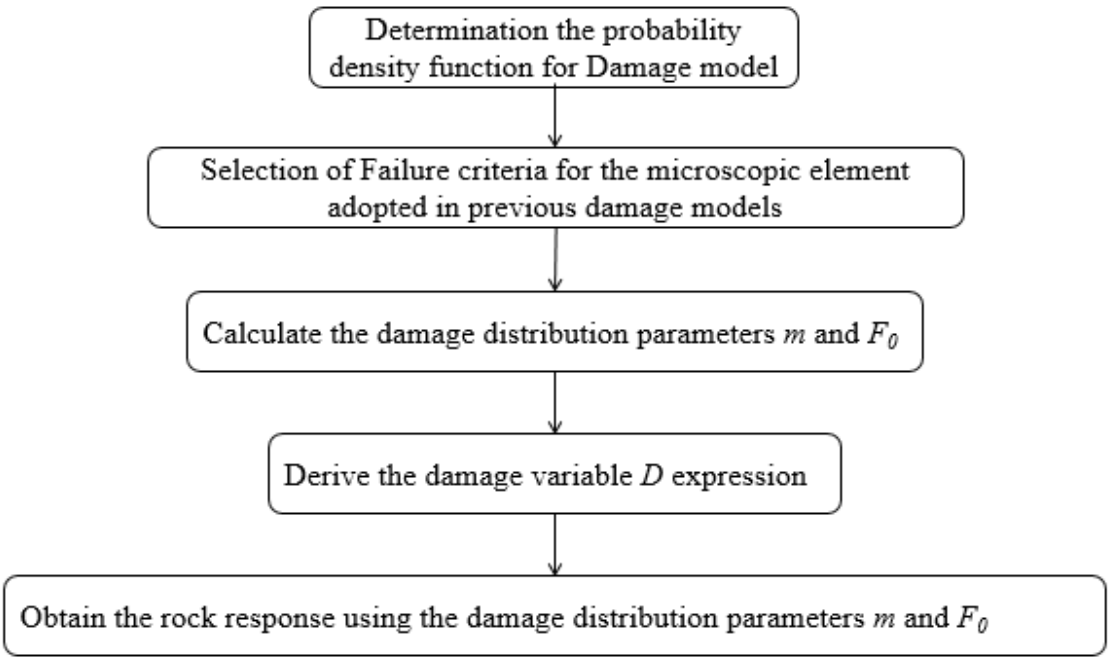

Figure 2.9 Schematic of the statistical damage model

Due to the easy implementation and application to an engineering analysis, the SDM has been favoured by many researchers based on statistical and stochastic theories (Tang 1997; Cao et al. 2010; Deng and Gu 2011; Li et al. 2012; Liu and Yuan 2015). Two steps are needed to establish a statistical constitutive damage model (Liu and Yuan 2015): the determination of the strength distribution of the microscopic elements and the selection of a proper micro-element failure criterion.

Four types of distributions have been used in published research to describe the strength distribution of microscopic elements: Weibull distribution, power function distribution, normal logarithmic distribution, and normal distribution (Li et al. 2017). Their corresponding probability density functions are summarized in Table 2.8. Previous studies (Li et al. 2017; Chen et al. 2018) argued that the pre-peak stress-strain curve can be well fit by constitutive models using different distributions, especially for the elastic deformation stage of rocks. However, compared with the power function, the damage model using the

Weibull distribution can better capture the rock plasticity behaviour of rocks (Chen et al. 2018). Therefore, it is reasonable to describe the rock microscopic unit strength using a Weibull distribution statistical probability model.

Table 2.8 The function of the probability density of various distributions adopted in previous damage models

Distributions	Function of probability density	References
Weibull distribution	$P(F)=\frac{m}{F_0}\left(\frac{F}{F_0}\right)^{m-1}\exp\left[-\left(\frac{F}{F_0}\right)^{m}\right]$	(Li et al. 2012) (Liu and Yuan 2015)
Power distribution	$P(F)=\frac{m}{F_0}\left(\frac{F}{F_0}\right)^{m-1}$	(Chen et al. 2018) (Li et al. 2017)
Normal distribution	$P(F)=\frac{1}{\sqrt{2\pi}S_0}\exp\left[-\frac{1}{2}\left(\frac{F-F_0}{S_0}\right)^{2}\right]$	(Kang et al. 2012) (Li et al. 2017)
Log-normal distribution	$P(F)=\frac{1}{\sqrt{2\pi}FS_0}\exp\left[-\frac{1}{2}\left(\frac{\ln F-F_0}{S_0}\right)^{2}\right]$	(Zhang et al. 2005) (Li et al. 2017)

where F is an elemental strength parameter depending on the strength criterion used; m, F_0 and S_0 are distribution parameters for corresponding distributions.

Based on the damage evolution process using a Weibull distribution (Bhattacharya and Ellingwood 1998), the damage variable D can be measured in the following form:

$$D=1-exp\left[-\left(\frac{F}{F_0}\right)^{m}\right] \tag{2.15}$$

The damage variable D correlates with the microscopic element strength F, which satisfies the Weibull distribution with two distribution parameters, e.g. F_0 and m. Identifying a suitable F to represent the strength of microscopic elements is a challenge. As the pioneer of the statistical damage mechanics, Tang (1997) suggested using maximum strain theory for microscopic elements. Later, many more appropriate failure criteria were adopted to

describe the stress state of the microscopic element (Cao et al. 2010; Li et al. 2012). The commonly used failure criteria in SDM are Mohr-Coulomb, the Drucker-Prager, and Hoek-Brown (Table 2.9). Compared with the damage model using maximum strain theory, damage models using the classical failure criteria better reflect the stress level of the microscopic elements (Li et al. 2012). However, the merits and limitations of the SDMs with various failure criteria should be further investigated.

Table 2.9 Failure criteria for the microscopic element adopted in previous damage models

Failure criterion	Expression in the principal stress space	References
Maximum strain theory	$F = \varepsilon$	(Tang 1997) (Liu and Yuan 2015)
Mohr-Coulomb criterion	$F(I_1', J_2', \theta_\sigma) = \frac{1}{3} I_1' \sin\varphi + \left(\cos\theta_\sigma - \frac{1}{\sqrt{3}} \sin\theta_\sigma \sin\varphi\right)\sqrt{J_2'} = c\cos\varphi$	(Cao et al. 2010) (Li et al. 2012)
Drucker-Prager criterion	$F(I_1', J_2') = \alpha_0 I_1' + \sqrt{J_2'} = k$	(Cao et al. 1988) (Xu and Karakus 2018)
Hoek-Brown criterion	$F(I_1', J_2', \theta_\sigma) = m\sigma_c \frac{I_1'}{3} + 4J_2' \cos^2\theta_\sigma + m\sigma_c\sqrt{J_2'}\left(\cos\theta_\sigma + \frac{\sin\theta_\sigma}{\sqrt{3}}\right) = s\sigma_c^2$	(Xu et al. 2017) (Xu and Karakus 2018)

Note: ε is the strain of rocks when maximum strain theory adopted in SDM; I_1' and J_2' are the first effective stress invariant and the second effective deviator stress invariant, respectively; θ_σ is the lode angle; c and φ are the cohesive strength and internal friction angle of the rock; α_0 and k are the materials constants related to the cohesive strength and internal friction angle, where $\alpha_0 = \frac{\sin\varphi}{\sqrt{3(3+\sin^2\varphi)}}, k = \frac{3c\cos\varphi}{\sqrt{3(3+\sin^2\varphi)}}$; σ_c is the uniaxial compressive strength of intact rock; m and s are Hoek-Brown input parameters.

Then the constitutive relationship for rocks expressed using a SDM is given by the following Equation using a Weibull distribution in the major principal stress direction (Li et al. 2012):

$$\sigma_1 = E\varepsilon_1 \exp\left[-\left(\frac{F}{F_0}\right)^m\right] + \mu(\sigma_2 + \sigma_3) \tag{2.16}$$

where μ is the Poisson's ratio of the rock. To capture rock mechanical responses using a SDM, it is necessary to estimate the damage distribution parameters (F_0 and m). Currently, two methods are available to determine the distribution parameters according to the stress-strain responses from the laboratory tests: the back analysis method (Liu and Yuan 2015; Chen et al. 2018) and extremum method (Deng and Gu 2011; Li et al. 2012). As pointed by Li et al. (2012), the back analysis method may involve uncertainty in the analysis process, and the mechanical meaning of model parameters is unclear. Therefore, another procedure to determine the distribution parameters was proposed by Li et al. (2012). On the stress-strain curve, the peak point is quite near the yield point, which can be used to determine the model parameters *m* and F_0. At the peak, the derivative of σ_1 with corresponding ε_1 should be zero (Fig. 2.10) i.e.:

$$\varepsilon_1 = \varepsilon_{1f}, \sigma_1 = \sigma_{1f} \tag{2.17}$$

$$\varepsilon_1 = \varepsilon_{1f}, \frac{d\sigma_1}{d\varepsilon_1} = 0 \tag{2.18}$$

where σ_{1f} and ε_{1f} are the stress and strain corresponding to the peak point.

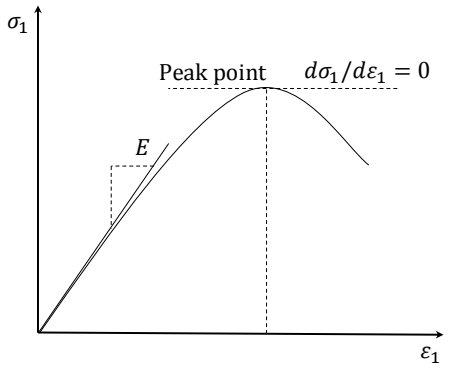

Figure 2.10 Determination of damage distribution parameters using the Extremum method, after Li et al. (2012)

Within the framework of the SDM, many researchers adopted and extended the classical SDM to capture the complex mechanical responses of rocks. The initial damage (crack closure stage) was identified and modelled by introducing initial voids (Cao et al. 2018) and dissipated energy corresponding to the initial damage (Yang et al. 2015). The residual strength of rocks induced by the confining pressure was further considered by different researchers. For example, a coefficient C_n was introduced by Wang et al. (2007) to improve the description of residual strength. Zhao et al. (2016b) adopted the damage tolerance principle to reflect the residual strength of the rocks. The impact on the mechanical properties of rocks was captured by the SDM using the coefficient of viscosity (Li et al. 2015) and over-stress model (Zhao et al. 2014). Recently, coupled damage models were proposed to gasp mechanical responses such as thermal effect (Yu et al. 2015; Peng et al. 2016; Xu and Karakus 2018), hydraulic (Zhang et al. 2016) and freeze-thaw (Huang et al. 2018). All these complex mechanical responses under various external conditions can be analysed by original or extended SDMs.

In field applications, jointed rock masses may demonstrate anisotropic characteristics when encountering large and persistent discontinuities, which is vital to the stability of surface or underground rock structures such as slopes and caverns (Hudson and Harrison 2000; Jia et al. 2012; Kostić 2017). BPM may provide a platform to analyse the stability of these in-situ structures; however, the BPM can be time-consuming, particularly when it is used to model field applications where a large number of particles are involved. In this case, the SDM may offer a different simpler approach to model and analyse the rock mass anisotropic behaviours. The application of SDM in this context is still very limited. In classical damage models (CDM), damage tensors, in most cases, were used to describe rock mass anisotropic behaviours. Kawamoto et al. (1988) and Swoboda et al. (1998) adopted a second-order damage tensor to reflect rock mass anisotropy due to pre-existing joints. In their damage

models, geometrical parameters of joints such as orientation, length, and density were considered. To define the degradation of the strength due to pre-existing joints, Kawamoto et al. (1988) and Swoboda et al. (1998) used the effective area and the initial damage parameter to represent the initial damage. However, the limitation of these methods is that they do not consider the influences of joint mechanical properties, such as shear strength (Liu and Yuan 2015). In order to understand the failure strength of jointed rock masses with a single fracture or a set of fractures, many empirical failure criteria modified from the classical failure criteria were proposed (Table 2.10).

Table 2.10 Summary of the modified failure criteria for anisotropic rocks

Original criterion	Modified failure criterion	References
Mohr-Coulomb criterion	Jaeger's criterion	(Jaeger 1960)
	Variable cohesion and friction angle criterion	(McLamore and Gray 1967)
	Tien and Kuo criterion	(Tien and Kuo 2001)
	The plane of patchy weakness theory	(Fjær and Nes 2014)
	A Nonlinear criterion	(Singh et al. 2015)
	Sliding and non-sliding model	(Asadi and Bagheripour 2015)
	Shi's criterion	(Shi et al. 2016a)
Barton-Bandis criterion	Duveau and Shao criterion	(Duveau et al. 1998)
	An extended plane of weakness theory	(Halakatevakis and Sofianos 2010)
Hoek-Brown criterion	Colak and Unlu criterion	(Colak and Unlu 2004)
	Saroglou and Tsiambaos criterion	(Saroglou and Tsiambaos 2008)
	Shi's criterion	(Shi et al. 2016b)

In a recent publication, Liu and Yuan (2015) proposed a coupled damage model which includes the shear strength of the macroscopic joint. However, as pointed by Liu and Yuan (2015), the joint stiffness effect on the deformability of the rock mass was ignored. In addition, it seems that they consider the shear strength in an arbitrary way using a coupling damage model. Within the framework of SDM, no studies have been found to represent the

geometrical and mechanical behaviours due to the pre-existing joint. Therefore, there is a need to develop a SDM for anisotropic rock masses considering joint orientations and joint mechanical properties.

This section summarizes previous studies on the theoretical and numerical modelling of mechanical behaviours of anisotropic rock masses. Although these studies lay the foundation in the area, there are still many unresolved challenging issues:

1. The complex relationships between microscopic parameters and macroscopic properties for BPM, especially FJM, are not clear;
2. Dynamic behaviour of jointed rocks is still an under-research area in rock engineering;
3. The joint orientation of the anisotropic rock masses is not properly considered in the current statistical damage model.

References:

Asadi M, Bagheripour MH (2015) Modified criteria for sliding and non-sliding failure of anisotropic jointed rocks. Int J Rock Mech Min Sci 73:95–101.

Aziznejad S, Esmaieli K, Hadjigeorgiou J, Labrie D (2018) Responses of jointed rock masses subjected to impact loading. J Rock Mech Geotech Eng 10:624–634.

Bahaaddini M, Hagan P, Mitra R, Hebblewhite BK (2015) Numerical Study of the Mechanical Behavior of Nonpersistent Jointed Rock Masses. Int Journals geochanics 16:04015035.

Bhattacharya B, Ellingwood B (1998) Continuum damage mechanics-based model of stochastic damage growth. J Eng Mech 124:1000–1009.

Brace WF, Jones AH (1971) Comparison of uniaxial deformation in shock and static

loading of three rocks. J Geophys Res 76:4913–4921

Cao W, Fang Z, Tang X (1988) A study of statistical constitutive model for soft and damage rocks. Chiniese J. Rock Mech. Enigneering 17:628–633

Cao W, Tan X, Zhang C, He M (2018) A constitutive model to simulate the full deformation and failure process for rocks considering initial compression and residual strength behaviors. Can Geotech J 54:1–51

Cao W, Zhao H, Li X, Zhang Y (2010) Statistical damage model with strain softening and hardening for rocks under the influence of voids and volume changes. Can Geotech J 47:857–871

Castro-Filgueira U, Alejano LR, Arzúa J, Ivars DM (2017) Sensitivity Analysis of the Micro-Parameters Used in a PFC Analysis Towards the Mechanical Properties of Rocks. Procedia Eng 191:488–495.

Chehreghani S, Noaparast M, Rezai B, Ziaedin S (2017) Bonded-particle model calibration using response surface methodology. Particuology 32:141–152.

Chen P (2017) Effects of microparameters on macroparameters of flat-jointed bonded-particle materials and suggestions on trial-and-error method. Geotech Geol Eng 35:663–677.

Chen S, Qiao C, Ye Q, Khan MU (2018) Comparative study on three-dimensional statistical damage constitutive modified model of rock based on power function and Weibull distribution. Environ Earth Sci 77:108.

Chiu CC, Wang TT, Weng MC, Huang TH (2013) Modeling the anisotropic behavior of jointed rock mass using a modified smooth-joint model. Int J Rock Mech Min Sci 62:14–22.

Chiu CC, Weng MC, Huang TH (2016) Modeling rock joint behavior using a rough-joint model. Int J Rock Mech Min Sci 89:14–25.

Cho N, Martin CD, Sego DC (2007) A clumped particle model for rock. Int J Rock Mech Min Sci 44:997–1010.

Colak K, Unlu T (2004) Effect of transverse anisotropy on the Hoek-Brown strength parameter “mi” for intact rocks. Int J Rock Mech Min Sci 41:1045–1052.

Cundall PA (2000) Numerical experiments on rough joints in shear using a bonded particle model. Springer, Berlin, Heidelberg.

Cundall PA, Strack ODL (1979) A discrete numerical model for granular assemblies. Géotechnique 29:47–65

Deng J, Gu D (2011) On a statistical damage constitutive model for rock materials. Comput Geosci 37:122–128

Doan ML, Billi A (2011) High strain rate damage of Carrara marble. Geophys Res Lett 38.

Duan K, Kwok CY (2015) Discrete element modeling of anisotropic rock under Brazilian test conditions. Int J Rock Mech Min Sci 78:46–56.

Duan K, Kwok CY, Pierce M (2015) Discrete element method modeling of inherently anisotropic rocks under uniaxial compression loading. Int J Numer Anal Methods Geomech 32:189–213.

Duveau G, Shao JF, Henry JP (1998) Assessment of some failure criteria for strongly anisotropic geomaterials. Mech Cohesive-Frictional Mater 3:1–26.

Fakhimi A, Villegas T (2007) Application of dimensional analysis in calibration of a discrete element model for rock deformation and fracture. Rock Mech Rock Eng

40:193–211.

Farahmand K, Diederichs MS, Vlachopoulos N (2015) Generation of a synthetic rock mass (SRM) model for simulation of strength of crystalline rock using a hybrid DFN- DEM approach. In: ISRM Regional Symposium-EUROCK 2015. International Society for Rock Mechanics.

Feng P, Ayatollahi MR, Dai F, Xu NW, Wei MD (2017) DEM investigation on fracture mechanism of the CCNSCB specimen under intermediate dynamic loading. Arab J Geosci 10:48.

Fjær E, Nes OM (2014) The impact of heterogeneity on the anisotropic strength of an outcrop shale. Rock Mech Rock Eng 47:1603–1611.

Gao F (2013) Simulation of Failure Mechanisms around Underground Coal Mine Openings Using Discrete Element Modelling (Doctoral dissertation). Simon Fraser University.

Grady DE, Lipkin J (1980) Criteria for impulsive rock fracture. Geophys Res Lett 7:255–258.

Green SJ, Perkins RD (1968) Uniaxial compression tests at varying strain rates on three geologic materials. In: The 10th US Symposium on Rock Mechanics (USRMS). American Rock Mechanics Association, pp 35–54.

Halakatevakis N, Sofianos AI (2010) Strength of a blocky rock mass based on an extended plane of weakness theory. Int J Rock Mech Min Sci 47:568–582.

He X, Xu C (2015) Discrete element modelling of rock cutting: from ductile to brittle transition. Int J Numer Anal Methods Geomech 39:1331–1351.

Hu W, Kwok CY, Duan K, Wang T (2017) Parametric study of the smooth-joint contact

model on the mechanical behavior of jointed rock. Int J Numer Anal Methods Geomech 1–19.

Huang D, Wang J, Liu S (2015) A comprehensive study on the smooth joint model in DEM simulation of jointed rock masses. Granul Matter 17:775–791.

Huang H (1999) Discrete element modeling of tool-rock interaction (Doctoral dissertation). The University of Minnesota.

Huang H, Lecampion B, Detournay E (2013) Discrete element modeling of tool-rock interaction I: Rock cutting. Int J Numer Anal Methods Geomech 37:1913–1929.

Huang S, Liu Q, Cheng A, Liu Y (2018) A statistical damage constitutive model under freeze-thaw and loading for rock and its engineering application. Cold Reg Sci Technol 145:142–150.

Hudson JA, Harrison JP (2000) Engineering rock mechanics: an introduction to the principles. Oxford; New York, Elsevier.

Itasca Consulting Group Inc (2014) Particle Flow Code, User's Guide. 3–6.

Jackson K, Kingman SW, Whittles DN, Lowndes IS, Reddish DJ (2008) The effect of strain rate on the breakage behavior of rock. Arch Min Sci 53:3–22.

Jaeger JC (1959) The frictional properties of joints in rock. Pure Appl Geophys 43:148–158.

Jaeger JC (1960) Shear failure of anisotropic rocks. Geol Mag 97:65–72.

Jia P, Yang TH, Yu QL (2012) Mechanism of parallel fractures around deep underground excavations. Theor Appl Fract Mech 61:57–65.

Jiang C, Zhao GF, Zhu J, Zhao YX, Shen L (2016) Investigation of Dynamic Crack

Coalescence Using a Gypsum-Like 3D Printing Material. Rock Mech Rock Eng 49:3983–3998.

Jing L (2003) A review of techniques, advances and outstanding issues in numerical modelling for rock mechanics and rock engineering. 39:283–353.

Kang Y, Jia Y, Fang G (2012) Rock damage mechanism based on the maximum tensile strain. J Lanzhou Univ (Natural Sci 48:.

Kim Y, Chao YJ (2007) Effect of loading rate on dynamic fracture initiation toughness of brittle materials. Int J Fract 145:195–204.

Kostić S (2017) Analytical Models for Estimation of Slope Stability in Homogeneous Intact and Jointed Rock Masses with a Single Joint. Int J Geomech 17:04017089.

Krajcinovic D, Silva MAG (1982) Statistical aspects of the continuous damage theory. Int J Solids Struct 18:551–562.

Labuz JF, Zang A (2012) Mohr-Coulomb Failure Criterion. Rock Mech Rock Eng 45:975–979.

Lankford J (1981) The role of tensile microfracture in the strain rate dependence of compressive strength of fine-grained limestone-analogy with strong ceramics. Int J Rock Mech Min Sci 18:173–175.

Li X, Cao W, Su Y (2012) A statistical damage constitutive model for softening behavior of rocks. Eng Geol 143–144:1–17.

Li XB, Wang SM, Weng L, Huang LQ, Zhou T, Zhou J (2015) Damage constitutive model of different age concretes under impact load. J Cent South Univ 22:693–700.

Li Y, Jia D, Rui Z, Peng J, Fu C, Zhang J (2017) Evaluation method of rock brittleness

based on statistical constitutive relations for rock damage. J Pet Sci Eng 153:123–132.

Liu H, Yuan X (2015) A damage constitutive model for rock mass with persistent joints considering joint shear strength. Can Geotech J 52:1136–1143.

Malvar LJ, Crawford JE (1998) Dynamic Increase Factors. 28th DDESB Semin Orlando 1–17.

Martin CD, Lu Y, Lan H (2012) Scale effects in a Synthetic Rock Mass. In: Harmonising Rock Engineering and the Environment. International Society for Rock Mechanics and Rock Engineering, pp 473–478.

Ivars DM, Pierce ME, Darcel C, Reyes-Montes J, Potyondy DO, Young RP, Cundall PA (2011) The synthetic rock mass approach for jointed rock mass modelling. Int J Rock Mech Min Sci 48:219–244.

Mas Ivars D, Potyondy D, Pierce M, Cundall P (2008) The smooth-joint contact model. In: Proceedings of WCCM8-ECCOMAS, 2008, 8th. Venice, Italy.

Masuda K, Mizutani H, Yamada I (1987) Experimental study of strain-rate dependence and pressure dependence of failure properties of granite. J Phys Earth 35:37–66.

McLamore R, Gray KE (1967) The mechanical behavior of anisotropic sedimentary rocks. J Eng Ind 89:62–73.

Olsson WA (1991) The compressive strength of tuff as a function of strain rate from 10-6 to 103/sec. Int J Rock Mech Min Sci 28:115–118.

Park B, Min K-B (2015) Bonded-particle discrete element modeling of mechanical behavior of transversely isotropic rock. Int J Rock Mech Min Sci 76:243–255.

Park B, Min KB, Thompson N, Horsrud P (2018) Three-dimensional bonded-particle

discrete element modeling of mechanical behavior of transversely isotropic rock. Int J Rock Mech Min Sci 110:120–132.

Park JW, Song JJ (2009) Numerical simulation of a direct shear test on a rock joint using a bonded-particle model. Int J Rock Mech Min Sci 46:1315–1328.

Peng J, Rong G, Cai M, Yao MD, Zhou CB (2016) Physical and mechanical behaviors of a thermal-damaged coarse marble under uniaxial compression. Eng Geol 200:88–93.

Potyondy DO (2012) A flat-jointed bonded-particle material for hard rock. In: 46th US Rock mechanics/geomechanics symposium. American Rock Mechanics Association.

Potyondy DO, Cundall PA (2004) A bonded-particle model for rock. Int J Rock Mech Min Sci 41:1329–1364.

Saroglou H, Tsiambaos G (2008) A modified Hoek-Brown failure criterion for anisotropic intact rock. Int J Rock Mech Min Sci 45:223–234.

Schöpfer MPJ, Childs C, Walsh JJ (2007) Two-dimensional distinct element modeling of the structure and growth of normal faults in multilayer sequences: 1. Model calibration, boundary conditions, and selected results. J Geophys Res 112:B10401.

Shang J, Duan K, Gui Y, Handley K, Zhao Z (2018) Numerical investigation of the direct tensile behaviour of laminated and transversely isotropic rocks containing incipient bedding planes with different strengths. Comput Geotech 104:373–388.

Shea WT, Kronenberg AK (1993) Strength and anisotropy of foliated rocks with varied mica contents. J Struct Geol 15:1097–1121.

Shen J, Karakus M (2014) Simplified method for estimating the Hoek-Brown constant for intact rocks. J Geotech Geoenvironmental Eng 140:04014025.

Shi X, Yang X, Meng Y, Li G (2016a) An anisotropic strength model for layered rocks considering planes of weakness. Rock Mech Rock Eng 49:3783–3792.

Shi X, Yang X, Meng Y, Li G (2016b) Modified Hoek–Brown failure criterion for anisotropic rocks. Environ Earth Sci 75:1–11.

Shu B, Liang M, Zhang S, Dick J (2018) Numerical Modeling of the Relationship Between Mechanical Properties of Granite and Microparameters of the Flat-Joint Model Considering Particle Size Distribution. Math Geosci.

Singh M, Samadhiya NK, Kumar A, Kumar V, Singh B (2015) A nonlinear criterion for triaxial strength of inherently anisotropic rocks. Rock Mech Rock Eng 48:1387–1405.

Sun MJ, Tang HM, Hu XL, Ge YF, Lu S (2013) Microparameter Prediction for a Triaxial Compression PFC3D Model of Rock Using Full Factorial Designs and Artificial Neural Networks. Geotech Geol Eng 31:1249–1259.

Tang C (1997) Numerical simulation of progressive rock failure and associated seismicity. Int J rock Mech Min Sci Geomech Abstr 34:249–261.

Tang CA, Chen ZH, Xu XH, Li C (1997) A Theoretical Model for Kaiser Effect in Rock. Pure Appl Geophys 150:203–215.

Tang CA, Yang WT, Fu YF, Xu XH (1998) A new approach to numerical method of modelling geological processes and rock engineering problems-continuum to discontinuum and linearity to nonlinearity. Eng Geol 49:207–214.

Tawadrous AS, Degagne D, Pierce M, Ivars DM (2009) Prediction of uniaxial compression PFC3D model micro-properties using artificial neural networks. Int J Numer Anal Methods Geomech 33:1953–1962.

Tien YM, Kuo MC (2001) A failure criterion for transversely isotropic rocks. Int J Rock Mech Min Sci 38:399–412.

Vallejos JA, Brzovic A, Lopez C, Bouzeran L, Ivars DM (2013) Application of the synthetic rock mass approach to characterize rock mass behavior at the El Teniente Mine, Chile. In: FLAC/DEM Symposium. Minneapolis.

Vallejos JA, Salinas JM, Delonca A, Mas Ivars D (2016) Calibration and verification of two bonded-particle models for simulation of intact rock behavior. Int J Geomech 17:06016030.

Wang P, Yang T, Xu T, Cai M, Li C (2016a) Numerical analysis on scale effect of elasticity, strength and failure patterns of jointed rock masses. Geosci J 20:539–549.

Wang T, Xu D, Elsworth D, Zhou W (2016b) Distinct element modeling of strength variation in jointed rock masses under uniaxial compression. Geomech Geophys Geo-Energy Geo-Resources 2:11–24.

Wang Y, Tonon F (2010) Calibration of a discrete elementmodel for intact rock up to its peak strength. Int J Numer Anal Methods Geomech 34:447–469.

Wang Z liang, Li Y chi, Wang JG (2007) A damage-softening statistical constitutive model considering rock residual strength. Comput Geosci 33:1–9.

Wu S, Xu X (2016) A study of three intrinsic problems of the classic discrete element method using flat-joint model. Rock Mech Rock Eng 49:1813–1830.

Xia L, Zeng Y (2018) Parametric study of smooth joint parameters on the mechanical behavior of transversely isotropic rocks and research on calibration method. Comput Geotech 98:1–7.

Xu X, Gao F, Zhang Z (2017) Thermo-mechanical coupling damage constitutive model of rock based on the Hoek–Brown strength criterion. Int J Damage Mech 0:105678951772683.

Xu XL, Karakus M (2018) A coupled thermo-mechanical damage model for granite. Int J Rock Mech Min Sci 103:195–204.

Yang B, Jiao Y, Lei S (2006) A study on the effects of microparameters on macroproperties for specimens created by bonded particles. Eng Comput 23:607–631.

Yang SQ, Xu P, Ranjith PG (2015) Damage model of coal under creep and triaxial compression. Int J Rock Mech Min Sci 80:337–345.

Yoon J (2007) Application of experimental design and optimization to PFC model calibration in uniaxial compression simulation. Int J Rock Mech Min Sci 44:871–889.

Yu QL, Ranjith PG, Liu HY, Yang TH, Tang SB, Tang CA, Yang SQ (2015) A Mesostructure-based Damage Model for Thermal Cracking Analysis and Application in Granite at Elevated Temperatures. Rock Mech Rock Eng 48:2263–2282

Zhang M, Li Z, Su X (2005) Probabilistic volume element modeling in elastic damage analysis of quasi-Brittle materials. Chinese J Rock Mech Eng 24:4282–4288.

Zhang N, Li X, Cheng H, Teng T (2016) A coupled damage-hydro-mechanical model for gas drainage in low-permeability coalbeds. J Nat Gas Sci Eng 35:1032–1043.

Zhang QB, Zhao J (2014) A review of dynamic experimental techniques and mechanical behaviour of rock materials. Rock Mech Rock Eng 47:1411–1478.

Zhang X, Zhang Q, Wu S (2017) Acoustic emission characteristics of the rock-like material containing a single flaw under different compressive loading rates. Comput Geotech

83:83–97.

Zhang XP, Wong LNY (2012) Cracking processes in rock-like material containing a single flaw under uniaxial compression: a numerical study based on parallel bonded-particle model approach. Rock Mech Rock Eng 45:711–737.

Zhang XP, Wong LNY (2013) Loading rate effects on cracking behavior of flaw-contained specimens under uniaxial compression. Int J Fract 180:93–110.

Zhang Y, Stead D, Elmo D (2015) Characterization of strength and damage of hard rock pillars using a synthetic rock mass method. Comput Geotech 65:56–72.

Zhang Y, Zhao X (2016) Characterisation of confinement effect on jointed rock pillars using a Synthetic Rock Mass approach. Int J Numer Anal Methods Geomech 40:1690–1711.

Zhao G, Xie L, Meng X (2014) A damage-based constitutive model for rock under impacting load. Int J Min Sci Technol 24:505–511.

Zhao H, Zhang C, Cao W, Zhao M (2016) Statistical meso-damage model for quasi-brittle rocks to account for damage tolerance principle. Environ Earth Sci 75:862

Zhao J (2000) Applicability of Mohr-Coulomb and Hoek-Brown strength criteria to the dynamic strength of brittle rock. Int J Rock Mech Min Sci 37:1115–1121.

Zhao J, Li H., Wu M., Li T. (1999) Dynamic uniaxial compression tests on a granite. Int J Rock Mech Min Sci 36:273–277

Zhao W, Huang R, Yan M (2015) Study on the deformation and failure modes of rock mass containing concentrated parallel joints with different spacing and number based on smooth joint model in PFC. Arab J Geosci 8:7887–7897.

Zhou GL, Tham LG, Lee PKK, Tsui Y (2001) A phenomenological constitutive model for rocks with shear failure mode. Int J Numer Anal Methods Geomech 25:391–414.

Chapter 3 A systematic approach to calibrating micro-parameters for the macro-rock properties of a flat, joint-bonded particle model

(Paper 1)

Changtai Zhou[1], Chaoshui Xu[1], Murat Karakus[1], Jiayi Shen[2]

[1]School of Civil, Environmental and Mining Engineering, The University of Adelaide, Adelaide, Australia

[2]Institute of Port, Coastal and Offshore Engineering, Zhejiang University, Hangzhou, China

Statement of Authorship

Title of Paper	A systematic approach to the calibration micro-parameters for the flat-jointed bonded particle model
Publication Status	☑ Published ☐ Accepted for Publication ☐ Submitted for Publication ☐ Unpublished and Unsubmitted w ork w ritten in manuscript style
Publication Details	Zhou C, Xu C, Karakus M, Shen J (2018) A systematic approach to the calibration of micro-parameters for the flat-jointed bonded particle model. Geomech Eng 16:471–482. doi: DOI: 10.12989/gae.2018.16.5.471

Principal Author

Name of Principal Author (Candidate)	Changtai Zhou		
Contribution to the Paper	Conducted the research and w rote the manuscript.		
Overall percentage (%)	85%		
Certification:	This paper reports on original research I conducted during the period of my Higher Degree by Research candidature and is not subject to any obligations or contractual agreements with a third party that w ould constrain its inclusion in this thesis. I am the primary author of this paper.		
Signature		Date	17/02/2019

Co-Author Contributions

By signing the Statement of Authorship, each author certifies that:

i. the candidate's stated contribution to the publication is accurate (as detailed above);

ii. permission is granted for the candidate in include the publication in the thesis; and

iii. the sum of all co-author contributions is equal to 100% less the candidate's stated contribution.

Name of Co-Author	Chaoshui Xu		
Contribution to the Paper	Supervised the research and reviewed the manuscript.		
Signature		Date	18/02/2019

Name of Co-Author	Murat Karakus		
Contribution to the Paper	Supervised the research and reviewed the manuscript.		
Signature		Date	18/02/2019

Name of Co-Author	Jiayi Shen		
Contribution to the Paper	Supervised the research and reviewed the manuscript.		
Signature		Date	18/02/2019

Abstract

A flat-jointed bonded-particle model (BPM) has been proved to be an effective tool for simulating mechanical behaviours of intact rocks. However, the tedious and time-consuming calibration procedure imposes restrictions on its widespread application. In this study, a systematic approach is proposed for simplifying the calibration procedure. The initial relationships between the microscopic, constitutive parameters and macro-mechanical rock properties are firstly determined through dimensionless analysis. Then, sensitivity analyses and regression analyses are conducted to quantify the relationships, using results from numerical simulations. Finally, four examples are used to demonstrate the effectiveness and robustness of the proposed systematic approach for the calibration procedure of BPMs.

Keywords: Discrete element method; bonded-particle model; Flat-jointed model; micro-parameters; macro-rock properties; intact rocks.

1 Introduction

Numerical modelling provides the possibility for understanding the complexity of rock mechanical behaviours via analogy simplification. Cundall (1971) proposed the discrete element method (DEM) to simulate the microstructure features and mechanical properties of intact rocks. The particle flow code (PFC) (Itasca Consulting Group Inc 2014), as the most widely used DEM code in geomechanics, uses a granular assembly following Newton's law of motion. Such models are based on the belief that one can replicate the macro-properties of intact rocks if one can reproduce rock's microstructures and the corresponding interactions between them.

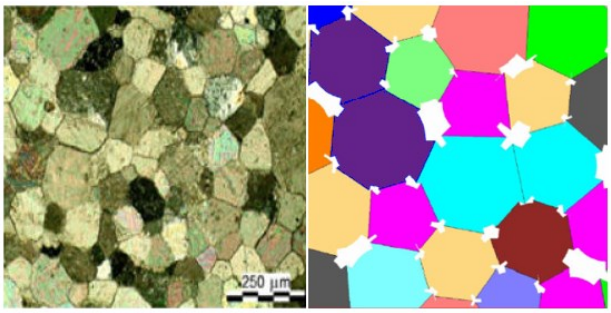

Figure 3.1 The scanning electron microscopy image of marble on the left, and the flat-jointed model material on the right.

At the early stage, PFC models were limited to simulating the mechanical behaviours of cohesionless granular materials without bonds between particles (Cundall and Strack 1979). In 2004, the bonded-particle model (BPM) (Potyondy and Cundall 2004) was introduced to reproduce the microstructures (see Fig. 3.1) and its corresponding macro-properties for intact rocks.

BPM can reproduce the behaviours of particle assemblies bonded by cementations, which mimic both the microstructure and the mechanical behaviours of intact rocks. The mechanical behaviours investigated in the literature include elasticity (Potyondy and

Cundall 2004; Schöpfer et al. 2007), fracturing (Zhao et al. 2015; Zhou et al. 2016), failure processes (Duan et al. 2015b), damage zones (Fakhimi and Villegas 2007), rock cutting (He and Xu 2015), crack initiation and coalescence processes (Vesga et al. 2008; Ning et al. 2015; Tian and Yang 2017) and shearing behaviours of soil-rock mixture (Xu et al. 2015)

Three BPMs, the linear-bond model (LBM), the parallel-bond model (PBM) and the flat-jointed model (FJM), are provided in PFC (Itasca Consulting Group Inc 2014). PBMs and FJMs are the most widely used in brittle rock simulations, which can produce a good match of mechanical behaviours of rocks at lab scales. However, a BPM with a LBM or a PBM suffers from three intrinsic problems: the unrealistic ratio of uniaxial compressive strength (UCS) to tensile strength (TS), the unrealistic low internal friction angle, and the unrealistic linear failure envelope (Potyondy and Cundall 2004; Cho et al. 2007; Schöpfer et al. 2007; Wu and Xu 2016). These limitations can be addressed in two ways: By either increasing interlock in the numerical models, i.e. creating clumps of particles (Cho et al. 2007), which will increase computation time; or by introducing a grain-based model.

(Potyondy 2012) reproduced the stress-strain behaviours of granite by using uniaxial compression tests and biaxial compression tests with the FJM. The work also revealed that macro-properties such as Young's modulus (E), Poisson's ratio (ν) and UCS can be matched to the laboratory data, and so too can the ratio of UCS to TS. Using a three-dimensional (3D) analysis, Wu and Xu (2016) confirmed that the unrealistically low ratio of UCS to TS can be fixed through FJM. They further explored the excessively low internal friction angle and the unrealistic failure envelope through uniaxial compression tests and triaxial compression tests. Vallejos et al. (2016) compared the PBM and FJM for intact rock simulations, and highly recommended FJM for intact rock simulations with and without confining pressures.

Despite the successful applications of the FJM for intact rock simulations, one issue remains unresolved: there are no direct relationships between micro-parameters of the FJM and the macro-mechanical properties of the rock being analysed. A tedious and time-consuming calibration process, on a trial and error basis, is normally required. This process involves performing numerical uniaxial compression tests, and direct or indirect tensile strength tests to derive a set of micro-parameters for the BPM using FJM. The time-consuming calibration process imposes significant restrictions on FJM's widespread applications for solving rock engineering problems. Numerous studies to address this issue for the PBM have been published (Huang 1999; Yang et al. 2006; Fakhimi and Villegas 2007). For example, a dimensionless analysis (Huang 1999) was introduced in the calibration procedure, which was proven to be more efficient and convenient (Yang et al. 2006; Fakhimi and Villegas 2007; He and Xu 2015). Yang et al. (2006) further proposed some empirical quantitative relationships to derive macro-properties of numerical models from micro-parameters. In contrast, for FJM, we found no published studies that quantify the relationships between micro-parameters and the macro properties of rocks. These relationships are expected to be completely different from those for the PBM because of their different mechanical behaviours at the micro-level (Potyondy 2012).

This paper aims to quantify the relationships between micro-parameters and macro-rock properties for FJM, which can then be used to build more effective and consistent numerical models for subsequent DEM studies. First, the background theory of FJM is reviewed. Using dimensionless analysis, we introduce the initial relationships between the micro-parameters and macro-properties of FJM. Then, the set of microscopic structure parameters that can generate a well-connected and isotropic particle assembly are determined. This paper then presents the results of uniaxial compression tests and direct tension tests, which are carried out to evaluate the effects of the individual, microscopic, constitutive parameters

on macro-rock properties. The results were used to simplify the proposed initial relationships. Regression analyses are performed based on the dimensionless analyses and the numerical modelling results to quantify the relationships. Finally, the performance of the derived relationships was assessed by testing them against four different types of rocks.

2 Relationships between micro-parameters and macro-rock properties of FJM

In this section, the fundamentals of FJM are reviewed, and the initial relationships between micro-parameters and macro-rock properties are introduced through dimensionless analysis.

2.1 Background theory of BPM

The BPM was introduced to simulate the mechanical behaviours of an assembly of rigid particles that are bonded together at and interact with each other through their contacts. The movement of these particles follows Newton's law of motion, while the interaction between particles is determined by constitutive models implemented at their contacts. The motion of particles includes two components: translational motion and rotational motion. As shown in Fig. 3.2a, contact force and moment arise when two particles come into contact are:

$$F_i = \sum_{j=1}^{n} (F_{ij}^n + F_{ij}^s) + F_i^{app} \tag{3.1}$$

$$M_i = \sum_{j=1}^{n} F_{ij}^s r_{ij} + M_i^{app} \tag{3.2}$$

where r_{ij} is the distance from the centre of particle *i* to the contact point between particle *i* and particle *j*; F_i^{app} and M_i^{app} are the additional force and moment applied to particle *i*; F_{ij}^n and F_{ij}^s are the normal and shear contact forces in the local coordinate system between particle *i* and particle *j*, respectively, see Fig 3.2b:

$$F_{ij}^{n} = k_{ij}^{n} U_{ij}^{n} \tag{3.3}$$

$$F_{ij}^{n} = -k_{ij}^{s} \Delta U_{ij}^{s} \tag{3.4}$$

where k_{ij}^{n} and k_{ij}^{s} are the normal and shear stiffness of the contact between particle *i* and particle *j*, U_{ij}^{n} is the overlap used to simulate the deformation of the particle in the normal direction, and ΔU_{ij}^{s} is the shear displacement increment between particle *i* and particle *j*.

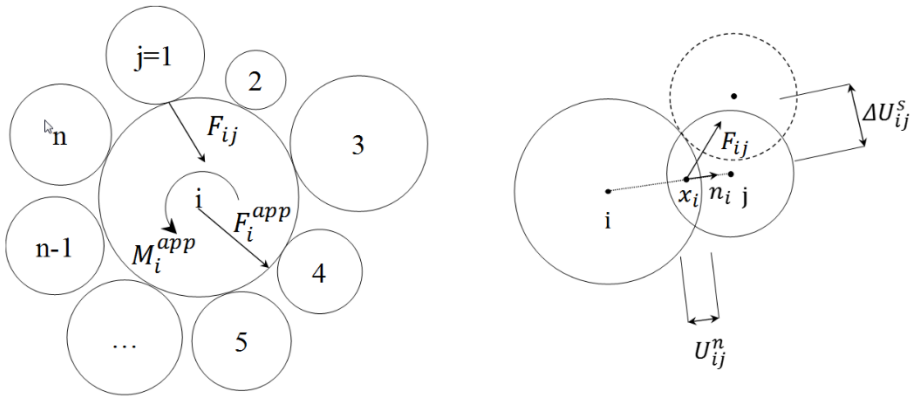

(a) (b)

Figure 3.2 (a) Forces and moments acting on a part; (b) Force-displacement behaviour at a contact

To simulate the quasi-static condition in DEM using the dynamic formulation implementation discussed above, some form of damping is necessary to dissipate the kinetic energy. In this study, the global damping was applied to damp out the particle accelerations.

2.2 Basic theory of FJM

The FJM provides the macroscopic behaviour of a finite-size, linear elastic, and either bonded or frictional interface that may sustain partial damage. The interface, a flat line in 2D, or a flat disc in 3D, can be discretised into several segments or several areas(elements), respectively.

A contact of FJM is active when any element is either bonded or has a negative gap. The contact may be deleted at the discretion of the contact detection logic when the distance between the notional surfaces becomes greater than the initial surface gap g_0. The implemented constitutive model of FJM is described in PFC manual (Itasca Consulting Group Inc 2014). The force-displacement relationship and yielding criterion are briefly described below.

The force-displacement relationship of FJM is determined by the relative displacement of two notional surfaces. Each of the equally discretised elements carries a force (F^e) and a moment (M^e), and can be either bonded or de-bonded at the centre of the interface, which coincides with the contact location. Then the normal stress and shear stress of FJM can be calculated.

When the bonded element is under tension, the tensile stress sustained by the bonded element can increase until the tensile strength of the bond is exceeded; then, the bonded element breaks (a tensile crack) and becomes a de-bonded element. The tensile strength of a de-bonded element by definition is zero. On the other hand, the shear strength of FJM follows the Mohr-Coulomb (MC) criterion, i.e,

$$\tau^e = c + \sigma^e \tan\phi_b \tag{3.5}$$

where c is the bond cohesion and ϕ_b is the local friction angle. The bonded element will break into a shear crack when the shear strength of the bond is exceeded. On the other hand, the shear strength of a de-bonded element obeys the Coulomb sliding criterion:

$$\tau^e = \sigma^e \tan\phi_r \tag{3.6}$$

where ϕ_r is the residual friction angle. The strength envelope of a bonded element is shown in Fig. 3.3.

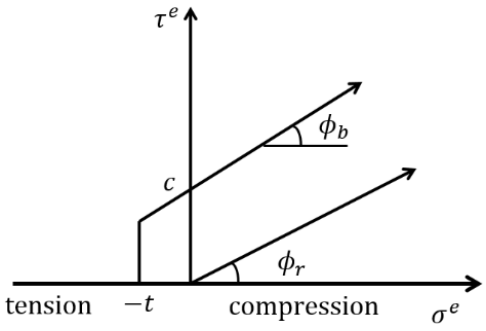

Figure 3.3 Failure envelopes for bonded elements and unbonded elements (Labuz and Zang 2012)

It is worthwhile to mention that for the FJM, the interface may evolve from a fully bonded state to a fully de-bonded and frictional state. Note that the breakage is brittle in FJM. However, the fully de-bonded interface is not removed during the simulation, so the interface will continue to resist relative rotation. This fictitious notional surface can, therefore, increase the ratio of UCS to TS by grain interlocking, which reflects rock behaviours more realistically at a micro scale, and is more advantageous compared with other bonded particle models (Potyondy 2012; Wu and Xu 2016).

For elastic deformability, in the latest version of PFC (Itasca Consulting Group Inc 2014), deformability method is employed to substitute the contact model properties. In this approach, the elastic contact properties, such as k_n and k_s, are not specified directly; rather, k_n and k_s of contacts are modified in the programme simultaneously to meet a target effective modulus (E^*) of the ball assembly. More details can be found in related works (Potyondy 2012; Wu and Xu 2016) and PFC manual (Itasca Consulting Group Inc 2014).

2.3 Preliminary relationships between micro-parameters and macro-properties

The dimensionless method (Huang 1999; Yang et al. 2006; Fakhimi and Villegas 2007; He and Xu 2015), through uniaxial compression tests and direct tension tests (Fig. 3.4), was proved to be useful and efficient for establishing the relationships between macro-

mechanical properties and micro-parameters. The BPM parameters can be divided into three groups: boundary conditions, micro-structure and geometrical parameters, and micro-mechanical and constitutive parameters between the particles, as shown in Table 3.1:

Table 3.1 Three groups of micro-parameters of BPM

Groups	Parameters	Symbol	Unit	Base unit
Boundary condition parameters	Specimen width	w	mm	L
	Specimen height	l	mm	L
	Loading rate	V	m/s	$L \cdot T^{-1}$
Micro-structures and geometrical parameters	Ratio of maximum to minimum ball radius	r_{max}/r_{min}	[-]	[-]
	Ratio of specimen width to the median ball diameter	w/d	[-]	[-]
	Bond surface gap	g_0	m	L
	Porosity of the synthetic the numerical specimen	n	[-]	[-]
	Number of elements in each bond	N_r	[-]	[-]
Micro-mechanical and constitutive parameters	Effective modulus of bond	E^*	GPa	$F \cdot L^{-2}$
	Stiffness ratio of contact	k^*	[-]	[-]
	Tensile strength of contact	t	MPa	$F \cdot L^{-2}$
	Cohesion of bond	c	MPa	$F \cdot L^{-2}$
	Friction angle of bond	ϕ_b	°	[-]
	Residual friction coefficient of bond	μ	[-]	[-]

Note: [*F, L, T*] represent the primary dimension of force, length and time respectively.

The mechanical properties, such as UCS, TS, E and v of FJM are governed by these parameters listed in Table 3.1. Dimensionless analysis, based on the Buckingham π theorem (Sonin 2004), was employed to establish the initial relationships between micro-parameters and macro properties of rocks for further investigation. Simply, a physical meaningful equation $\Phi(q_1,q_2,...,q_n)=0$, where q_i is a physical variable, can be rewritten in terms of a set of dimensionless parameters $\phi(\pi_1,\pi_2,...,\pi_n)=0$, where π_1 is the dimensionless variable

constructed from the original variable. Therefore, different mechanical properties of FJM can be expressed in term of dimensionless parameters constructed from these micro-parameters.

In this study, the loading rate V, one of the boundary parameters, was removed from the analysis because only the quasi-static loading conditions were considered. For this reason, and based on the work done in previous studies and the PFC manual (Itasca Consulting Group Inc 2014), V is set to 0.02 m/s. Therefore, there are a total of 10 physical parameters, $\{ r_{max}/r_{min}, w/d, N_r, n, k^*, \tan\phi_b, \mu, E^*, c, t\}$ for the FJM, which can be represented by 9 dimensionless parameters: $\{ r_{max}/r_{min}, w/d, N_r, n, k^*, \tan\phi_b, \mu, E^*/c, t/c\}$.

The macro elastic properties, namely E and v, are determined by the E^* and k^* in the elastic regime where no failure occurs (Huang 1999; Potyondy and Cundall 2004). However, the macro-strength properties, such as UCS and TS in the numerical model, depend on both the bond/interface strength parameters and the micro-elastic parameters. Invoking the Buckingham π theorem, the following equations are suggested for the relationships between micro-parameters and macro-parameters (Huang 1999; He and Xu 2015):

$$\frac{E}{E^*} = f_E(k^*, n, N_r) \tag{3.7}$$

$$v = f_v(k^*, n, N_r) \tag{3.8}$$

$$\frac{\sigma_c}{c} = f_c\left(\frac{E^*}{c}, k^*, \frac{t}{c}, \mu, \phi_b, n, N_r\right) \tag{3.9}$$

$$\frac{\sigma_t}{t} = f_t\left(\frac{E^*}{c}, k^*, \frac{t}{c}, \mu, \phi_b, n, N_r\right) \tag{3.10}$$

3 Sensitivity analysis for the effects of individual parameters on the macro-properties

In this section, the influences of micro-structural parameters of the BPM on macro properties were discussed based on both previous studies and current numerical simulations in order to generate a homogenous, isotropic and well-connected granular assembly. A sensitivity analysis was then used to investigate the effects of individual constitutive micro-parameters on macro-rock properties. Parameters that have limited or no effects on the corresponding macro-properties were removed from the relationship. As shown in Fig. 3.4, a rectangular specimen of 54×108 mm, with randomly distributed particles, was used to perform uniaxial compression tests and direct tension tests for sensitivity analysis.

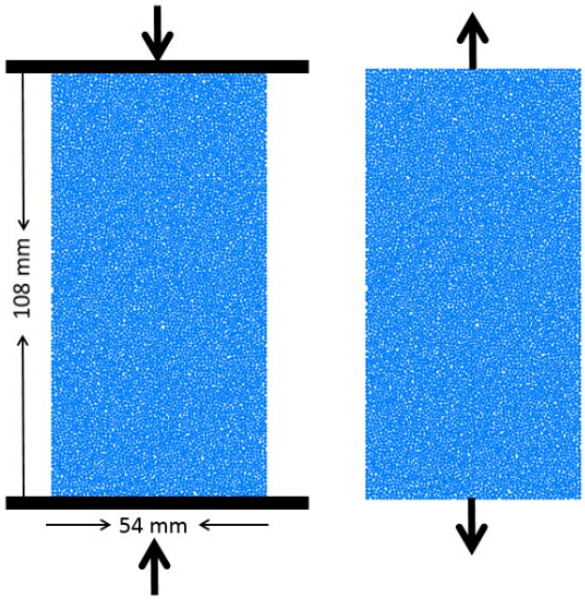

Figure 3.4 Bonded-particle models for the uniaxial compressive test (left) and direct tension test (right).

In modelling compressive loading, see left figure in Fig. 3.4, the UCS test was carried out by moving the top platen downward and the bottom platen upward. However, in modelling tensile loading, both platens were removed and a group of particles at the top and bottom

of the specimen are regarded as “grips”. The direct tensile test was then performed by moving the top grip particles upward and the bottom grip ones downward to create tension within the specimen.

3.1 Micro-structural parameters of the BPM

Micro-structural parameters related to the particle distribution were determined first to generate a well-connected particle assembly based on previous studies, as shown in Table 3.1. The number of elements N_r, ratio of maximum to minimum ball radius r_{max}/r_{min}, porosity n, and ratio of specimen width to the median ball diameter w/d, are discussed below.

3.1.1 The number of elements (N_r)

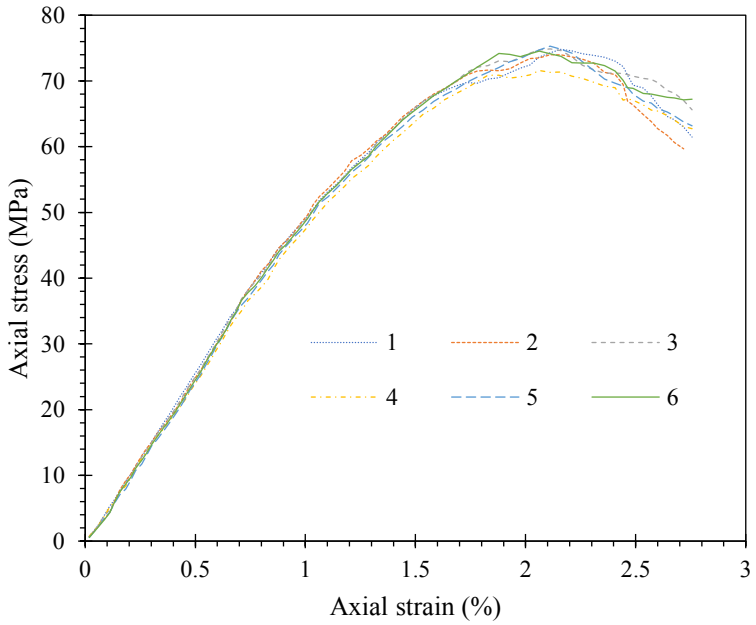

Figure 3.5 Stress-strain curves with different numbers of elements for each bond

Discrete bond elements are first introduced in FJM so their effects on macro rock properties need to be investigated. In this study, we progressively increased the number of elements for each interface from 1 to 6 to examine their impacts on the stress-strain curves of the

specimen and the results are shown in Fig. 3.5, which indicates that the number of elements has limited effect on the mechanical properties of FJM. Note that the calibration study mainly focuses on the mechanical properties (UCS, TS, E and *v*) rather than the failure mode. These properties are fundamental parameters needed for most geomechanical investigations.

The mechanical properties and their corresponding coefficients of variation (COV) are listed in Table 3.2. The results show that the number of elements for each interface has no effect on the tensile strength while it has a very limited effect on the UCS, *E* and *v* with COV less than 2%. Therefore, this variable was removed from further investigations in this study.

Table 3.2 Macro-properties of FJM with different number of elements for each bond and the corresponding COV

Numbers of element	UCS (MPa)	TS (MPa)	*E* (GPa)	*v*
1	75.18	2.03	5.31	0.161
2	74.23	2.03	5.30	0.161
3	75.13	2.03	5.29	0.161
4	72.01	2.03	5.14	0.159
5	75.63	2.03	5.32	0.161
6	74.89	2.03	5.31	0.161
COV (%)	1.76	0.00	1.29	0.51

3.1.2. Ratio of maximum to minimum ball radius (r_{max}/r_{min})

The r_{max}/r_{min} ratio is related to the particle size distribution, and there are mixed conclusions on its influence on the corresponding macro-properties. Ding et al. (2014) indicated that UCS and *E* increase while the ν shows an opposite trend with an increasing r_{max}/r_{min} ratio. Yang et al. (2006), however, pointed out that no obvious effects on *E*, *v* and UCS can be

found based on simulation results. Koyama and Jing (2007) argued that the particle size distribution has very limited effects on the macro-properties (E, v, UCS and TS) when the ratio of specimen width to the median ball radius w/d exceeds a threshold value. Huang (1999) suggested that the particle ratio can be removed from consideration when a particle assembly has a sufficient degree of freedom. Previous investigations (Huang 1999; Yang et al. 2006; Koyama and Jing 2007) show that the r_{max}/r_{min} ratio of published researches falls in the range of 1.32-3.00; and 1.66 is the most common choice for the simulation of brittle rocks. Therefore, to simplify the BPM establishment process, we suggested that the $\frac{r_{max}}{r_{min}}$ ratio is set at 1.66 so it is removed from further considerations.

3.1.3. Porosity (n)

The porosity (n), related to the damage in rock (Xue 2015), in PFC-2D is the ratio of the total void area within the specimen to the total area of the specimen, which is, in general, higher than that of natural rock material. This is because PFC models use circular particles to represent rock grains, which is a major limitation of PFC implementation. Porosity n is a good index for representing particle distribution parameters that are related to the coordination number, defined as the number of contacts per particle. The relationship between the porosity and the coordination numbers was established by Oda et al. (1982). Many studies (Yang et al. 2006; Schöpfer et al. 2007; Ding et al. 2014) indicate that UCS, TS and E decrease with increasing n, while the v is not affected. On the other hand, computational efficiency can be substantially increased as n increases (Yang et al. 2006; Wang et al. 2014) because of the reduction in the numbers of particles.

In this study, to simplify the process, n was removed from further considerations by setting n to the constant value of 0.16, which corresponds to the porosity when the most commonly

used r_{max}/r_{min} ratio of 1.66 is used according to previous studies (Potyondy and Cundall 2004; Yoon 2007; Potyondy 2012).

3.1.4. Ratio of specimen width to the median ball diameter (w/d)

As mentioned earlier, the *w/d* ratio influences the macro-mechanical properties of intact rocks. For FJM, a proper ratio needs to be found for numerical simulations. This ratio also implicitly defines the size of particles that have to be used, given a specific specimen scale. Previous studies covered a wide range of the *w/d* ratio for other bond models, from 5 to 200 (Huang 1999; Potyondy and Cundall 2004). These results indicate that the elastic properties and strength properties suffer large variations when the *w/d* ratio is low, and they converge to a constant value when this ratio is greater than 50 (Koyama and Jing 2007).

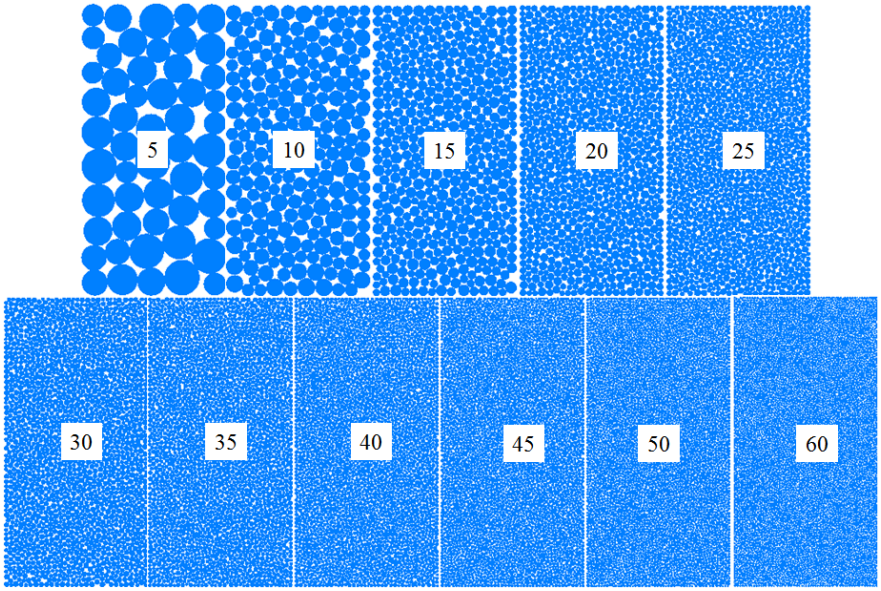

Figure 3.6 The schematic view of a stochastic procedure for BPM model generation. The *w/d* ratio varying from 5 to 60 to create 11 models, with 10 realisations generated for each configuration.

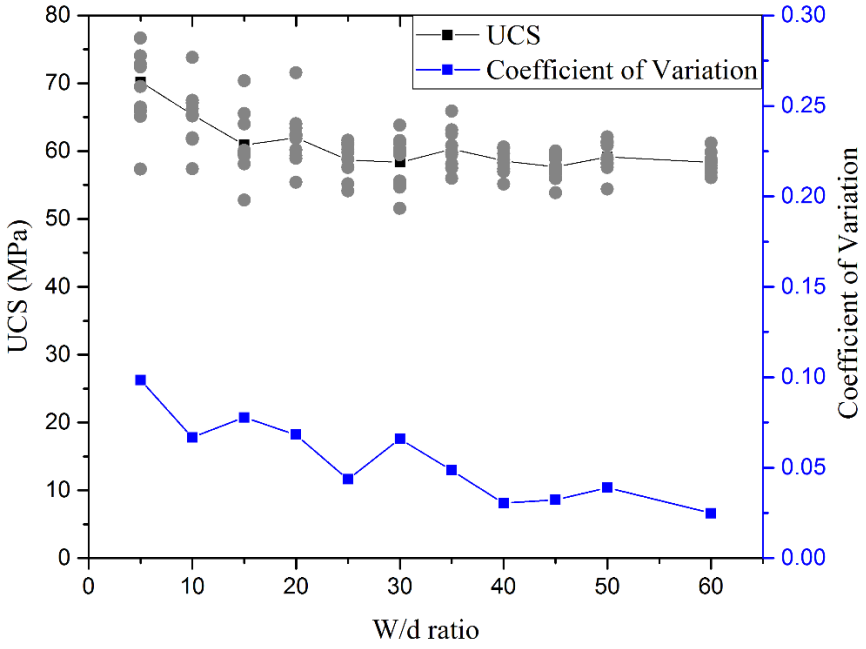
UCS
Coefficient of Variation
UCS (MPa)
Coefficient of Variation
W/d ratio
0
10
20
30
40
50
60
70
80
0.00
0.05
0.10
0.15
0.20
0.25
0.30

(a)

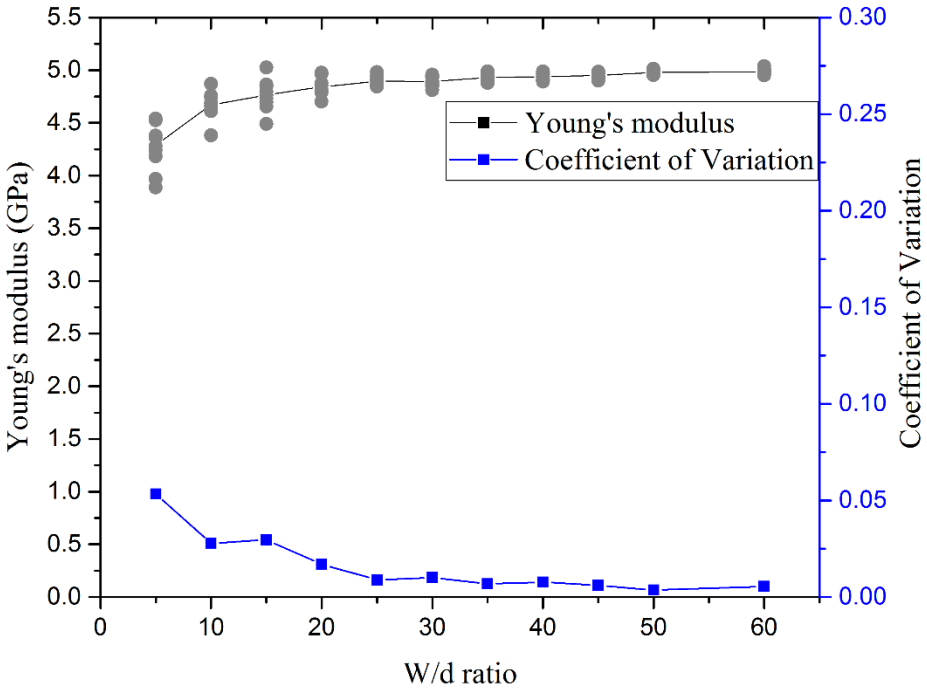
Young's modulus
Coefficient of Variation
Young's modulus (GPa)
Coefficient of Variation
W/d ratio
0.0
0.5
1.0
1.5
2.0
2.5
3.0
3.5
4.0
4.5
5.0
5.5
0
10
20
30
40
50
60
0.00
0.05
0.10
0.15
0.20
0.25
0.30

(b)

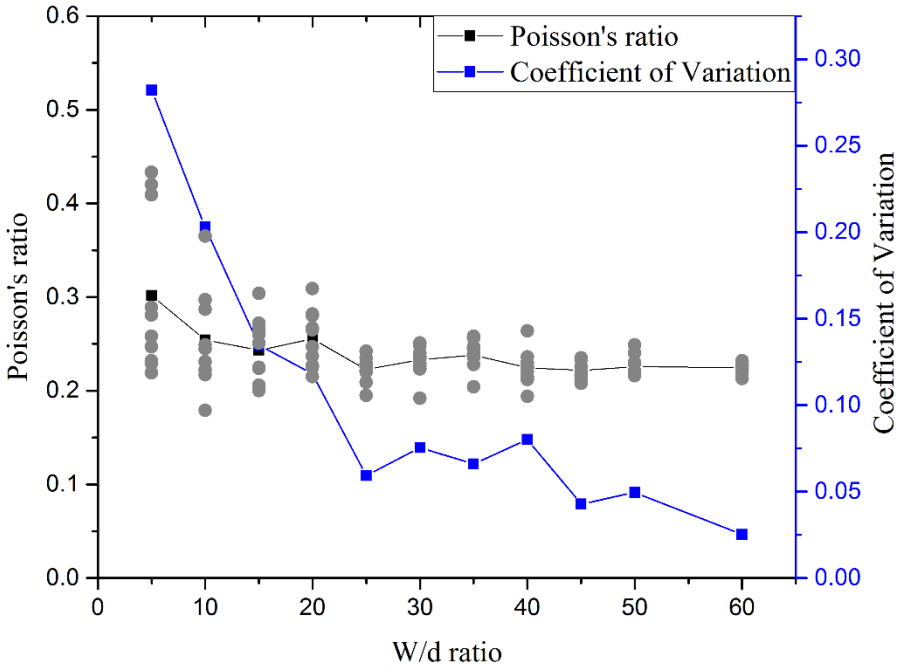

(c)

Figure 3.7 Variations of macro-properties for different w/d ratios, with 10 realizations for each ratio, (a) UCS, (b) *E* and (c) *v*.

To find a suitable value for FJM, we progressively increased the *w/d* ratio from 5 to 60, with 10 stochastic realisations for each ratio to create 11 different numerical models, as shown in Fig. 3.6. In the stochastic realisations, the geometrical properties such as initial position and size are randomly attributed to particles according to different random seeds.

Figure 3.7 shows the scatter plot and mean values of UCS, *E* and *v* versus the *w/d* ratio. The coefficient of variation (COV) is used to evaluate the variability of the macro-properties for different *w/d* ratios, and is also plotted in Fig. 3.7. The results show that the average UCS and *v* decrease while the *E* increases as the *w/d* ratio increases, which is consistent with the results by Koyama and Jing (2007), Schöpfer et al. (2007) and Yoon (2007).

The acceptable COV used to determine a suitable *w*/*d* ratio was set to 5%. The simulation results show that the optimal ratios are 40 and 45 in terms of UCS and ν, but it is found to

be 10 for E because of its low variability with different w/d ratios. Therefore, a minimum w/d ratio of 45 was selected, which ensures that macro-properties such as UCS, E and v converged to a stable value.

To summarize, the final boundary parameters and micro-structural parameters for the FJM that were suitable for simulating the mechanical behaviours of rock materials are summarised in Table 3.3.

Table 3.3 Boundary and microstructure parameters for the FJM

Boundary parameters			Microstructure parameters				
w (mm)	l (mm)	V (m/s)	r_{max}/r_{min}	g_0	N_r	n	w/d
54	108	0.02	1.66	1e-4	3	0.16	45

The determination of these micro-structural parameters is a prerequisite for generating a suitable and consistent homogenous and isotropic particle assembly, for both laboratory-scale investigation and large-scale field application problems. Each numerical model should have enough number of particles to ensure that the model has a large sufficient degree of freedom so that stable and reliable mechanical behaviours can be obtained. At the micro-scale, each particle should have at least three contacts to ensure that the particle in the model is stable and well-connected so that flat-jointed bonds can be properly installed. These contacts are largely influenced by the initial gap g_0 and porosity n. If the micro-structure parameters listed in Table 3.3 are used, the average contact number is 4.08, indicating a well-connected BPM.

3.2 Constitutive parameters

In this section, influences of individual constitutive parameters of FJM on macro-properties such as UCS, TS, E and v are investigated through sensitivity analysis. The initial microscopic constitutive parameters for sensitivity analysis are listed in Table 3.4. The

results are summarised in Fig. 3.8. The macro-properties are normalised by the maximum value of the corresponding macro-properties. Table 3.5 lists the variability of macro-properties for different ranges of constitutive micro-parameters, expressed in the form of coefficient of variation (COV). Detailed discussions of these results are given below.

Table 3.4 Initial constitutive parameters for sensitivity analysis

Stiffness ratio k^*	Effective modulus E^*	Bond tensile strength t	Bond cohesion c	Local friction angle ϕ_b
2	20 (GPa)	4 (MPa)	40 (MPa)	35 (degree)

Table 3.5 COV of macro-properties corresponding to individual parameters

Coefficient of Variation (COV) (%)	E	v	σ_c	σ_t
Stiffness ratio, k^*	5.49	22.38	2.89	2.43
Effective modulus, E^*	62.96	0.35	1.85	0.58
Bond tensile strength, t	0.25	0.38	0.14	18.64
Bond Cohesion, c	0.12	0.24	28.59	0.00
Local Friction angle, ϕ_b	0.14	0.32	69.50	0.00

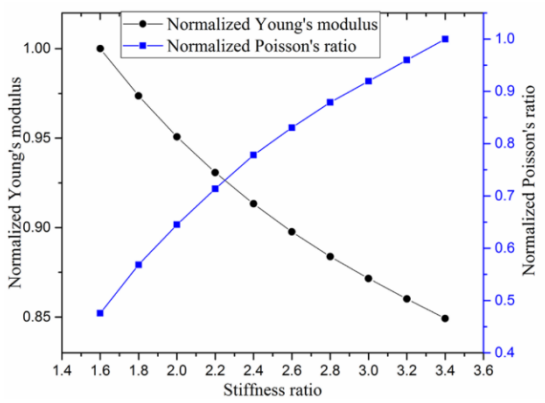
Normalized Young's modulus
Normalized Poisson's ratio
Normalized Young's modulus
Normalized Poisson's ratio
Stiffness ratio

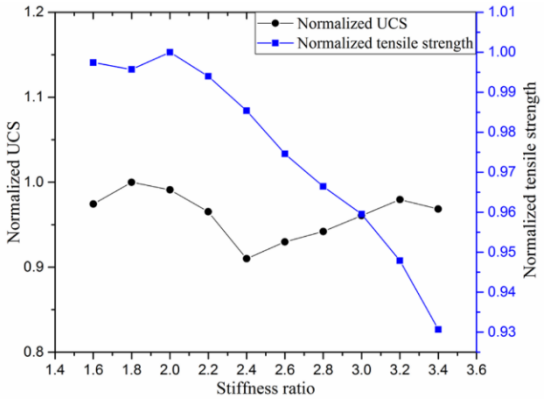
Normalized UCS
Normalized tensile strength
Normalized UCS
Normalized tensile strength
Stiffness ratio

(a)

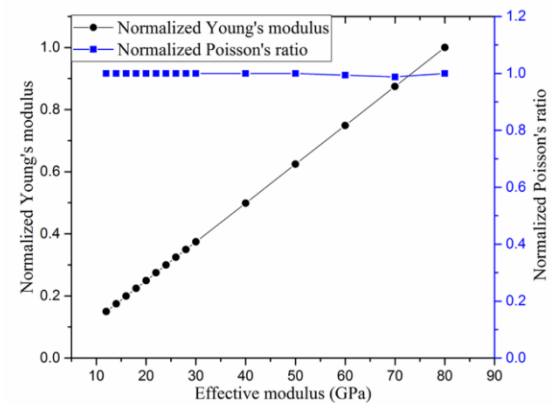
Normalized Young's modulus
Normalized Poisson's ratio
Normalized Young's modulus
Normalized Poisson's ratio
Effective modulus (GPa)

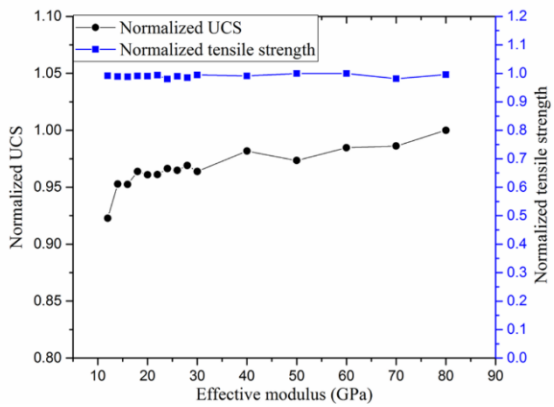
Normalized UCS
Normalized tensile strength
Normalized UCS
Normalized tensile strength
Effective modulus (GPa)

(b)

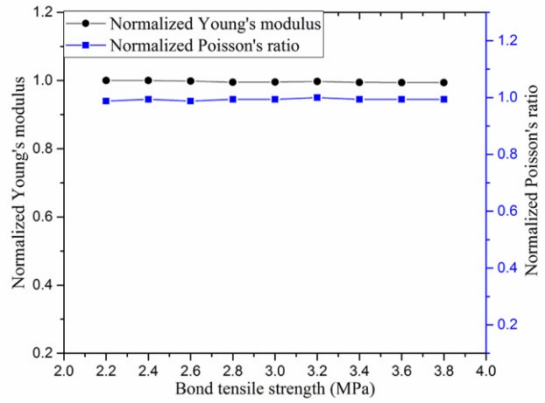
Normalized Young's modulus
Normalized Poisson's ratio
Normalized Young's modulus
Normalized Poisson's ratio
Bond tensile strength (MPa)

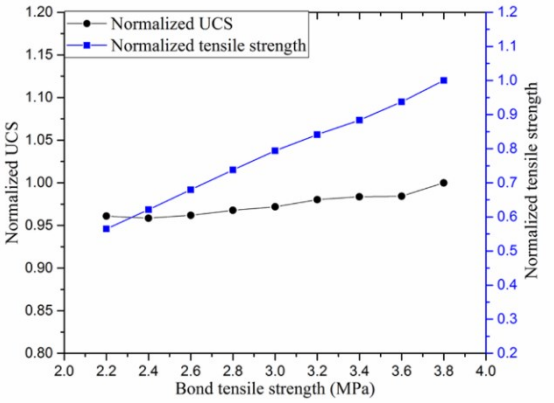
Normalized UCS
Normalized tensile strength
Normalized UCS
Normalized tensile strength
Bond tensile strength (MPa)

(c)

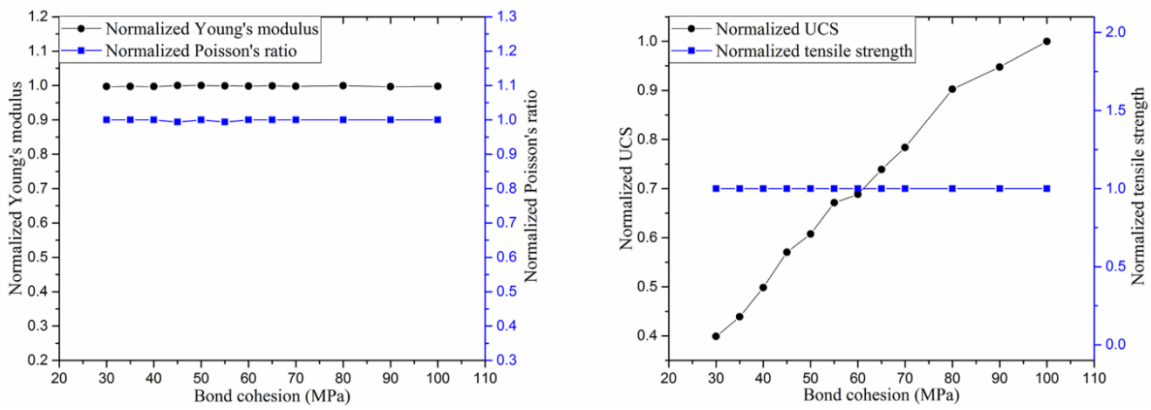

(d)

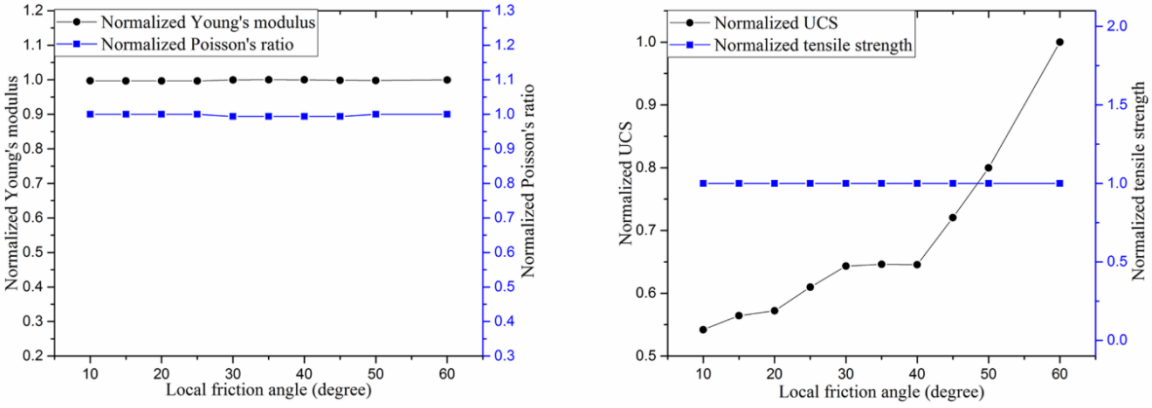

(e)

Figure 3.8 Macro-properties of FJM with variation of individual parameters: (a) stiffness ratio, (b) effective modulus, (c) bond tensile strength, (d) bond cohesion, (e) internal friction angle.

3.2.1 Stiffness ratio (k*)

The effects of k^* on the macro-elastic and strength properties of the synthetic rock, when k^* increases from 1.4 to 3.6, are illustrated in Fig. 3.8a. Obviously, the influences on both E and v are significant. As k^* increases, the E of BPM material decreases, but the v increases. These results for the FJM are consistent with previous works with PBM (Huang 1999; Yang et al. 2006; Fakhimi and Villegas 2007; He and Xu 2015). Therefore, k^* is the dominant factor for calibrating these two macro-elastic properties with the COV of 5.49% and 22.38% respectively, indicating significant variations.

On the other hand, k^* has a limited effect on UCS and TS, with a COV value of only 2.89 % and 2.43%, respectively. Slight decreases in UCS and TS can be seen as k^* increases. However, the tendency for the variation of UCS is not clear, and the benefit of including k^* in the determination of UCS should be further assessed.

3.2.2 Effective modulus (E*)

Young's modulus E is linearly dependent on the E^* for the FJM material (see Fig. 3.8b). The relationship is dominant with a COV of 62.96%, much higher than the COV by other micro-parameters, including k^* discussed above. The influence of E^* on v and TS can be ignored where the corresponding COV is less than 1%. UCS increases slightly when E^* increases, but the corresponding COV value is relatively low at 1.85%.

3.2.3 Bond tensile strength (t)

Elastic properties are found to be independent of t of the FJM, as shown in Fig. 3.8c. These results are consistent with that for PBM. As expected, for the strength properties of BPMs, this parameter dominates the influence on the TS with a linear relationship and a COV value of 18.64%. On the other hand, the UCS increases with increasing t, as local tensile failure causes damages and therefore contributes globally to the strength reduction. As the trend of variation is clear, t was also included in the relationship to determine the UCS of the FJM.

3.2.4 Bond cohesion (c)

The simulation results reveal that the elastic properties (E and v) are independent of c with COV of only 0.12% and 0.24% respectively, see Fig. 8d. This is consistent with previous investigations using PBM. For macro-strength properties, the TS is independent of c and therefore c can be excluded from the function to estimate the TS of FJM material. On the other hand, the UCS of FJM material has a positive linear relationship with c, one of the

primary factors governing the UCS, with a COV of 28.59%. It is strange at the first sight that *c* has effect on UCS but not on TS. This phenomenon, however, lies in the fact that tensile failure and shear failure are governed by two separate parameters *t* and *c* at the particle level due to DEM implementation, as mentioned in Section 2.1.

3.2.5 Local friction angle (ϕ_b)

Finally, the ϕ_b was studied to assess its influences on the macro-properties of FJM (see Fig. 3.8e). As the residual friction angle ϕ_r (Fig. 3.3) only influences the post-peak behaviours (beyond the scope of the current study), but has no effect on the pre-failure macro-properties (Wu and Xu 2016), this parameter is not included further in this study. Figure 8e suggests that ϕ_b has no effect on the *E* and *v*, because ϕ_b will not take any effect until the bond breaks and sliding between particles occurs. For the same reason, the ϕ_b also has no effect on the TS and therefore can be removed from of the relationship for TS. However, the resistance to sliding between particles has the dominant effect on the UCS of FJM with a COV of 69.50%. This is perhaps one of the merits of FJM as resistance to sliding between rock grains at the micro-scale under compression is the behaviour expected from rock materials.

Based on the results discussed above for FJM materials, *E* is affected by *E**and *k** but *v* is only related to *k**. For strength properties, TS is determined by *k** and *t*, while UCS has a more complex relationship with almost all constitutive micro-parameters. Therefore, the initial relationships are modified to give more practical functions below:

$$\frac{E}{E^*} = f_E(k^*) \tag{3.11}$$

$$v = f_v(k^*) \tag{3.12}$$

$$\frac{\sigma_c}{c} = f_c\left(\frac{E^*}{c}, k^*, \frac{t}{c}, \mu, \phi_b\right) \tag{3.13}$$

$$\frac{\sigma_t}{t} = f_t(k^*) \tag{3.14}$$

When employing the Mohr-Coulomb (MC) failure criterion and the deformability method discussed above at the particle level, FJM can reproduce realistic macro-mechanical properties of intact rocks. The deformability properties, such as E and v, are elastic properties before failure and only relate to microscopic deformability parameters such as E^* and k^*. However, the macro-strength properties, UCS and TS, are dependent at the particle level not only on the micro-strength parameters but also the micro-deformability parameters. A possible explanation for this is that the elastic mismatch at the particle level will induce stress related localised tensile failure, which may evolve into shear failure at the global scale.

4 Regression analysis

The simplified relationships listed above can be further quantified using regression analysis based on numerical simulation results. We used linear regression, non-linear regression and multivariate regression techniques to obtain the best-fit relationships for different macro-properties. This section presents these relationships in the order of complexity. The determination of v is the simplest, because it only depends on k^* as discussed above. Then, the relationships for E and TS are described, because they depend on two micro-parameters: E^* and k^*, t and k^*, respectively. The last relationship described is for UCS as it depends on all micro-parameters. This order of relationships should also be followed in practice to derive micro-parameters for FJM in order to match a set of given macro-rock properties. The macro-mechanical properties of BPM are derived from stress-strain curves: E and v

can be obtained in the elastic region and UCS and TS can be derived at the peak of stress-strain curves under uniaxial compression tests and direct tension tests, respectively.

4.1 Poisson's ratio

Based on the sensitivity analysis conducted, Poisson's ratio v of FJM materials is mainly determined by k^*. In this study, the range of v covered by our numerical simulations was between 0.10 and 0.35 as shown in Fig. 3.9, which is the value range for most rock materials (Alejandro 2013). The best, non-linear regression gives the following expression:

$$v=0.155\,ln\,(k^*)+0.053,\ R^2=0.995 \tag{3.15}$$

A closed-form expression for v can be derived using a microstructure continuum approach (Chang and Misra 1990; Bathurst and Rothenburg 1992). The expression, as derived in Chang and Misra (1990) is:

$$v=\frac{k^*-1}{4k^*+1} \tag{3.16}$$

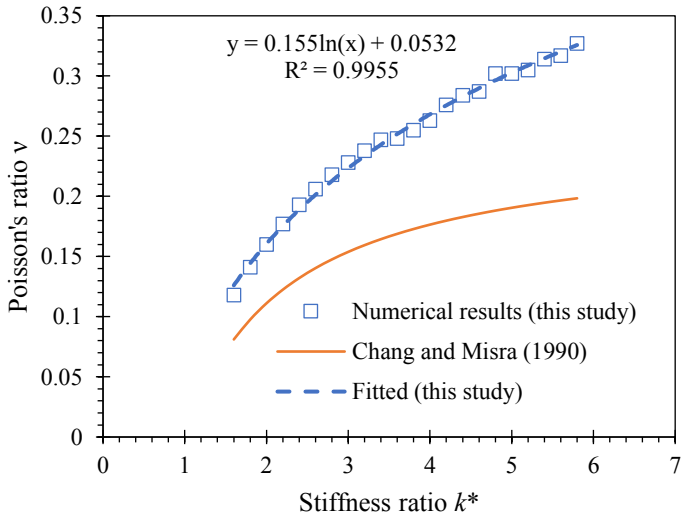

Figure 3.9 Effect of k^* on Poisson's ratio and a comparison with existing analytical solution

This relationship is also plotted in Fig. 3.9 as a comparison. This analytical solution suggests that v has a non-linear relationship with k^*. However, this closed-form solution gives an upper limit of 0.25 for v, which is inconsistent with laboratory data. Based on our proposed relationship, k^* for FJM should be less than 20 so a realistic v can be obtained.

4.2 Young's modulus

Young's modulus was determined by E^* and k^* of the FJM, see Eq. 3.11. The numerical simulation results are shown in Fig. 3.10 suggest that a ratio of E to E^* has a non-linear relationship with the k^*. The best-fit relationship is:

$$E = E^*[-0.185\ln(k^*) + 1.151], R^2 = 0.991 \tag{3.17}$$

An analytical solution for E was also derived in Chang and Misra (1990):

$$E = \frac{2r^2 N K_n}{3V}\left(\frac{2k^* + 3}{4k^* + 1}\right) \tag{3.18}$$

where r is the radius of the particle, N is the number of contacts, K_n is the normal stiffness of contact and V is the volume of packing. The expression obtained by non-linear regression analysis is similar to the closed-form analytical equation (Eq. 3.18).

As a comparison, the analytical solution is also plotted in Fig. 3.10. An obvious discrepancy can be seen when k^* is less than 3, but the difference gradually disappears when k^* is greater than 3.

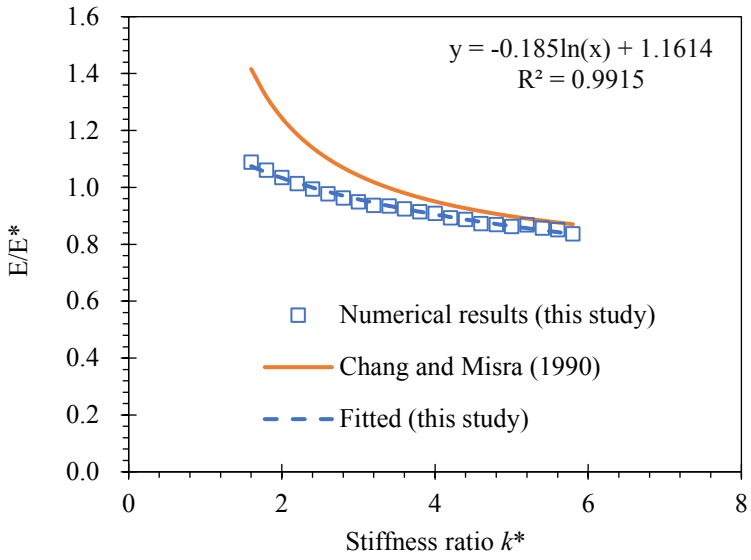

Figure 3.10 Effects of k^* on the ratio of Young's modulus to the effective modulus and a comparison with existing analytical solution

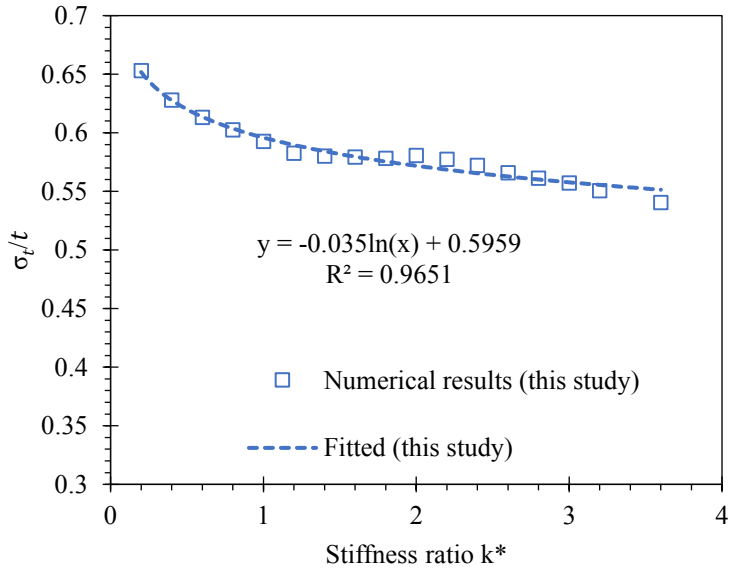

Figure 3.11 Effects of k^* on the ratio of tensile strength to effective tensile strength

4.3 Tensile strength

Unlike elasticity properties, no closed-form solutions can be found to link strength properties such as UCS and TS to micro-parameters of BPM. Using dimensionless analysis

and numerical simulation results, the relationship between the ratio σ_t/t and k^* can be established by non-linear regression, see Fig. 3.11. The expression is:

$$\sigma_t = t\left[-0.035\, ln\left(k^*\right) + 0.596\right],\ R^2 = 0.965 \tag{3.19}$$

4.4 Uniaxial compressive strength

The UCS of FJMs demonstrates a complex, multivariate relationship with the whole set of micro-constitutive parameters, including c, t and ϕ_b, E^* and k^*. Based on the dimensionless analysis, the multivariate regression of the simulation results gives the following relationship between UCS and the micro-parameters mentioned above. The relationship is determined through regression analysis of 85 sets of micro-constitutive parameters used for uniaxial compressive tests, as shown below:

$$\frac{\sigma_c}{c} = -0.056k^* + 0.777tan\phi_b + 0.1419\frac{E^*}{c} + 2.126\frac{t}{c} + 1.167,\ R^2 = 0.922 \tag{3.20}$$

4.5 Calibration procedure

The obtained relationships described above can be used to estimate the micro-constitutive parameters needed for applying the FJM for geomechanical analysis. In this study, the local friction angle ϕ_b was first arbitrarily determined, as it is only related to post-peak behaviours (Vallejos et al. 2016; Wu and Xu 2016). The following procedure should be used to derive a set of suitable micro-mechanical parameters for the FJM in order to match a set of macro-rock properties, in addition to the geometrical parameters listed in Table 3.3:

1. Estimate the stiffness ratio k^* through Eq. 3.15 to match Poisson's ratio v;
2. Estimate the effective modulus E^* through Eq. 3.17, with the stiffness ratio k^* determined in step 1 to match Young's modulus E;
3. Estimate the bond tensile strength t through Eq. 3.19, with the stiffness ratio k^* determined in step 1 to match tensile strength;

4. Estimate the bond cohesion c through Eq. 3.20 with stiffness ratio k^* determined in step 1, effective modulus E^* in step 2, bond tensile strength t in step 3, and pre-determined local friction angle ϕ_b to match UCS.

The proposed UCS model has a complex, multivariate relationship with micro-parameters and therefore great care should be taken to ensure if the desired UCS value can be achieved after all micro-parameters are obtained. If it is necessary to adjust the value of UCS, c can be altered until the desired UCS value is obtained as this will not affect other micro- or macro-properties because c only appears in the relationship for UCS.

Table 3.6 The comparison between experimental data and numerical simulation results of macroscopic mechanical properties of four types of rocks

Rock types		UCS (MPa)	TS (MPa)	E (GPa)	v
Avro granite	Experiment	192.00	13.00	72.00	0.200
(Olofsson and Fredriksson 2005)	Numerical	188.53	13.05	72.23	0.204
	COV (%)	1.289	0.271	0.225	1.400
Sandstone	Experiment	107.50	11.30	35.40	0.252
(Peng and Zhang 2007)	Numerical	92.39	11.36	35.42	0.255
	COV (%)	10.690	0.374	0.039	0.836
Transjurane sandstone	Experiment	40.00	2.80	12.50	0.300
(Peng and Zhang 2007)	Numerical	38.04	2.80	12.59	0.295
	COV (%)	3.550	0.000	0.507	1.188
Coal	Experiment	22.30	0.88	18.48	0.303
(Peng and Zhang 2007)	Numerical	22.62	0.927	18.71	0.287
	COV (%)	1.007	3.678	0.874	3.835
	R^2	0.9925	0.9999	0.9999	0.9832
	AAREP	6.190%	1.495%	0.579%	2.062%

5 Validation

In order to evaluate the effectiveness of the proposed empirical relationships in constructing a FJM, four different types of rocks, with different combinations of strength and elasticity

properties, were used. The macro-properties of these rocks are listed in Table 3.6. The procedure proposed in Section 3.4 was employed to obtain the micro-constitutive parameters for the selected rocks, as listed in Table 3.7.

Table 3.7 Summary of micro constitutive parameters used for the rocks studied

Rock types	Stiffness ratio k*	Effective modulus E*(GPa)	Bond tensile strength (MPa)	Bond cohesion (MPa)	Local friction angle (degree)
A-granite	2.582	73.774	23.102	84.530	35.000
Sandstone	3.610	38.734	20.509	38.710	35.000
T-sandstone	4.919	14.591	5.184	18.740	35.000
Coal	5.015	21.662	1.631	11.010	35.000

A-granite: Avro granite; T-sandstone: Transjurane sandstone

Numerical simulations were then performed to obtain the macro-mechanical parameters of the numerical models constructed using these micro-parameters. The numerical results are listed in Table 3.6 for comparison. The coefficient of variation (COV) in this case is used to quantify the discrepancy between the numerical results and the experimental data. The results show that the values of *E*, *v* and TS can be reproduced very well with COV less than 2%. The value of UCS, on the other hand, has a higher COV, ranging from 1.0% to 10.7%. This suggests greater difficulty in reproducing the UCS accurately, which is expected because of its complex relationships with almost all micro-parameters. However, the *c*, in this case, can be adjusted further to reduce the COV value for the UCS if desired.

For example, in order to better match the value of UCS for the sandstone, *c* was gradually increased until the desired UCS value was obtained. In this case, the *c* was increased to 45 MPa while keeping the other constitutive parameters unchanged. This caused the UCS

value of the sandstone to increase from 92.39 to 106.29 MPa, with a COV value of only 0.800%.

To investigate the reliability of the proposed method, the predicted macro-properties of rocks, based on numerical simulations, were compared with the experimental data in more detail. In this process, the regression R-squared value (R^2) and the average absolute relative percentage error (AAREP) were used as a measurement of discrepancy for the assessment (Shen et al. 2014):

$$R^2 = 1 - \frac{\sum_{i=1}^{N}\left(M_{R,i}^{obs} - M_{R,i}^{pred}\right)^2}{\sum_{i=1}^{N}\left(M_{R,i}^{obs} - M_{R,i}^{av}\right)^2} \tag{3.21}$$

$$\text{AAREP} = \frac{\sum_{i=1}^{N}\left|\frac{M_{R,i}^{pre} - M_{R,i}^{obs}}{M_{R,i}^{obs}}\right|}{N} \tag{3.22}$$

where N is the total number of numerical simulations, $M_{R,i}^{obs}$ and $M_{R,i}^{pred}$ are experimental value and numerical value, respectively, and $M_{R,i}^{av}$ is the average of the numerically determined values.

The values of these discrepancy measurements are listed in Table 3.6. A visual comparison between experimental data and simulation results of four macro-properties is given in Fig. 3.12. A close agreement was observed between the data and the numerical results. The values of R^2 for all macro-properties were higher than 0.98, and the values of AAREP were less than 3%, excepting UCS, for which AAREP=6.19%.

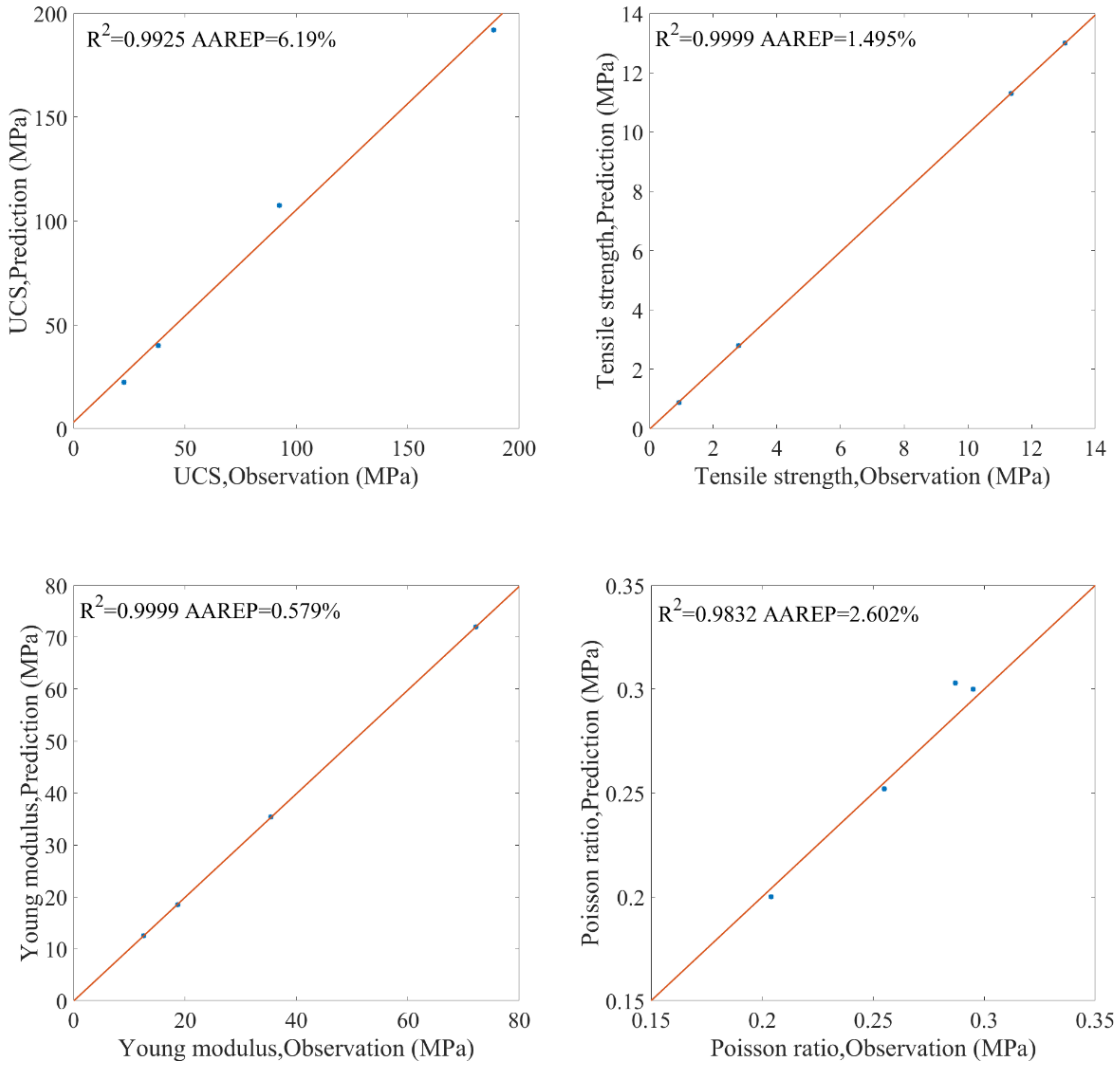

Figure 3.12 Prediction performances for different macro-properties

To evaluate the reliability of the proposed method when micro structure parameters change, the effect of different *w/d* ratio was further assessed. For Hawkesbury sandstone, numerical models with *w/d*=67.5, using parameters listed in Table 3.8 (as predicted by the proposed model) were subjected to uniaxial compression and direct tension tests to derive mechanical properties. The COV values of TS, *E* and *v* were all below 3%, which is considered an acceptable level of discrepancy. However, the COV value of UCS was 10.08, indicating that *c*, in this case, may be adjusted further to reduce the COV value for the UCS if desired.

Table 3.8 The comparison between experimental data and numerical simulation results of the macro-mechanical properties of Hawkesbury sandstone, with *w/d*=67.5

Rock type		UCS (MPa)	TS (MPa)	E (GPa)	v
Hawkesbury sandstone	Experiment	50.8	4	11	0.2
	Numerical	58.60	4.08	11.14	0.194
	COV (%)	10.08	1.40	0.89	2.15

6 Conclusions

When using flat-jointed BPMs, one may encounter tedious and time-consuming calibration procedures to find a suitable set of parameters that can be used to generate a proper numerical specimen for geotechnical investigations of intact rocks if a trial and error approach is used. In order to solve this problem, a systematic approach to simplify the calibration procedure is proposed. Based on dimensionless analysis, sensitivity analysis, regression analysis and numerical simulation results, four relationships between macro-rock properties such as UCS, TS, E and v, and micro–parameters of the flat-jointed BPM such as k^*, E^*, t, c and ϕ_b were derived to facilitate the proposed parameter derivation procedure.

When determining the micro-parameters for the flat-jointed BPM, after the structural parameters (such as N_r , n, r_{max}/r_{min} and w/d) are determined, k^* should be determined based on the desired v first. E^* should then be determined to match E of the rock material, followed by t based on the TS of the rock material. Finally, the c should be determined to match the desired UCS.

The effectiveness and robustness of this approach were confirmed by the close agreement between the numerical results and the experimental results including both pre-peak and post-peak stages. Note that some additional minor adjustments of c may be necessary to

achieve a better match for the derived UCS, as demonstrated in the validation test for the sandstone example.

Abbreviations

BPM Bonded-particle model

DEM Discrete element method

PFC The particle flow code

LBM The linear-bond model

PBM The parallel-bond model

FJM The flat-jointed model

UCS Uniaxial compressive strength

TS Tensile strength

COV Coefficient of variation

MC Mohr-Coulomb

R^2 The regression R-squared value

AAREP The average absolute relative percentage error

Acknowledgement

Scholarship support for the first author provided by China Scholarship Council (CSC) is gratefully acknowledged. The authors would like to thank Leticia Mooney for her editorial support during the preparation of this paper.

References

Alejandro J (2013) Considerations for discrete element modeling of rock cutting (Doctoral dissertation). University of Pittsburgh.

Bathurst RJ, Rothenburg L (1992) Investigation of micromechanical features of idealized granular assemblies using DEM. Eng Comput 9:199–210.

Chang CS, Misra A (1990) Packing structure and mechanical properties of granulates. J Eng Mech 116:1077–1093.

Cho N, Martin CD, Sego DC (2007) A clumped particle model for rock. Int J Rock Mech Min Sci 44:997–1010.

Cundall PA (1971) A computer model for simulating progressive, large-scale movements in blocky rock systems. In: The International Symposium on Rock Mechanics. pp 47–65.

Cundall PA, Strack ODL (1979) A discrete numerical model for granular assemblies. Géotechnique 29:47–65.

Ding X, Zhang L, Zhu H, Zhang Q (2014) Effect of model scale and particle size distribution on PFC3D simulation results. Rock Mech Rock Eng 47:2139–2156.

Duan K, Kwok CY, Tham LG (2015) Micromechanical analysis of the failure process of brittle rock. Int J Numer Anal Methods Geomech 39:618–634.

Fakhimi A, Villegas T (2007) Application of dimensional analysis in calibration of a discrete element model for rock deformation and fracture. Rock Mech Rock Eng 40:193–211.

He X, Xu C (2015) Discrete element modelling of rock cutting: from ductile to brittle

transition. Int J Numer Anal Methods Geomech 39:1331–1351.

Huang H (1999) Discrete element modeling of tool-rock interaction (Doctoral dissertation). The University of Minnesota.

Itasca Consulting Group Inc (2014) PFC2D/3D (Particle Flow Code in 2/3 Dimensions), Version 5.0. Minneapolis.

Koyama T, Jing L (2007) Effects of model scale and particle size on micro-mechanical properties and failure processes of rocks-A particle mechanics approach. Eng Anal Bound Elem 31:458–472.

Labuz JF, Zang A (2012) Mohr-Coulomb Failure Criterion. Rock Mech Rock Eng 45:975–979.

Ning J, Liu X, Tan Y, Wang J, Tian C (2015) Relationship of box counting of fractured rock mass with hoek-brown parameters using particle flow simulation. Geomech Eng 9:

Olofsson I, Fredriksson A (2005) Strategy for a numerical rock mechanics site descriptive model.

Peng S, Zhang J (2007) Engineering geology for underground rocks. Eng Geol Undergr Rocks 1–319.

Potyondy DO (2012) A flat-jointed bonded-particle material for hard rock. In: 46th US Rock mechanics/geomechanics symposium. American Rock Mechanics Association.

Potyondy DO, Cundall PA (2004) A bonded-particle model for rock. Int J Rock Mech Min Sci 41:1329–1364.

Schöpfer MPJ, Childs C, Walsh JJ (2007) Two-dimensional distinct element modeling of

the structure and growth of normal faults in multilayer sequences: 1. Model calibration, boundary conditions, and selected results. J Geophys Res 112: B10401.

Shen J, Jimenez R, Karakus M, Xu C (2014) A simplified failure criterion for intact rocks based on rock type and uniaxial compressive strength. Rock Mech Rock Eng 47:357–369.

Sonin AA (2004) A generalization of the Pi-theorem and dimensional analysis. Proc Natl Acad Sci U S A 101:8525–6.

Tian WL, Yang SQ (2017) Experimental and numerical study on the fracture coalescence behavior of rock-like materials containing two non-coplanar filled fissures under uniaxial compression. Geomech Eng 12:541–560.

Vallejos JA, Salinas JM, Delonca A, Mas Ivars D (2016) Calibration and verification of two bonded-particle models for simulation of intact rock behavior. Int J Geomech 17:06016030.

Vesga LF, Vallejo LE, Lobo-Guerrero S (2008) DEM analysis of the crack propagation in brittle clays under uniaxial compression tests. Int J Numer Anal Methods Geomech 32:1405–1415.

Wang Z, Ruiken A, Jacobs F, Ziegler M (2014) A new suggestion for determining 2D porosities in DEM studies. Geomech Eng 7:665–678.

Wu S, Xu X (2016) A study of three intrinsic problems of the classic discrete element method using flat-joint model. Rock Mech Rock Eng 49:1813–1830.

Xu WJ, Li CQ, Zhang HY (2015) DEM analyses of the mechanical behavior of soil and soil-rock mixture via the 3D direct shear test. Geomech Eng 9:815–827.

Xue X (2015) Study on relations between porosity and damage in fractured rock mass. Geomech Eng 9:15–24.

Yang B, Jiao Y, Lei S (2006) A study on the effects of microparameters on macroproperties for specimens created by bonded particles. Eng Comput 23:607–631.

Yoon J (2007) Application of experimental design and optimization to PFC model calibration in uniaxial compression simulation. Int J Rock Mech Min Sci 44:871–889.

Zhang Y, Zhao X (2016) Characterisation of confinement effect on jointed rock pillars using a Synthetic Rock Mass approach. Int J Numer Anal Methods Geomech 40:1690–1711.

Zhao W, Huang R, Yan M (2015) Mechanical and fracture behavior of rock mass with parallel concentrated joints with different dip angle and number based on PFC simulation. Geomech Eng 8:757–767.

Zhou C, Xu C, Karakus M, Shen J (2018) A systematic approach to the calibration of micro-parameters for the flat-jointed bonded particle model. Geomech Eng 16:471–482.

Zhou L, Chu X, Zhang X, Xu Y (2016) Numerical investigations on breakage behaviour of granular materials under triaxial stresses. Geomech Eng 11:639–655.

Chapter 4 The rate-dependency mechanical properties of the jointed rock mass considering joint orientation using a particle mechanics approach

(Paper 2)

Changtai Zhou[1], Chaoshui Xu[1], Murat Karakus[1], Jiayi Shen[2]

[1]School of Civil, Environmental and Mining Engineering, The University of Adelaide, Adelaide, Australia

[2]Institute of Port, Coastal and Offshore Engineering, Zhejiang University, Hangzhou, China

Statement of Authorship

Title of Paper	The rate-dependency mechanical properties of the jointed rock mass considering joint orientation using a particle mechanics approach
Publication Status	☐ Published ☐ Accepted for Publication ☑ Submitted for Publication ☐ Unpublished and Unsubmitted w ork w ritten in manuscript style
Publication Details	Submitted to International Journal for Numerical and Analytical Methods in Geomechanics and currently under revision.

Principal Author

Name of Principal Author (Candidate)	Changtai Zhou		
Contribution to the Paper	Conducted the research and w rote the manuscript.		
Overall percentage (%)	85%		
Certification:	This paper reports on original research I conducted during the period of my Higher Degree by Research candidature and is not subject to any obligations or contractual agreements with a third party that w ould constrain its inclusion in this thesis. I am the primary author of this paper.		
Signature		Date	17/02/2019

Co-Author Contributions

By signing the Statement of Authorship, each author certifies that:

i. the candidate's stated contribution to the publication is accurate (as detailed above);

ii. permission is granted for the candidate in include the publication in the thesis; and

iii. the sum of all co-author contributions is equal to 100% less the candidate's stated contribution.

Name of Co-Author	Chaoshui Xu		
Contribution to the Paper	Supervised the research and reviewed the manuscript.		
Signature		Date	18/02/2019

Name of Co-Author	Murat Karakus		
Contribution to the Paper	Supervised the research and reviewed the manuscript.		
Signature		Date	18/02/2019

Name of Co-Author	Jiayi Shen		
Contribution to the Paper	Supervised the research and reviewed the manuscript.		
Signature		Date	18/02/2019

Abstract

In nature, several forms of anisotropy in rocks, resulting from the presence of bedding planes, joints and weak layers, strongly influence the mechanical properties of the jointed rock mass, which can be critically important to the stability of surface or underground rock excavation. However, the anisotropic characteristic is often ignored by the existing uniaxial dynamic failure criteria. The pre-existing persistent joint effect on the rate-dependency mechanical properties of the jointed rock masses is investigated by a particle mechanical approach, bonded particle model (BPM). First, the capabilities of simulating jointed rock masses and capturing rate-dependency mechanical properties for BPM are validated by the comparison BPM simulation results to the previous experimental results. Then a dynamic strength model is proposed based on the Jaeger's criterion and simulation results. To further investigate the dynamic behaviours, the dynamic UCS for the anisotropic rock masses with various joint orientation are investigated by subjected the BPM models UCS tests with various strain rate. The proposed dynamic strength model is validated based on the simulation results using discrepancy indicators. Then, the fragmentation characteristics of the jointed rock masses are presented and indicate that the failure mode may affect the dynamic UCS. This is further confirmed by carrying out the analysis orientations of microscopic cracks from a micro-mechanical perspective.

Keywords: Jaeger's criterion; uniaxial compression; bonded particle model; loading rate; anisotropy

List of symbols:

σ_{ud} (MPa)	Uniaxial dynamic compressive strength
σ_{us} (MPa)	Uniaxial static compressive strength
C	Material constant
RSC_d	The dynamic rock strength constant of the granite
ε_s (s^{-1})	The static strain rate, which has different values in different references
ε_r (s^{-1})	The reference strain rate
ε_d (s^{-1})	The dynamic strain rate
a	Material constant
n	Material constant
σ_{1d} (MPa)	The dynamic triaxial compressive strength
σ_1 (MPa)	The major principal stress
σ_3 (MPa)	The minor principal stress
c_d (MPa)	Dynamic cohesion
φ (°)	Internal friction angle
m	Hoek-Brown constant for rock material
COV (%)	Coefficient of Variation
w/d	Ratio of maximum to minimum ball radius
g/r_{min}	Ratio of installation-gap
n_p	Porosity
N_r	Number of elements
E^*(GPa)	Bond modulus
k^*	Stiffness ratio

μ	Friction coefficient
t (MPa)	Bond tensile strength
c (MPa)	Bond cohesion
Φ_b (°)	Bond friction angle
c_j (MPa)	Joint cohesion
ϕ_j (°)	Joint friction angle
β (°)	Joint orientation
R^2	Regression R-squared value
AAREP	The average absolute relative percentage error
$\sigma_{us(normalized)}$	The normalized static UCS predicted by the Jaeger's prediction
A, B, C	The coefficient parameter based on the simulation results
A_{90}	Regression value for A when $\beta = 90°$
B_{90}	Regression value for B when $\beta = 90°$
N	The total number of numerical simulations
$M_{R,i}^{obs}$	Simulation results
$M_{R,i}^{pred}$	Theoretical predications
$M_{R,i}^{av}$	Average of the simulation determined values.

1 Introduction

It is well known that the dynamic mechanical properties of rocks are different from those measured in quasi-static conditions (Zhang and Zhao 2014). For many engineering applications, including drilling and blasting, which deal with dynamic behaviours of rocks, a full understanding of the rate-dependent mechanical properties of rocks is important as dynamic behaviours will be the key to assess rock dynamic failure such as rock burst in high-stress conditions.

Published investigations revealed that the mechanical properties of rocks (Brace and Jones 1971; Li et al. 2004; Jacson et al. 2008; Doan and Billi 2011; Fuenkajorn et al. 2012; Liu and Xu 2015; Wasantha et al. 2015) are markedly influenced by the strain rate imposed on them, which can be regarded as the dynamic behaviours. These mechanical properties include properties such as strength (Doan and Billi 2011), elastic modulus (Brace and Jones 1971) and fracture toughness (Kim and Chao 2007; Feng et al. 2017). Experimental results (Brace and Jones 1971; Wasantha et al. 2015) show that rock failure strength is positively correlated with strain rate. With respect to the logarithmic scale of the strain rate, the strength increases slowly at lower strain rate but after a critical strain rate, the strength increases sharply, as shown in Fig. 4.1. The critical strain rate depends on the type of rock and is generally in the range of 10^{-1} and 10^{3} s^{-1} (Blanton 1981; Cai et al. 2007; Zhang and Zhao 2014; Zhu et al. 2015), which coincides with the range of intermediate strain rates (Cadoni 2010). The dynamic behaviour of rocks within this range of strain rates is, therefore, the focus of this work and the understanding of such behaviour can help predict the critical strain rate. Note in this paper, the term of dynamic behaviour is used loosely to refer to the rate-dependent behaviour of rock materials within the range of intermediate strain rates.

Table 4.1 Semi-empirical relationships for the estimation of the rate-dependent dynamic strength of rock-like materials (modified Zhang and Zhao 2014)

Material type	Semi-empirical equation	$\dot{\varepsilon}$ (s^{-1})	Material constants	References
Granite	$\sigma_{ud} = Clog(\varepsilon) + \sigma_{us}$	10^{-8}-10^{4}	C=13 MPa/log(s^{-1}), σ_{ud}=340 MPa	(Masuda et al. 1987)
Granite	$\sigma_{ud} = RSC_d log\left(\frac{\varepsilon}{\varepsilon_s}\right) + \sigma_{us}$	10^{-8}-10^{0}	RSC_d=11.9 MPa, σ_{us}=170 MPa, $\varepsilon_s = 0.5 - 1\ s^{-1}$	(Zhao et al. 1999)
Rocks	$\sigma_{ud} = a\varepsilon^n$	10^{0}-10^{5}	$n_{max} = \frac{1}{3}$	(Grady and Lipkin 1980)
Granites	$\sigma_{ud} \propto \varepsilon^{\frac{1}{1+n}} (\varepsilon < 10^2 s^{-1})$ $\sigma_{ud} \propto \varepsilon^{0.3} (\varepsilon \geq 10^2 s^{-1})$	10^{-6}-10^{3}	n=130	(Lankford 1981)
Basalts	$\sigma_{ud} \propto \varepsilon^{\frac{1}{1+n}} (\varepsilon < 10^2 s^{-1})$ $\sigma_{ud} \propto \varepsilon^{0.3} (\varepsilon \geq 10^2 s^{-1})$	10^{-6}-10^{3}	n=130	(Lankford 1981)
Limestone	$\sigma_{ud} \propto \varepsilon^{\frac{1}{144}} (\varepsilon < 10^2 s^{-1})$ $\sigma_{ud} \propto \varepsilon^{0.31} (\varepsilon \geq 10^2 s^{-1})$	10^{-4}-10^{4}		(Green and Perkins 1968)
Tuff	$\sigma_{ud} \propto \varepsilon^{0.007} (\varepsilon < 76 s^{-1})$ $\sigma_{ud} \propto \varepsilon^{0.35} (\varepsilon \geq 76 s^{-1})$	10^{-6}-10^{3}		(Olsson 1991)
concrete	$\sigma_{ud} = \sigma_{us}\left(\frac{\varepsilon}{\varepsilon_s}\right)^{1.026\alpha_s} (\varepsilon < 30 s^{-1})$ $\sigma_{ud} = \sigma_{us}\gamma_s\left(\frac{\varepsilon}{\varepsilon_s}\right)^{\frac{1}{3}} (\varepsilon \geq 30 s^{-1})$	10^{-5}-10^{3}	$\alpha_s = \frac{1}{5 + \frac{\sigma_{us}}{10}}$ $\gamma_s = 10^{6.156\alpha_s - 2.0}$ $\varepsilon_s = 3.0 \times 10^{-5} s^{-1}$	(Malvar et al. 1998)

Note: σ_{ud} and σ_{us} are uniaxial dynamic compressive strength and uniaxial static compressive strength; C is a material parameter; RSC_d is the dynamic rock strength constant; ε_s is the static strain rate, which has different values in different studies, but falls in the range between 10^{-5} to 10^{-1} s^{-1}; a and n are constants; $\dot{\varepsilon}$ is the valid range of strain rate.

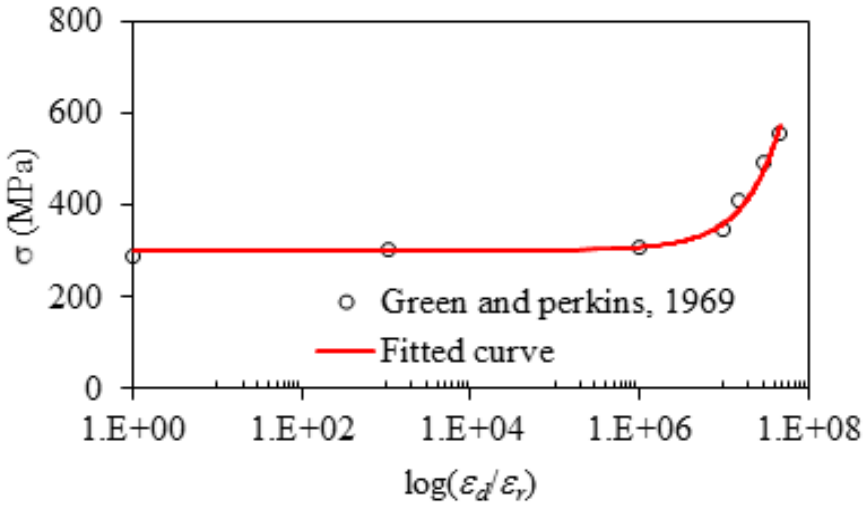

Figure 4.1 The uniaxial compressive strength of Solnhofen limestone at various strain rates (Green and Perkins 1968)

Table 4.2 Dynamic failure criterion for intact rock

Failure criterion	Modified equation	Comments	References
Mohr-Coulomb criterion	$\sigma_{1d} = \sigma_{ud} + \sigma_3 \frac{1+sin\varphi}{1-sin\varphi}$ $c_d = \frac{\sigma_{ud}(1-sin\varphi)}{2cos\varphi}$	φ is hardly influenced by ε only applicable for low confining stress	(Zhao 2000)
Hoek-Brown criterion	$\sigma_{1d} = \sigma_3 + \sigma_{ud}\left(\frac{m\sigma_3}{\sigma_{ud}} + 1.0\right)^{0.5}$	m is not affected by ε	(Zhao 2000)

Note: σ_{1d} and σ_{ud} are the dynamic triaxial compressive strength and the dynamic uniaxial compressive strength respectively; c_d is the dynamic cohesion; φ is the internal friction angle of intact rock; m is the Hoek-Brown constant for rock material.

Based on experimental results, several semi-empirical equations were proposed to estimate the dynamic strength of rock and concrete materials at different strain rates (Grady and Lipkin 1980; Masuda et al. 1987; Olsson 1991; Malvar et al. 1998; Zhao et al. 1999), as listed in Table 4.1. For dynamic failure criteria, Zhao (2000) attempted to incorporate the

rock dynamic strength in classical criteria such as the Mohr-Coulomb (MC) and Hoek-Brown (HB) strength criteria to capture failure strength of rocks under high strain rate, as listed in Table 4.2.

In addition to experimental results mentioned above, many numerical models (Kim and Chao 2007; Zhou and Hao 2008; Hao and Hao 2013; Zhang and Wong 2013; Wu and Wong 2014; Wu et al. 2015) were published for the investigation of the effect of strain rate on the mechanical behaviours of rock material, which include intact rocks (Olsson 1991) and jointed rock masses (Lankford 1981; Masuda et al. 1987; Zhao et al. 1999). Jacson et al. (2008) found that the energy used in bringing the specimen to fracture increases and the degree of fragmentation increases with increasing strain rate using bonded particle model (BPM) model. The simulation results obtained by Wu and Wong (2014) revealed that the dynamic strength of granite becomes more strain rate dependent when the specimen contains more micro-cracks. Zhang and Wong (2013) demonstrated that the dynamic compressive stress and coalescence stress significant increase, while the crack initiation stress slightly increases with the increasing strain rate for a rock specimen with a non-persistent joint. In their further study using BPM model, Zhang et al. (2017) indicated that numbers of shear and tensile cracks, together with the acoustic emissions increase with increasing strain rate. However, these BPM models mainly focus on the fragmentation characteristic and cracking process, not on the dynamic strengths at different strain rate for both intact and jointed rocks.

The study on the dynamic failure behaviours of jointed rock masses is still very limited. As mentioned above, this is, in fact, an important subject in engineering applications where both the intact rock and the surrounding discontinuities must be considered simultaneously in order to have a more realistic assessment of the dynamic behaviours of rock excavations

such as rock burst susceptibility. In this work, we attempt to address this gap using the simplest rock mass model: a rock specimen containing a single persistent discontinuity oriented at different angles relative to the principal stress direction. The understanding of such a simple model can be used to help analyse the dynamic behaviours of more complex rock mass models. Discrete element method is used in this research to build the numerical models to assess the dynamic behaviours of the jointed rock specimen under dynamic loading condition. Based on the simulation results, a rate dependent failure criterion is proposed which can be used to estimate the failure strength of a jointed rock mass at different strain rates.

2 Simulation methodology: bonded particle model (BPM)

Bonded particle model (BPM) is used in this research for numerical simulations. The theory of BPM is briefly introduced first followed by a demonstration of the capability of BPM in modelling rate-dependent mechanical properties of rock materials through a comparison study between numerical simulations and experimental results. To the best of our knowledge, this is also the first research attempt to use a BPM approach to establish the relationship between the dynamic strength of intact rocks and the strain rate.

2.1 Bonded particle model (BPM)

The BPM (Potyondy and Cundall 2004) was introduced to simulate the mechanical behaviours of an assembly of particles that are bonded together and interact with each other through their contacts when subjected to external loads. The movement of these particles follows Newton's law of motion, while the interaction between particles is determined by constitutive models implemented at their contacts. The motion of particles includes two components: translational motion and rotational motion. Contact force and moment arise when two particles come into contact. Damage process is simulated by the formation of

microscopic shear cracks and tensile cracks when the corresponding shear and tensile stress exceed respectively the shear and tensile strength of the bond connecting the particles. BPM can be used to model both the mechanical behaviours of intact rocks and rocks with discontinuities.

2.1.1 Modelling intact rock

The flat jointed model (FJM) developed by Potyondy and Cundall (2004) has been demonstrated to be capable of reproducing realistically rock mechanical properties. A set of micro-parameters of FJM must be determined first before the simulation model can be established. These parameters are derived using a calibration process that can match the target macro-mechanical properties of the intact rock. The calibration procedure proposed by our previous study (Zhou et al. 2018) is:

a. The Poisson's ratio is matched first by changing the micro-parameter of stiffness ratio k^* in uniaxial compression numerical tests.
b. With the determined Poisson's ratio, Young's modulus is then matched by changing the micro-parameter of effective modules.
c. Finally, the UCS is matched by changing two micro-parameters: bond cohesion and internal friction angle of the bond.

In this work, a rectangular model of $54\text{mm} \times 108\text{mm}$ containing randomly packed non-uniform particles with installed bonds. The 2D model is then subjected to uniaxial compressive loading and direct tension tests to derive the micro-parameters for the FJM corresponding to the type of rock studied. For this study, Hawkesbury sandstone (Wasantha et al. 2013) is the subject rock with its mechanical properties listed in Table 4.3. The micro-parameters of the FJM derived from the calibration process that can simulate the mechanical behaviours of this rock are listed in Table 4.4 and the corresponding modelled macro-

mechanical properties are listed in Table 4.3 together with their variability expressed as coefficient of variation (COV), due to the random nature of the numerical model.

Table 4.3 Mechanical properties of Hawkesbury sandstone (Wasantha et al. 2013): PFC model vs experimental results

Macro-properties	UCS, MPa	Tensile strength, MPa	Young's modulus, GPa	Poisson's ratio
Experimental results	50.80	4.00	11.00	0.20
Numerical results	50.17	4.08	11.02	0.20
COV (%)	0.51	1.40	0.13	0.70

Table 4.4 Basic calibrated micro-parameters for Hawkesbury sandstone

Groups	Micro-parameters	Description	value
Microstructure parameters	w/d	Ratio of specimen width to the average ball diameter	60
	r_{max}/r_{min}	Ratio of maximum to minimum ball radius	1.66
	g/r_{min}	Installation-gap ratio	4e-2
	n_p	Porosity	0.16
	N_r	Number of bond elements	3
FJM Constitutive parameters	E^*(GPa)	Bond modulus	11.40
	k^*	Stiffness ratio	2.5
	μ	Friction coefficient	0.77
	t_b (MPa)	Bond tensile strength	7.10
	c_b (MPa)	Bond cohesion	28.20
	Φ_b (degree)	Bond friction angle	25

2.1.2 Modelling discontinuities

To simulate the mechanical behaviours of discontinuities within a rock mass, a smooth joint contact model (SJM) was proposed and explored in details by Mas Ivars et al. (2008). The SJM simulates the behaviour of a planar interface with dilation regardless of local particle contact orientations along the interface. Two particles on both sides of the smooth joint contact may slide past each other along the joint plane instead of moving around each other following their particle surfaces.

The macro-properties of rock discontinuities include normal stiffness, shear stiffness, cohesion and friction angle. These properties are represented in SJM indirectly using smooth joint micro-parameters such as bond normal stiffness, bond shear stiffness, bond cohesion and friction angle at the particle level. Bahaaddini et al. (2013) proposed a calibration procedure to derive these micro-parameters which include a normal deformability numerical test for normal stiffness and a direct shear numerical test for the shear stiffness, cohesion and friction angle, following the guidelines given in ISRM suggested method (Ulusay 2014).

In this study, normal stiffness and shear stiffness of the discontinuity are not considered so they are set to a large value to minimise their impact on mechanical properties of the discontinuity. The only direct shear numerical test was carried out to match the cohesion and friction angle of the discontinuity. The macro-properties of modelled and experimental results are summarized in Table 4.5. The corresponding micro-parameters are listed in Table 4.6.

Table 4.5 Mechanical properties of the discontinuity (Wasantha et al. 2013)

Parameters	Laboratory tests	Numerical tests
Friction angle (°)	32.00	31.79
Cohesion (MPa)	2.20	2.19

Table 4.6 Calibrated micro-parameters for the smooth-joint model

Calibrated micro-parameters	Normal stiffness (GPa/m)	Shear stiffness (GPa/m)	Friction angle (°)	Cohesion (MPa)	Tensile strength (MPa)
Value	800	200	32	2.20	1

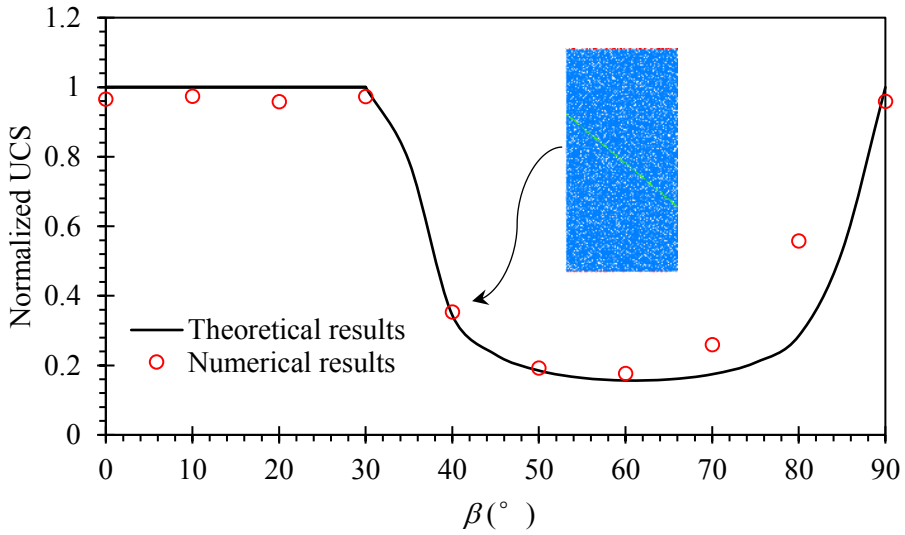

Figure 4.2 Comparison between theoretical (Jaeger 1959) and numerical results for Hawkesbury sandstone with a persistent joint

2.2 Model validation

2.2.1 Jointed rock model with a persistent discontinuity

To demonstrate that BPM+SJM can model the mechanical behaviours of rocks with discontinuities, a BPM with a persistent discontinuity oriented at different angles, shown in Fig. 4.2, subjected to uniaxial compression loading is used to derive the corresponding UCS, normalized by the intact rock UCS, which is considered to be equal to the UCS of the jointed rock when the joint orientation $\beta = 0^{\circ}$ or 90°. The numerical results are then compared with theoretical predictions based on Jaeger's failure criterion (Jaeger 1959):

$$\sigma_1 = \sigma_3 + \frac{2\left(c_j + \sigma_3 tan\phi_j\right)}{sin2\beta\left(1 - tan\phi_j tan\beta\right)} \tag{4.1}$$

where σ_1 and σ_3 are the major and minor principal stresses and for the case of uniaxial loading, σ_3=0; c_j and ϕ_j are joint cohesion and joint friction angle, as shown in Table 4.5 in which β is the joint orientation measured clockwise from the horizontal direction. The

above equation can be rewritten for UCS when normalized by the quasi-static UCS of intact rock as:

$$\sigma_{us(normalized)}^{\beta} = \begin{cases} 1 & \beta < \phi_j \; or \; \beta = 90° \\ \dfrac{2c_j}{\sigma_{us}^{in} sin2\beta\left(1 - tan\phi_j tan\beta\right)} & \phi_j \leq \beta < 90° \end{cases} \quad (4.2)$$

A good agreement between theoretical results and numerical results can be observed with only a small discrepancy at higher β angles (Fig. 4.2). This discrepancy is caused by the boundary effect when the persistent joint intersects both the top and bottom specimen surfaces. In these cases, the failure along the discontinuity is no longer dominant and higher compressive strength is obtained due to the "rupture failure" behaviour associated with the two halves of the specimen separated by the joint (Wasantha et al. 2013).

2.2.2 Dynamic response of intact rock

To demonstrate that BPM can also be used to model the dynamic behaviours of intact rock material, the specimen as shown in Fig. 4.2 is subjected to uniaxial compression loading with various strain rate ranging from 0.001 s^{-1} to 100 s^{-1}. The micro-parameters used for the BPM are as listed in Table 4.4. The normalized UCS ($\sigma_{ud}^{in}/\sigma_{us}^{in}$) , also known as dynamic increase factor (*DIF*), based on simulation results, together with some published experimental data (Green and Perkins 1968; Blanton 1981; Doan and Billi 2011; Kimberley and Ramesh 2011; Zhang and Zhao 2013; Zou et al. 2016) are plotted in Fig. 4.3. Note that to present a unified normalized UCS relationship for different rocks with different strength, it is common to use normalized strain rate (dynamic strain rate/reference strain rate) to define the relationship for normalized UCS ($\sigma_{ud}^{in}/\sigma_{us}^{in}$), where the reference strain rate ε_r is equivalent to the quasi-static strain rate of the rocks (Lankford 1981; Malik et al. 2017). From our simulation results, it was found that the strain rate has very limited effect on UCS

when the strain rate is below 0.1 s^{-1}. This result is consistent with the result of previous studies (Zhang and Wong 2014) where the focus was to find a proper static loading rate for BPM. Therefore, the reference strain rate ε_r in BPM is determined to be 0.1 s^{-1}. Fig. 4.3 shows that the numerical results are consistent with experimental results, suggesting that BPM can capture the dynamic response of rock material. To the best of our knowledge, this is the first research attempt to simulate the rock dynamic behaviours in terms of normalized UCS or *DIF* using the BPM approach. As mentioned above, there are numerous published dynamic BPM studies, but their focus were mainly on rock fragmentation (Whittles et al. 2006) and fracturing process (Zhang and Wong 2013; Feng et al. 2017; Zhang et al. 2017).

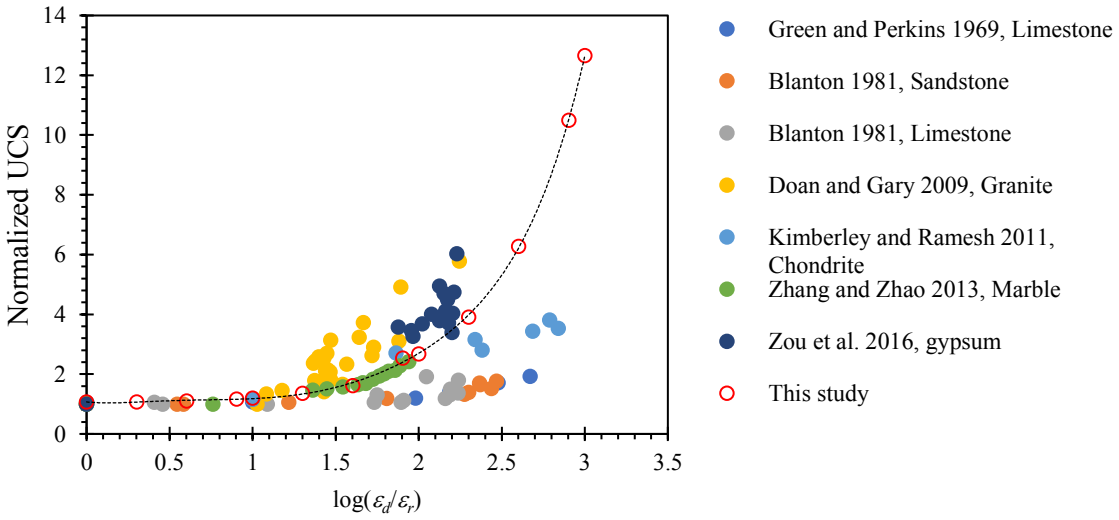

Figure 4.3 Normalised UCS of experimental and numerical results

3 The proposed dynamic strength model

Using the semi-empirical strength relationship mentioned in Section 1 (Green and Perkins 1968; Olsson 1991), the dynamic uniaxial compressive strength can be related to normalized strain rate and static uniaxial compressive strength for intact rock, i.e.:

$$\sigma_{ud} \propto \left(\frac{\varepsilon_d}{\varepsilon_r}, \sigma_{us}\right) \tag{4.3}$$

An exponential expression is commonly used in the literature to describe the relationship between the dynamic UCS of rock materials and the normalized strain rate, as listed in Table 4.1. Therefore, in this study, a similar form of expression is also used to describe the dynamic strength of intact rock:

$$\sigma_{ud(normalized)}^{in} = A_{in}\left(\frac{\varepsilon_d}{\varepsilon_r}\right)^{B_{in}} + C_{in} \tag{4.4}$$

where $\sigma_{ud(normalized)}^{in}$ is the normalized (by static UCS) dynamic strength for intact rock, and the A_{in}, B_{in} and C_{in} are coefficients for the intact rock dynamic strength model. Using least square regression of the numerical simulation results presented in the previous section, A_{in}, B_{in} and C_{in} are found to be 0.02, 0.92 and 0.98, respectively. When the dynamic strain rate ε_d approaching to ε_r, σ_{ud}^{in} equals to the static UCS of intact rock and therefore $\sigma_{ud(normalized)}^{in}$ = 1. Eq. (3) represents a unified normalised relationship between intact rock dynamic UCS and the strain rate and is applicable for different rock types (Fig. 4.4).

For a jointed rock mass, the static UCS varies with different joint orientation according to Jaeger's criterion presented in Equation (4.1). For dynamic loading cases, assuming the dynamic failure strength of a jointed rock mass also follows Jaeger's relationship, i.e.:

$$\frac{\sigma_{ud}^{\beta}}{\sigma_{ud}^{in}} = \frac{\sigma_{us}^{\beta}}{\sigma_{us}^{in}} \tag{4.5}$$

Then the dynamic UCS for a rock specimen with a persistent joint, normalised by the static UCS of intact rock, can be expressed:

$$\sigma_{ud(normalized)}^{\beta} = \frac{\sigma_{ud}^{\beta}}{\sigma_{us}^{in}} = \frac{\sigma_{ud}^{\beta}}{\sigma_{ud}^{in}}\frac{\sigma_{ud}^{in}}{\sigma_{us}^{in}} \tag{4.6}$$

Therefore, combining the above equations with Eq. (4.1):

$$\sigma_{ud(normalized)}^{\beta}=\begin{cases}\sigma_{ud(normalized)}^{in}, & \beta<\phi_j \; or \; \beta=90° \\ \dfrac{2c_j}{\sigma_{us}^{in}sin2\beta\left(1-tan\phi_j tan\beta\right)}\sigma_{ud(normalized)}^{in}, & \phi_j\le\beta<90°\end{cases} \tag{4.7}$$

From Eq. (3), the normalized dynamic strength model can then be written as:

$$\sigma_{ud(normalized)}^{\beta}=\begin{cases}A_{in}\left(\dfrac{\varepsilon_d}{\varepsilon_r}\right)^{B_{in}}+C_{in}, & \beta<\phi_j \; or \; \beta=90° \\ \dfrac{2c_j}{\sigma_{us}^{in}sin2\beta\left(1-tan\phi_j tan\beta\right)}\left[A_{in}\left(\dfrac{\varepsilon_d}{\varepsilon_r}\right)^{B_{in}}+C_{in}\right], & \phi_j\le\beta<90°\end{cases} \tag{4.8}$$

If the form of exponential expression is also used to describe the dynamic UCS of rock with a persistent joint at different orientations:

$$\sigma_{ud(normalized)}^{\beta}=A\left(\frac{\varepsilon_d}{\varepsilon_r}\right)^{B}+C \tag{4.9}$$

then the coefficients *A*, *B* and C are identical to A_{in}, B_{in} and C_{in} when $\beta<\phi_j \; or \; \beta=90°$; and when $\phi_j\le\beta<90°$, these coefficients are:

$$A=A_{in}\frac{2c_j}{\sigma_{us}^{in}\,sin2\beta\left(1-tan\phi_j tan\beta\right)} \tag{4.10}$$

$$B=B_{in} \tag{4.11}$$

$$C=C_{in}\frac{2c_j}{\sigma_{us}^{in}\,sin2\beta\left(1-tan\phi_j tan\beta\right)} \tag{4.12}$$

4 Numerical simulations of the dynamic UCS of a jointed rock mass

To investigate the effect of strain rate on the dynamic UCS of a rock with a persistent joint, a series of numerical specimens with different joint orientation are constructed and they are then subjected to uniaxial compressions at different loading rates to derive the corresponding dynamic UCS. The proposed dynamic failure model described above is then cross-validated by the simulation results.

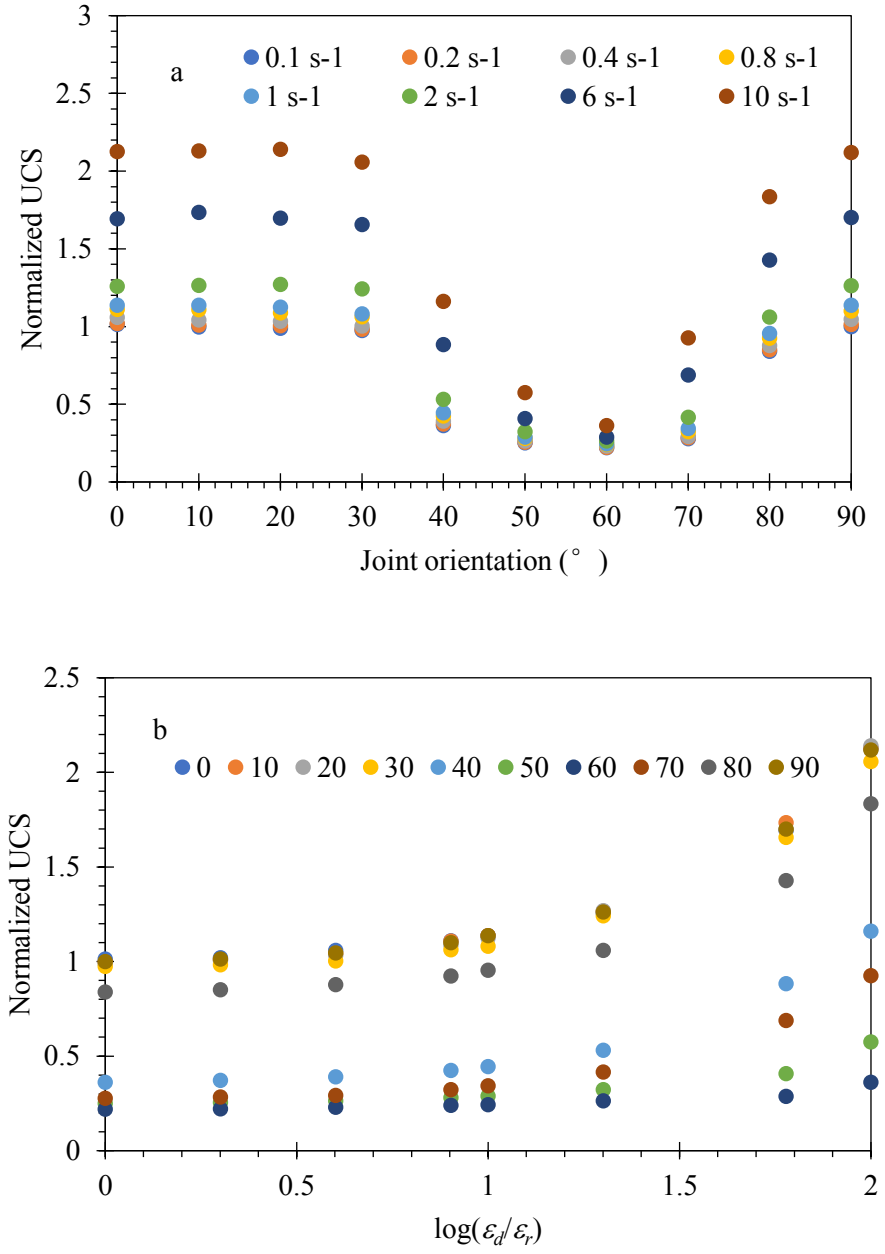

Figure 4.4 UCS of the specimen with different joint orientations at different strain rates

4.1 BPM simulation results

Fig. 4.4 shows the dynamic UCS of the jointed rock at different joint orientation, normalised by the static UCS of the specimen. The relationships between the dynamic UCS of the rock at different joint orientation and the normalised strain rates are shown in Fig. 4.4 (b).

As expected, the dynamic strength increases with increasing strain rate. When $\beta < \phi_j$ or $\beta = 90°$, the normalized UCS increases from 1.0 to approximately 2.1 as the strain rate increases from 0.1 s^{-1} to 10 s^{-1}. When $\phi_j < \beta < 90°$, the dynamic strength also increases with increasing strain rate. However, the rate of increment is sensitive to the joint orientation, with the least happening at around $\beta = 60°$, where the normalized UCS only increases from 0.22 to 0.36 as strain rate increases from 0.1 s^{-1} to 10 s^{-1}. As sliding failure is the dominant failure mechanism when β is around $45° + \frac{\phi_j}{2}$, the results suggest that shear failure may be less sensitive to changes in strain rates. It will be interesting that this can be cross-validated by experiments.

Table 4.7 *A*, *B* and *C* obtained based on least square regression of simulation results

Joint orientation (˚)	*A*	*B*	*C*	R^2
0	1.65E-02	0.92	0.99	0.99
10	2.50E-02	0.83	0.97	0.99
20	2.04E-02	0.88	0.97	0.99
30	2.10E-02	0.87	0.94	0.99
40	1.39E-02	0.89	0.34	0.99
50	1.40E-03	1.17	0.26	0.98
60	1.75E-03	0.94	0.22	0.96
70	1.03E-02	0.91	0.26	0.99
80	1.28E-02	0.94	0.83	0.99
90	2.04E-02	0.87	0.98	0.99

4.2 Assessment of the proposed dynamic strength model

To assess the dynamic strength model presented in Section 3, the simulation results in Section 4.1 is used to derive coefficients and further compared with the theoretical

prediction of Eq. (9). The coefficients A, B and C are derived based on the least squares regression of the numerical simulation results discussed in the previous section and their values are summarized in Table 4.7 together with the goodness-of-fit indicator R^2.

These coefficients are plotted in Fig. 4.5, together with their theoretical predations based on the proposed dynamic strength model. The results show that theoretical predictions are in reasonably good agreement with the simulation results. The discrepancies are caused by the random nature of the discrete element modelling approach. For large β angles, the differences become significant, which is caused by the change of failure mechanism due to the intersection between the persistent joint and the top and bottom surfaces of the specimen.

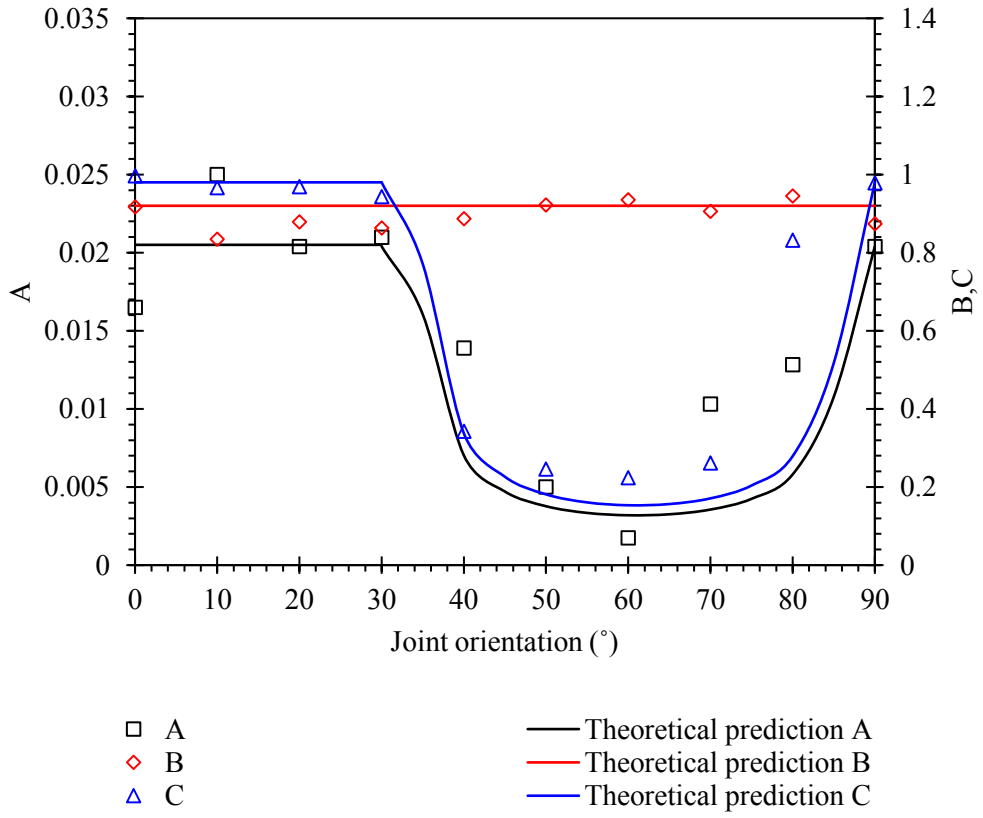

Figure 4.5 The comparison of parameters A, B and C with corresponding theoretical predictions based on the proposed model

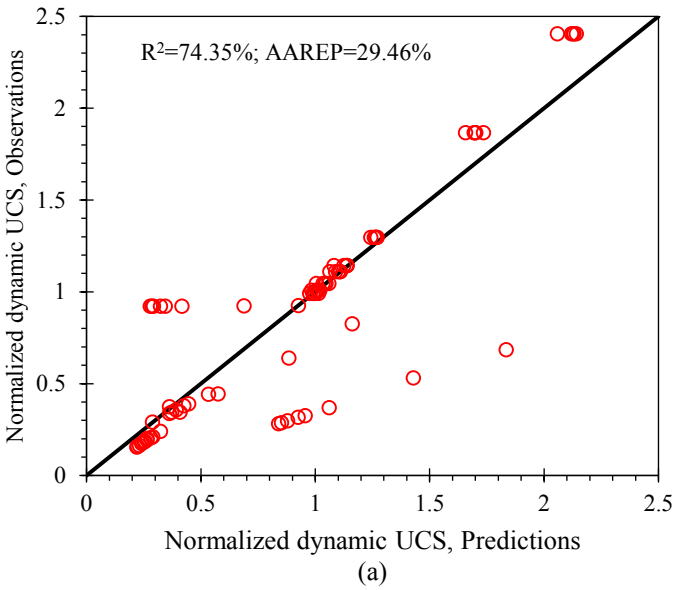

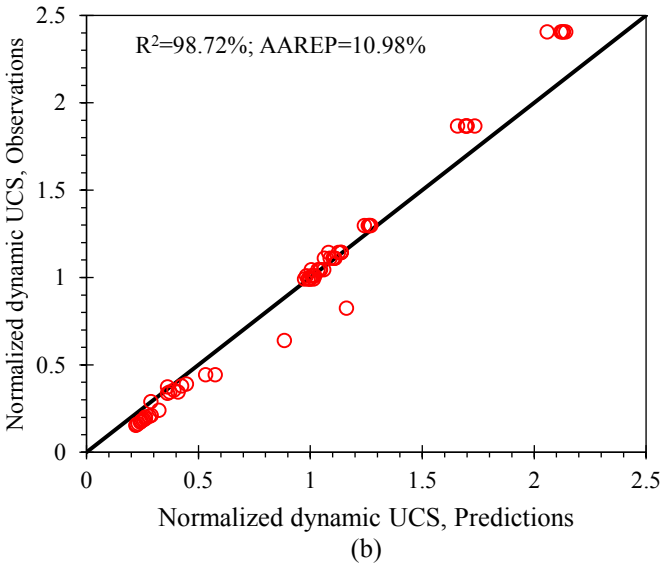

Figure 4.6 The comparison of dynamic normalized UCS from theoretical predictions and simulation results, (a) all data; (b) excluding the data when $60° < \beta < 90°$

To further evaluate the reliability and robustness of the proposed dynamic strength model, the predicted normalized dynamic UCS of the jointed rock is compared with simulation results presented in Section 4.1. In the validation process, the regression R-squared value

(R^2) and the average absolute relative percentage error (AAREP) are used as a measurement of discrepancy for the assessment (Shen et al. 2012):

$$\text{AAREP} = \frac{\sum_{i=1}^{N} \left| \frac{M_{R,i}^{pre} - M_{R,i}^{obs}}{M_{R,i}^{obs}} \right|}{N} \tag{4.12}$$

where N is the total number of numerical simulations, $M_{R,i}^{obs}$ and $M_{R,i}^{pred}$ are simulation results and theoretical predications, respectively, $M_{R,i}^{av}$ is the average of simulation values.

The comparison of all cases between theoretical predictions and simulation results is shown in Fig. 4.6 (a) where relatively larger differences are observed with the values of R^2 and AAREP at 74.35% and 29.46%, respectively. Closer observations indicate that major discrepancies correspond to those cases at large β angles where the persistent joint intersects the top and bottom surfaces of the specimen. As the proposed dynamic strength model is essentially derived based on Jaeger's strength criterion, which assumes that the failure mechanism is the shear failure along the persistent joint. When the joint intersects the top and bottom surfaces of the specimen, the assumed shear failure mechanism is no longer dominant (see more discussions below), which will cause the deviation of predicted values from the actual strength of the specimen. This is observed clearly in both experiments (Bagheripour and Mostyn 1996; Wasantha et al. 2013) and numerical studies (Fig. 4.2, (Wasantha et al. 2012; Chong et al. 2013)). If these cases (corresponding to $60° < \beta < 90°$ in our numerical models) are removed from Fig. 4.6 (a), the agreement between the proposed model and the simulation results is much improved, with R^2 greater than 0.98 and AAREP less than 11%, as shown in Fig. 4.6 (b). This demonstrates that the proposed model can describe properly the dynamic strength of a specimen with a persistent joint under the

assumption that the dominant failure mechanism is the shear failure along the joint, similar to the Jaeger's criterion to describe the static strength of such a specimen.

5 Discussions

The simulation results clearly show that the effect of the strain rate on the dynamic strength of the jointed rock mass is significant. To better understand the dynamic failure behaviours of the jointed rock mass, the fragmentation characteristics, microscopic cracks and crack orientation distribution are further analysed in this section from the micromechanical perspective based on the numerical simulations.

5.1 The fragmentation characteristics

5.1.1 The fragmentation characteristics of intact rock

The fragmentation characteristics of intact rock under different loading rates are studied by increasing the strain rate from 0.1 s^{-1} to 10 s^{-1}. Fragmentations derived from numerical models are presented in Fig. 4.7 in comparison with experimental results from Whittles et al. (2006). These results are also consistent with the observation made by many researchers (Li et al. 2005; Doan and Gary 2009) based on their experiment: fractures changes from single fracturing to multiple fragmentations and even to pulverization as the strain rate increases, i.e., the size of fragments becomes smaller but their number gets larger. This trend is also reflected by the number of microscopic fractures formed at different strain rates in the numerical models, see Fig. 4.8.

These failure characteristics may be related to the time-dependent initiation and propagation of micro-cracks in rocks (Costin 1987; Li and Xia 2000; Fuenkajorn et al. 2012; Zhou et al. 2015). At the strain rate increases, the dynamic strength increases and therefore a higher level of stress is reached before micro-cracks coalescence occurs, causing the

specimen to fail. Consequently, a greater number of micro-cracks are generated in the specimen fracturing process.

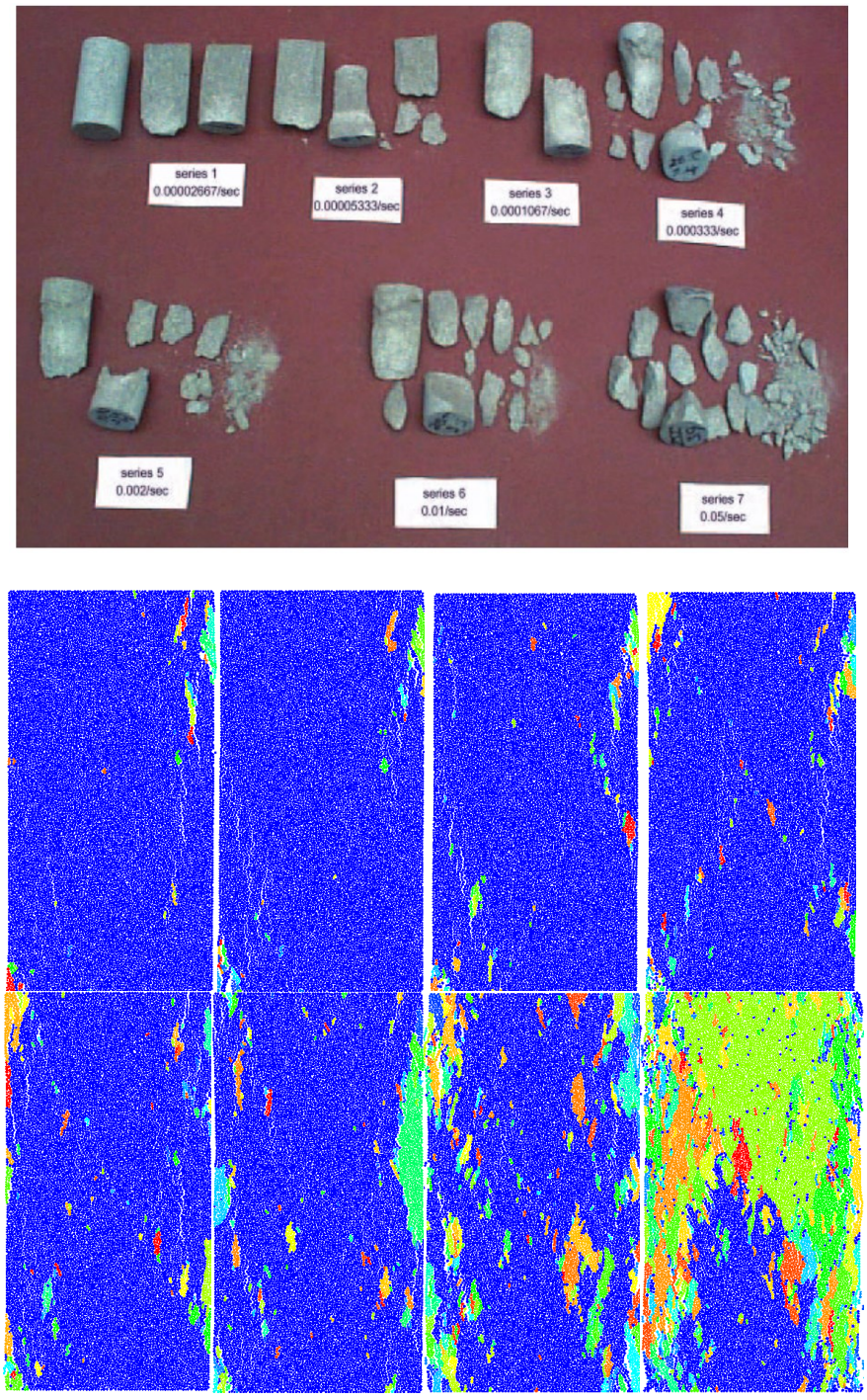

Figure 4.7 Comparison of post failure fragmentation under different loading rate (0.1 s^{-1}, 0.2 s^{-1}, 0.4 s^{-1}, 0.8 s^{-1}, 1 s^{-1}, 2 s^{-1}, 6 s^{-1} and 10 s^{-1}) between experimental study (Whittles et al. 2006; Jacson et al. 2008) and BPM simulations

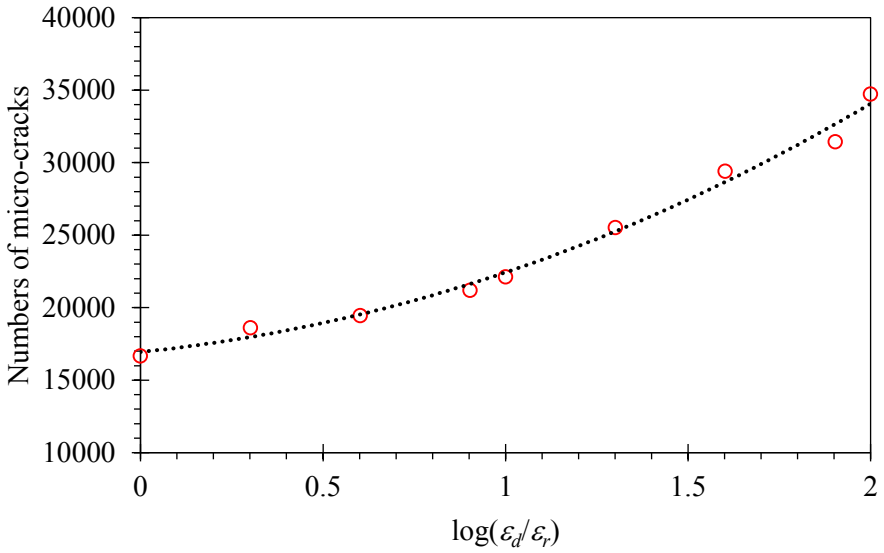

Figure 4.8 Number of micro-cracks in BPM at different strain rates

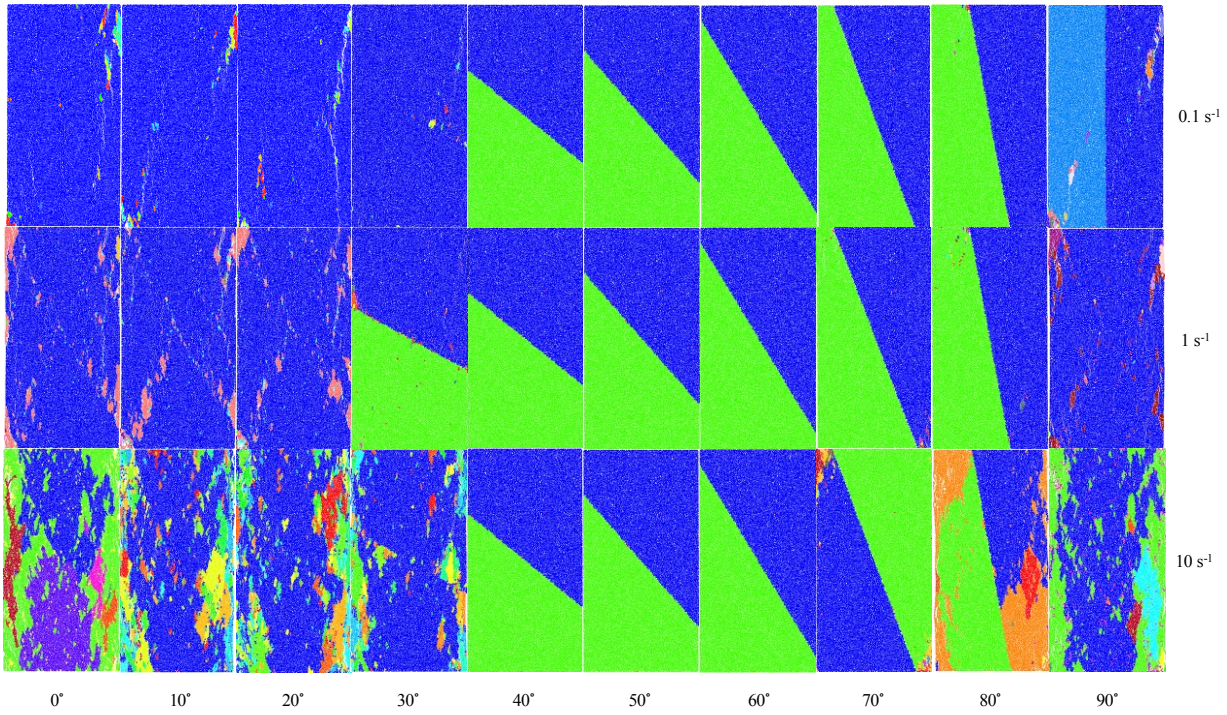

Figure 4.9 Fragment characteristics of jointed rock mass under various strain rate (0.1 s^{-1}, 1 s^{-1} and 10 s^{-1}). Note that particles with the same colour are in the same fragment

5.1.2 The fragmentation characteristics of jointed rock masses

For jointed rock masses, based on our numerical simulations, as shown in Fig. 4.9, the fragmentation characteristics are similar to those of intact rock only when $\beta < \phi_j$ or $\beta = 90°$. As expected, when $\phi_j < \beta < 90°$, the fragmentation characteristics are totally different compared with those of intact rock due to the present of the joint. The sliding failure can be easily seen from two distinct blocks of different movements. At high β angles when the joint intersects both the top and bottom surfaces of the specimen, the failure mode is a mixture of sliding along the joint, shearing and tensile failure within the two halves of intact rock, so both ends of the specimen appear "crushed". It can also be observed from Fig. 4.9 that shearing and tensile failures intensify as the strain rate increases.

The number of micro-cracks based on the numerical simulations of jointed rock mass is shown in Fig. 4.10. In general, the number of micro-cracks increases with increasing strain rate for all cases. The results for the cases of $\beta < \phi_j$ *or* $\beta = 90°$ follow closely that of intact rock, suggesting similar dominant shearing failure mode in these cases. When $\phi_j < \beta < 60°$, the number of micro-cracks is significantly smaller compared with the cases mentioned above, particularly for cases of $\beta = 40^o - 70^o$. This suggest that the sliding failure along the joint becomes dominant in these cases and the internal stress experienced by parts of intact rock of the specimen is not high enough to cause shearing and tensile failures. However, even in these cases, the strain rate will also have effects on the failure mode. As the rate increases, more micro-cracks are formed, indicating the occurrence of more shearing and tensile failures, a consequence of the combination of the high impact load and the dynamic dissipation of the energy within the part of intact rock of the specimen.

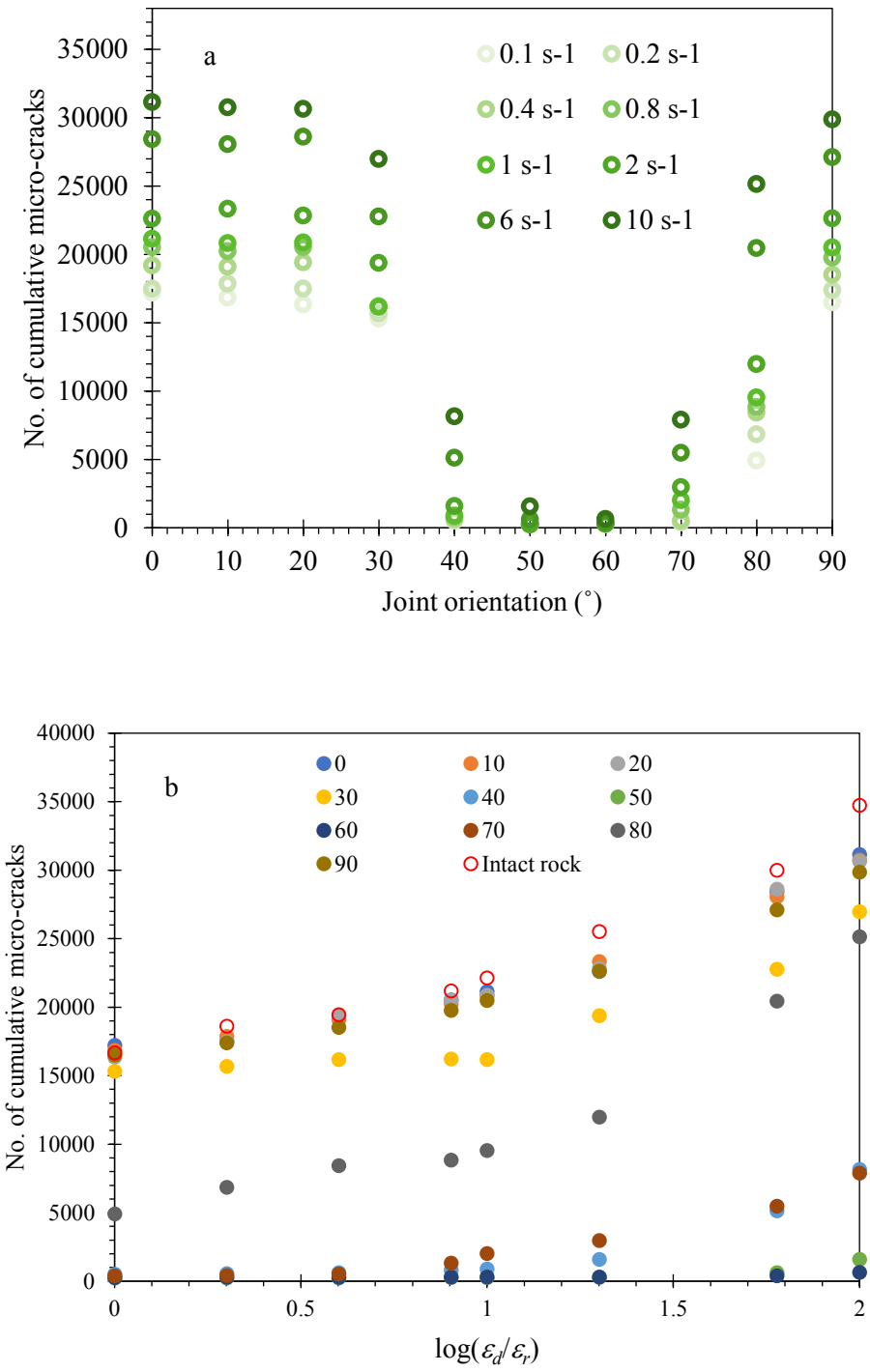

Figure 4.10 Number of microscopic cracks of numerical models at different joint orientations and strain rates

5.2 Orientations of microscopic cracks

When the BPM specimen is subject to compression loading, the macroscopic failure involves microscopic crack initiation, propagation and coalescence. Early studies (Nemat-Nasser and Horii 1982; Basista and Gross 1998) often used the sliding-crack model to capture the formation of micro-tensile cracks (Fig. 4.11a). In BPM models, a force-chain crack model can be used to illustrate the compression-induced tensile cracking process (Potyondy and Cundall 2004; Hoek and Martin 2014), see Fig. 11b. Therefore, the microscopic cracks can be analysed in PFC.

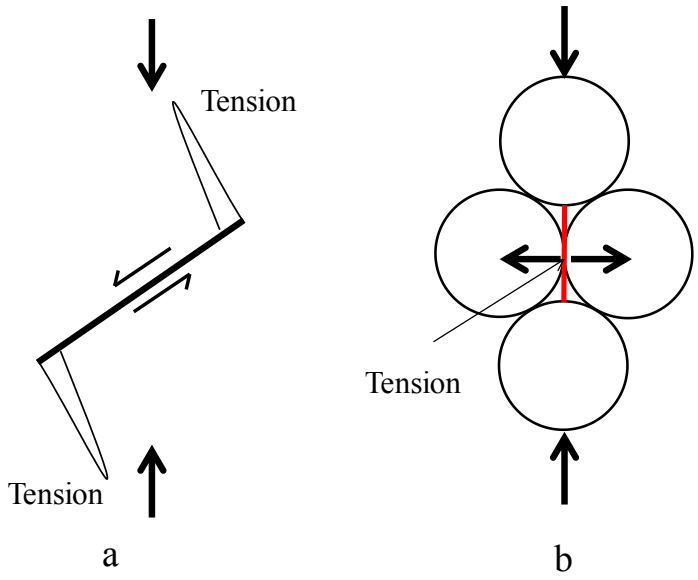

Figure 4.11 Physical mechanisms for compression-induced tensile cracking, idealized using a bonded assembly of particles (after Hoek and Martin, 2014)

To better understand the failure mechanism, the orientations of microscopic cracks are discussed in this section. These include tensile cracks (Fig. 4.12) where the bond breaks in tensile mode and shearing cracks (Fig. 4.13) where the bond undergoes a shear failure. Note that the orientation of cracks, in this case, is defined as the angle of crack to the horizontal

plane measured anticlockwise. Only cases of β = 0°, 50° and 80° are shown here to demonstrate three different cases of failure mode mixture.

When a rock specimen is subjected to an external load, the macroscopic failure is the consequence of the initiation, propagation and coalescence of micro-cracks. In reality, these micro-cracks could be transgranular or intergranular depending on local stress conditions, or rock grains can be "crushed" under extremely high compressive load, which can be regarded as the collective action of many transgranular cracks. In BPM, micro-cracks can only happen in two ways: tensile and shearing breakage of the bond interface. The force-chain crack model was proposed to illustrate the compression-induced tensile cracking process (Potyondy and Cundall 2004; Hoek and Martin 2014). This is demonstrated by a group of four circular particles arranged in a diamond shape and the left and right particles are forced apart (hence subjected to potential tensile failure) by an axial load applied at the top and bottom particles. Therefore, the orientations of these microscopic cracks are parallel to the applied stress direction.

From Fig. 4.12, these tensile micro cracks are dominant in all cases, particularly for small and large β angles. For β = 50° where sliding failure is the dominant macroscopic failure mode, tensile cracks parallel to the axial loading direction is still dominant. But in this case, some additional tensile cracks perpendicular to the joint also appear, particularly for the case of low strain rate. This is likely due to the friction force on the surface of the joint causing some bonds near the surface to undergo tensile breakage.

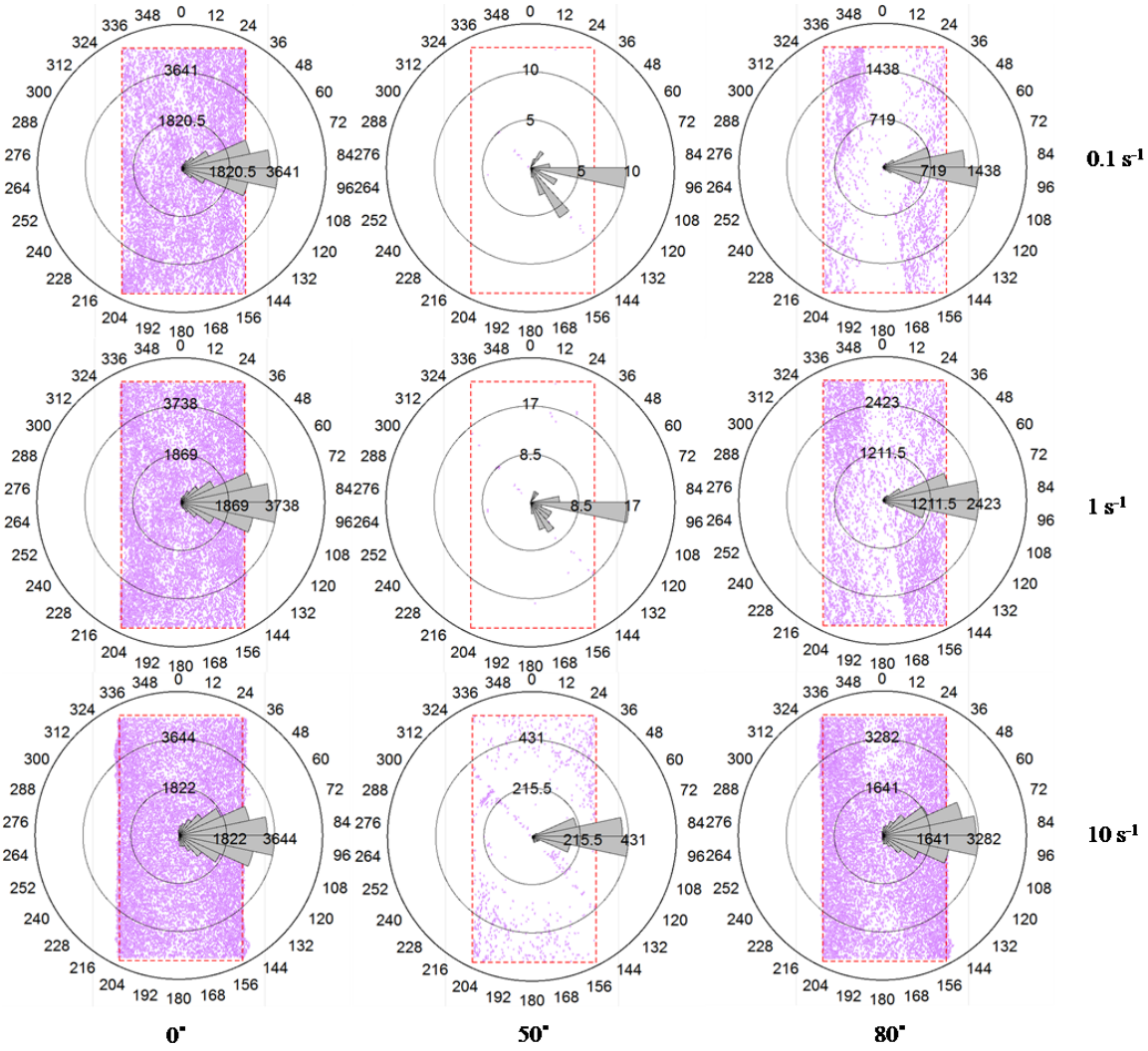

Figure 4.12 Distribution of the orientation of tensile microscopic cracks of the numerical models

For shearing micro-cracks (Fig. 4.13), when $\beta = 0°$, their orientations are mainly in the ranges of 36˚-60˚ and 120˚-144˚, indicating a "X" shearing failure behaviour, which is consistent to experimental observations. This "X" shearing feature is less obvious as the failure mode becomes complex ($\beta = 80^o$) or disappears all together when the macroscopic sliding failure along the joint becomes dominant ($\beta = 50^o$). Some shear cracks in vertical orientation are observed when $\beta = 50^o$, which again may be caused by the friction on the

joint surface due to its roughness. For $\beta = 80^{o}$, close to the case of β=90^{o}, the "X" shearing feature becomes more obvious as strain rate increases from 0.1 s^{-1} to 10 s^{-1}.

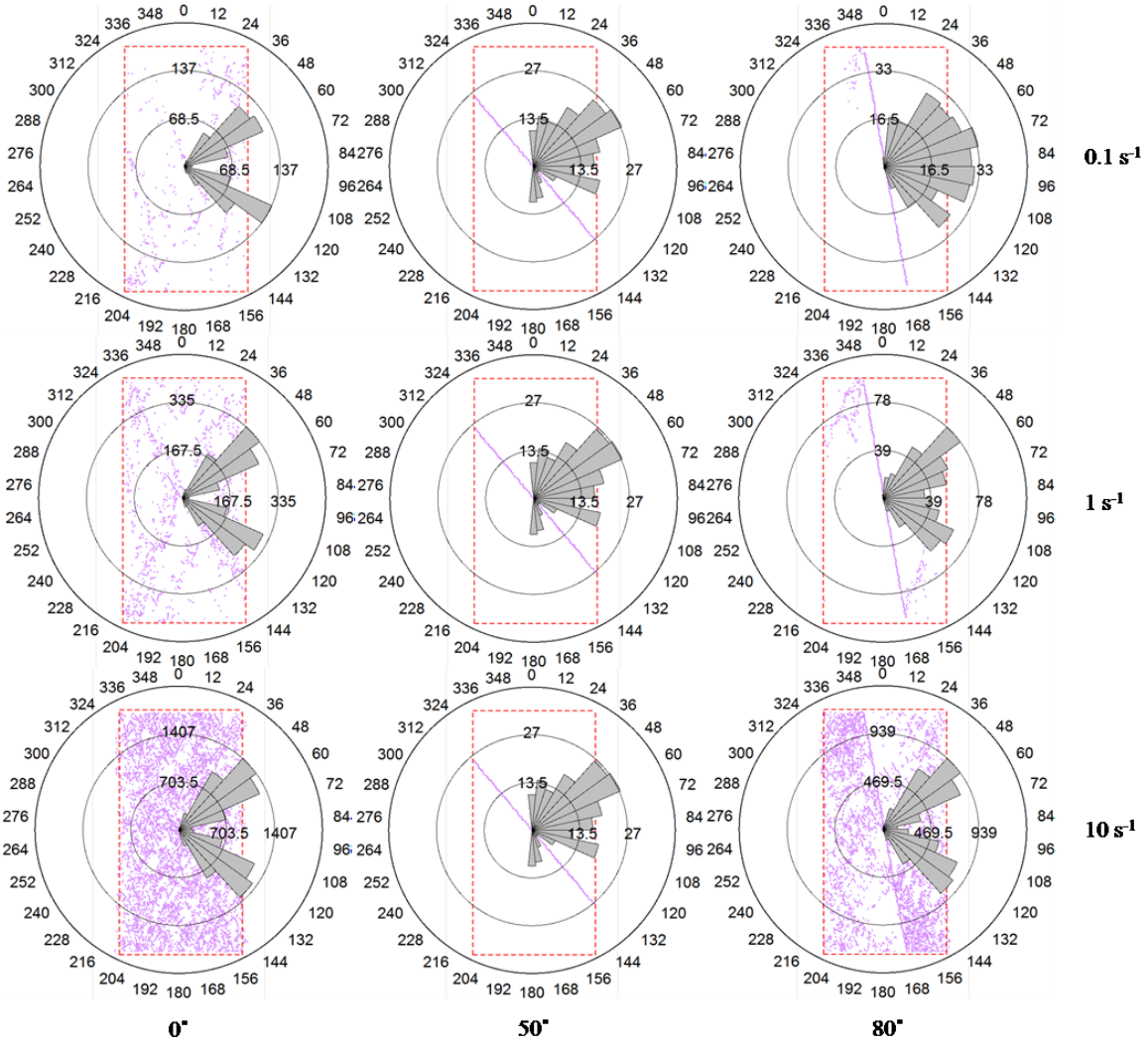

Figure 4.13 Distribution of shearing microscopic cracks of the numerical models

6 Conclusions

The rock dynamic behaviours in terms of uniaxial compressive strength are investigated in this study using bonded particle models. The following conclusions can be drawn based on the works presented:

1. BPM has been demonstrated to be capable of simulating the strain rate-dependent mechanical properties and behaviours of rock materials. These can include uniaxial compressive strength, fragmentation characteristic and the features of micro-cracking within the rock specimen. This is the first time that a BPM approach is used systematically for these studies.
2. A dynamic failure criterion is proposed for the rock mass with a persistent joint based on the single plane of weakness theory. The model has been demonstrated to be effective for the prediction of the dynamic UCS of a rock mass with a joint at different orientations.
3. The dynamic behaviours of a rock mass are more sensitivity to the strain rate when tensile and shearing failure modes within the parts of intact rock are more dominant, corresponding to joints at low and high angles. When the macroscopic sliding failure mode is dominant, corresponding to cases where joint orientation is close to $45° + \phi_j/2$, the dynamic behaviours of the jointed rock mass is much less sensitive to the variations of strain rates.

Acknowledgement

The PhD scholarship provided by the China Scholarship Council (CSC) to the first author is gratefully acknowledged.

References

Bagheripour MH, Mostyn G (1996) Prediction of the strength of jointed rock - Theory and practice. In: ISRM International Symposium-EUROCK 96. International Society for Rock Mechanics and rock engineering. Torino, Italy; p. 231-8.

Bahaaddini M, Sharrock G, Hebblewhite BK (2013) Numerical direct shear tests to model the shear behaviour of rock joints. Comput Geotech 51:101–115.

Basista M, Gross D (1998) The sliding crack model revisited. Stud Appl Mech 46:125–143.

Blanton TL (1981) Effect of strain rates from 10-2 to 10 sec-1 in triaxial compression tests on three rocks. Int J Rock Mech Min Sci 18:47–62.

Brace WF, Jones AH (1971) Comparison of uniaxial deformation in shock and static loading of three rocks. J Geophys Res 76:4913–4921.

Cadoni E (2010) Dynamic characterization of orthogneiss rock subjected to intermediate and high strain rates in tension. Rock Mech Rock Eng 43:667–676.

Cai M, Kaiser PK, Suorineni F, Su K (2007) A study on the dynamic behavior of the Meuse/Haute-Marne argillite. Phys Chem Earth 32:907–916.

Chong WL, Haque A, Gamage RP, Shahinuzzaman A (2013) Modelling of intact and jointed mudstone samples under uniaxial and triaxial compression. Arab J Geosci 6:1639–1646.

Costin LS (1987) Time-dependent deformation and failure. Fract Mech rock 167:215.

Doan ML, Billi A (2011) High strain rate damage of Carrara marble. Geophys Res Lett 38:.

Doan ML, Gary G (2009) Rock pulverization at high strain rate near the San Andreas fault. Nat Geosci 2:709–712.

Feng P, Ayatollahi MR, Dai F, Xu NW, Wei MD (2017) DEM investigation on fracture mechanism of the CCNSCB specimen under intermediate dynamic loading. Arab J Geosci 10:48.

Fuenkajorn K, Sriapai T, Samsri P (2012) Effects of loading rate on strength and deformability of Maha Sarakham salt. Eng Geol 135–136:10–23.

Grady DE, Lipkin J (1980) Criteria for impulsive rock fracture. Geophys Res Lett 7:255–258.

Green SJ, Perkins RD (1968) Uniaxial compression tests at varying strain rates on three geologic materials. In: The 10th US Symposium on Rock Mechanics (USRMS). American Rock Mechanics Association, pp 35–54.

Hao Y, Hao H (2013) Numerical investigation of the dynamic compressive behaviour of rock materials at high strain rate. Rock Mech Rock Eng 46:373–388.

Hoek E, Martin CD (2014) Fracture initiation and propagation in intact rock - A review. J Rock Mech Geotech Eng 6:287–300.

Jackson K, Kingman SW, Whittles DN, Lowndes IS, Reddish DJ (2008) The effect of strain rate on the breakage behavior of rock. Arch Min Sci 53:3–22.

Jaeger JC (1959) The frictional properties of joints in rock. Pure Appl Geophys 43:148–158.

Kim Y, Chao YJ (2007) Effect of loading rate on dynamic fracture initiation toughness of brittle materials. Int J Fract 145:195–204.

Kimberley J, Ramesh KT (2011) The dynamic strength of an ordinary chondrite. Meteorit Planet Sci 46:1653–1669.

Lankford J (1981) The role of tensile microfracture in the strain rate dependence of compressive strenght of fine-grained limestone-analogy with strong ceramics. Int J Rock Mech Min Sci 18:173–175.

Li HB, Zhao J, Li JR, Liu YQ, Zhou QC (2004) Experimental studies on the strength of different rock types under dynamic compression. Int J Rock Mech Min Sci 41:68–73.

Li XB, Lok TS, Zhao J (2005) Dynamic characteristics of granite subjected to intermediate loading rate. Rock Mech Rock Eng 38:21–39.

Li Y, Xia C (2000) Time-dependent tests on intact rocks in uniaxial compression. Int J Rock Mech Min Sci 37:467–475.

Liu S, Xu J (2015) Effect of strain rate on the dynamic compressive mechanical behaviors of rock material subjected to high temperatures. Mech Mater 82:28–38.

Malik A, Chakraborty T, Rao KS (2017) Strain rate effect on the mechanical behavior of basalt: Observations from static and dynamic tests. Thin-Walled Struct 126:127–137.

Malvar LJ, Crawford JE (1998) Dynamic Increase Factors. 28th DDESB Semin Orlando 1–17.

Mas Ivars D, Potyondy D, Pierce M, Cundall P (2008) The smooth-joint contact model. In: Proceedings of WCCM8-ECCOMAS, 2008, 8th. Venice, Italy.

Masuda K, Mizutani H, Yamada I (1987) Experimental study of strain-rate dependence and pressure dependence of failure properties of granite. J Phys Earth 35:37–66.

Nemat-Nasser S, Horii H (1982) Compression-induced nonplanar crack extension with application to splitting, exfoliation, and rockburst. J Geophys Res 87:6805.

Olsson WA (1991) The compressive strength of tuff as a function of strain rate from 10-6

to 103/sec. Int J Rock Mech Min Sci 28:115–118.

Potyondy DO, Cundall PA (2004) A bonded-particle model for rock. Int J Rock Mech Min Sci 41:1329–1364.

Shen J, Karakus M, Xu C (2012) Direct expressions for linearization of shear strength envelopes given by the Generalized Hoek-Brown criterion using genetic programming. Comput Geotech 44:139–146.

Ulusay R (ed) (2014) The ISRM suggested methods for rock characterization, testing and monitoring: 2007-2014. Springer.

Wasantha PL, Ranjith PG, Viete DR (2013) Specimen slenderness and the influence of joint orientation on the uniaxial compressive strength of singly jointed rock. J Mater Civ Eng 26:2–5.

Wasantha PLP, Ranjith PG, Viete DR (2012) Specimen slenderness and the influence of joint orientation on the uniaxial compressive strength of jointed rock: A numerical study. In: ISRM Regional Symposium-7th Asian Rock Mechanics Symposium. international Society for Rock Mechanics, pp 174–180.

Wasantha PL, Ranjith PG, Zhao J, Shao SS, Permata G (2015) Strain rate effect on the mechanical behaviour of sandstones with different grain sizes. Rock Mech Rock Eng 48:1883–1895.

Whittles DN, Kingman S, Lowndes I, Jackson K (2006) Laboratory and numerical investigation into the characteristics of rock fragmentation. Miner Eng 19:1418–1429.

Wu Z, Liang X, Liu Q (2015) Numerical investigation of rock heterogeneity effect on rock dynamic strength and failure process using cohesive fracture model. Eng Geol 197:198–210.

Wu Z, Wong LNY (2014) Investigating the effects of micro-defects on the dynamic properties of rock using Numerical Manifold method. Constr Build Mater 72:72–82.

Zhang QB, Zhao J (2014) A review of dynamic experimental techniques and mechanical behaviour of rock materials. Rock Mech Rock Eng 47:1411–1478.

Zhang QB, Zhao J (2013) Determination of mechanical properties and full-field strain measurements of rock material under dynamic loads. Int J Rock Mech Min Sci 60:423–439.

Zhang X, Zhang Q, Wu S (2017) Acoustic emission characteristics of the rock-like material containing a single flaw under different compressive loading rates. Comput Geotech 83:83–97.

Zhang XP, Wong LNY (2013) Loading rate effects on cracking behavior of flaw-contained specimens under uniaxial compression. Int J Fract 180:93–110.

Zhang XP, Wong LNY (2014) Choosing a proper loading rate for bonded-particle model of intact rock. Int J Fract 189:163–179.

Zhao J (2000) Applicability of Mohr-Coulomb and Hoek-Brown strength criteria to the dynamic strength of brittle rock. Int J Rock Mech Min Sci 37:1115–1121.

Zhao J, Li H., Wu M., Li T. (1999) Dynamic uniaxial compression tests on a granite. Int J Rock Mech Min Sci 36:273–277.

Zhou C, Xu C, Karakus M, Shen J (2018) A systematic approach to the calibration of micro-parameters for the flat-jointed bonded particle model. Geomech Eng 16:471–482.

Zhou H, Yang Y, Zhang C, Hu D (2015) Experimental investigations on loading-rate dependency of compressive and tensile mechanical behaviour of hard rocks. Eur J

Environ Civ Eng 19: s70–s82.

Zhou XQ, Hao H (2008) Modelling of compressive behaviour of concrete-like materials at high strain rate. Int J Solids Struct 45:4648–4661.

Zhu WC, Niu LL, Li SH, Xu ZH (2015) Dynamic Brazilian test of rock under intermediate strain rate: pendulum hammer-driven SHPB test and numerical simulation. Rock Mech Rock Eng 48:1867–1881.

Zou C, Wong LNY, Loo JJ, Gan BS (2016) Different mechanical and cracking behaviors of single-flawed brittle gypsum specimens under dynamic and quasi-static loadings. Eng Geol 201:71–84.

Chapter 5 A new damage model accounting the effect of joint orientation for the jointed rock mass

(Paper 3)

Changtai Zhou[1], Chaoshui Xu[1], Murat Karakus[1], Jiayi Shen[2]

[1]School of Civil, Environmental and Mining Engineering, The University of Adelaide, Adelaide, Australia

[2]Institute of Port, Coastal and Offshore Engineering, Zhejiang University, Hangzhou, China

Statement of Authorship

Title of Paper	A new damage model accounting the effect of joint orientation for the jointed rock mass
Publication Status	☐ Published ☐ Accepted for Publication ☑ Submitted for Publication ☐ Unpublished and Unsubmitted w ork w ritten in manuscript style
Publication Details	Submitted to Engineering Geology and currently under review.

Principal Author

Name of Principal Author (Candidate)	Changtai Zhou		
Contribution to the Paper	Conducted the research and w rote the manuscript.		
Overall percentage (%)	85%		
Certification:	This paper reports on original research I conducted during the period of my Higher Degree by Research candidature and is not subject to any obligations or contractual agreements with a third party that w ould constrain its inclusion in this thesis. I am the primary author of this paper.		
Signature		Date	17/02/2019

Co-Author Contributions

By signing the Statement of Authorship, each author certifies that:

i. the candidate's stated contribution to the publication is accurate (as detailed above);

ii. permission is granted for the candidate in include the publication in the thesis; and

iii. the sum of all co-author contributions is equal to 100% less the candidate's stated contribution.

Name of Co-Author	Chaoshui Xu		
Contribution to the Paper	Supervised the research and reviewed the manuscript.		
Signature		Date	18/02/2019

Name of Co-Author	Murat Karakus		
Contribution to the Paper	Supervised the research and reviewed the manuscript.		
Signature		Date	18/02/2019

Name of Co-Author	Jiayi Shen		
Contribution to the Paper	Supervised the research and reviewed the manuscript.		
Signature		Date	18/02/2019

Abstract

Damage accumulation in the rock mass leading to failure is influenced by the properties of pre-existing discontinuities. In order to simulate rock mass behaviour realistically, many damage models have been proposed. Amongst them, limited damage models consider joint orientation, one of the significant properties of discontinuities impacting the rock mass failure, in the strongly anisotropic rock masses. In this study, we propose a statistical damage model using a Weibull distribution which takes into account joint orientation by incorporating the Jaeger's and modified Hoek-Brown failure criteria for the jointed rock mass. The proposed statistical damage model is validated using the experimental results. Further, verification of the proposed model is conducted by the *Distinct Element Method using* Particle Flow Code (PFC). To investigate the influence of the shape parameter (m) and scale parameter (F_0) of Weibull distribution on the statistical damage model predictions, a sensitivity analysis is carried out. It is found that the parameter m only depends on strain parameter k. On the other hand, the parameter F_0 is indirectly related to the failure strength of the jointed rock mass in the proposed damage model. The considerable influence of joint stiffness on the damage variable D, damage evolution rate D_r and rock mass responses are also identified.

Keywords: Damage model; Joint orientation; Jointed rock mass; Bonded particle model;

List of symbols:

$P(F)$	The percentage of damaged elements out of the total number of microscopic elements.
F	The element strength parameter depending on the strength criterion used
F_0	Scale parameter of the Weibull distribution
m	Shape parameter or a homogeneous index of Weibull distribution
D	Damage variable
N	The total number of all microscopic elements
n	The number of all failed microscopic elements under a certain loading
σ_i (MPa)	The nominal stress, i = 1, 3
σ_i^* (MPa)	The effective stress, i = 1, 3
ν	Poisson's ratio of the material
ε_1	The strain on the major principal stress direction
σ_{1f} (MPa)	Peak stress at failure
ε_{1f}	Peak strain at failure
c (MPa)	Cohesion
ϕ (˚)	Internal friction angle
c_j (MPa)	Joint cohesion
ϕ_j (˚)	Joint friction angle
β (˚)	Joint orientation
m_i	A material constant of Hoek-Brown
k_0	A constant value related to the cohesion and internal friction angle of the rock

k_β	Anisotropy parameter
E (GPa)	Young's modulus of rock
E_β (GPa)	Deformation modulus of the jointed rock mass
δ (m)	A mean vertical spacing interval in rock that contains a single set of horizontal joints
k_n (GPa)	Joint normal stiffness
k_s (GPa)	Joint shear stiffness
k	Strain parameter
COV (%)	Coefficient of Variation

1 Introduction

The deformation behaviour of rock material is a fundamental topic in rock engineering (Li et al. 2012; Peng et al. 2015). Accurate estimation of rock strength and deformation properties is critical for the stability analysis of rock engineering applications such as rock slope, rock tunnel, underground excavation, etc. In nature, the rock mass consists of intact rock and discontinuities such as bedding planes, joints and cleavages. The strength and the mechanical properties of the rock mass are controlled by the mechanical and geometrical properties of the discontinuities and intact rocks (Yang et al. 1998; Tiwari and Rao 2006; Zhou et al. 2014; Wasantha et al. 2015; Jin et al. 2016; Guo et al. 2017). Therefore, the deformation behaviours of the rock mass can be largely influenced by the geometrical and mechanical properties of joints, especially for anisotropic rock mass.

Many experimental investigations (Donath 1961; Hoek 1964; Mclamore and Gray 1967; Ramamurthy et al. 1988; Yang et al. 1998; Prudencio and Van Sint Jan 2007; Jiang et al. 2014; Chen et al. 2016; Jin et al. 2016) published characterizes deformation properties and failure mechanisms in anisotropic rock masses. The results from these studies indicate that the failure strength and deformation is closely associated with joint orientation or bedding orientation, see Fig. 5.1. The failure strength reaches its maximum value either at $\beta=0^{\circ}$ or $\beta=90^{\circ}$, while its minimum value located around $\beta=45^{\circ}$-60°. Three failure modes are observed in the experimental results (Tien and Tsao 2000): sliding mode along the discontinuity or joint, shearing mode along the intact rock and mixed mode. These laboratory results lay the foundation for failure analysis of the anisotropic rock masses.

Several failure criteria have been proposed to incorporate the effect of joint orientation on the failure behaviour of rock masses. These criteria were generally modified from the classical failure criteria such as the Mohr-Coulomb, the Barton-Bandis, and the Hoek-

Brown as shown in Table 5.1. They provide some effective tools to estimate the strength of anisotropic rock masses. However, it can be challenging to investigate the failure process of geomaterials under complex loading condition in practical engineering (Chen et al. 2012).

Table 5.1 Summary of the failure criteria considering the joint orientation

Original criterion	Modified failure criterion	References
Mohr-Coulomb criterion	Jaeger's criterion	(Jaeger 1959, 1960)
	Variable cohesion and friction angle failure criterion	(McLamore and Gray 1967)
	Tien and Kuo criterion	(Tien and Kuo 2001)
	The plane of patchy weakness theory	(Fjær and Nes 2014)
Barton-Bandies criterion	Duveau and Shao criterion	(Duveau et al. 1998)
	An extended plane of weakness theory	(Halakatevakis and Sofianos 2010)
Hoek-Brown criterion	Colak and Unlu criterion	(Colak and Unlu 2004)
	Saroglou and Tsiambaos criterion	(Saroglou and Tsiambaos 2008)
	Shi's criterion	(Shi et al. 2016)

On the other hand, the damage mechanics becomes an effective way to investigate the failure process and failure behaviours of geomaterials, simulating the initiation, propagation and coalescence of microcracks from a microscopic perspective (Hoek and Martin 2014). Two damage models, including continuum damage model (CDM)(Ortiz 1985; Chow and Wang 1987; Kawamoto et al. 1988; Halm and Dragon 1998; Swoboda et al. 1998; Cauvin and Testa 1999; Dragon et al. 2000; Pituba and Fernandes 2011; Kishta et al. 2017; Richard et al. 2017) and micromechanical model (Shao et al. 2005; Zhu et al. 2008; Chen et al. 2012), are widely used to describe the anisotropic behaviours of the rock mass. Due to easily implementation and convenient for field applications, the continuum damage model (CDM) was explained by many researchers. In CDM, the damage tensors, in most cases, were used to describe the anisotropic behaviours of rock masses. Kawamoto et al. (1988) and Swoboda et al. (1998) adopted the second-order damage tensor to reflect the anisotropy

due to the pre-existing joints in the jointed rock mass. However, in strongly anisotropic materials, these models do not correctly describe the failure modes: shear failure in intact rock matrix and sliding failure along the joint and thus they may underestimate the strengths of the rock masses (Liu and Yuan 2015). Recently, Liu and Yuan (2015) proposed a coupled damage model which includes the shear strength of the macroscopic joint. However, as pointed Liu and Yuan (2015), the effect of joint stiffness on the deformability of the rock mass was ignored. Inspired by these studies, a new damage model considering joint orientation is proposed in this study.

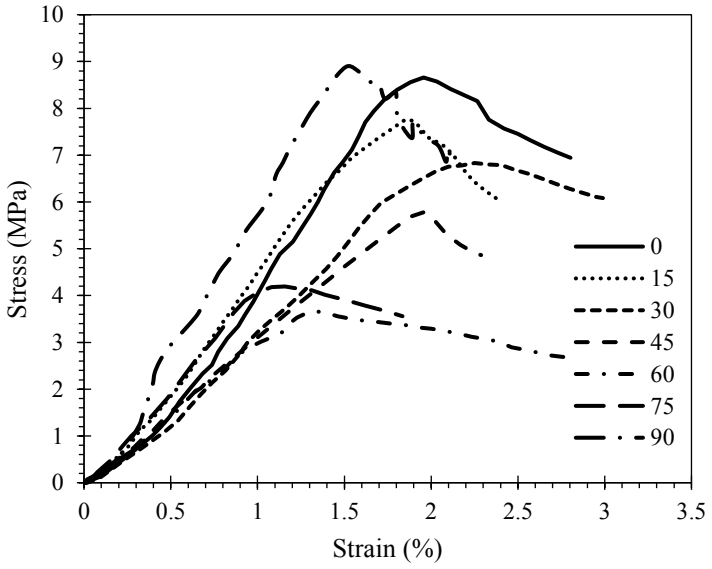

Figure 5.1 Behaviour of rock like materials with different joint orientation (after Jin et al. 2016)

In this paper, a new statistical damage model for a rock mass considering joint orientation is derived based on Weibull distribution. Fundamentals of the statistical damage model and its derivation are explained in section 2. Validation and verification of the proposed damage model are presented in section 3. Particle Flow Code used for verification is also explained

in section 3. Finally, a sensitivity analysis for the damage distribution parameters and rock mass response is carried out in section 4.

2 Statistical damage model

2.1 Damage model development

Conceptually, a rock is composed of a large number of microscopic elements. When the rock is subjected to external loading, microscopic elements will fail and defects or micro-cracks are created, which then they coalesce to form macro-cracks. This is basically the damage accumulation process taking place in the rock as a response to external load. Statistically, the strength of these microscopic elements can follow a certain type of distribution with the most commonly suggested ones as power function distribution and Weibull distribution. Therefore, a statistical approach may better describe the mechanical behaviour of rocks from a micro level (Deng and Gu 2011). As stated in Section 1, the damage model based on the statistical damage theory is widely used to investigate different mechanical behaviours, such as softening and hardening behaviours (Cao et al. 2010) and thermal-mechanical behaviours (Xu and Karakus 2018). However, very limited research has been done on modelling anisotropic characteristics such as strength and deformability of jointed rocks using the statistical damage theory.

The Weibull distribution used to describe the distribution of the strength of microscopic elements in the damage model can be written as:

$$P(F) = \frac{m}{F_0}\left(\frac{F}{F_0}\right)^{m-1} exp\left[-\left(\frac{F}{F_0}\right)^{m}\right] \tag{5.1}$$

where F is the element strength parameter depending on the failure criterion used, which can be regarded as stress level when strength criterion (Zhou et al. 2017) used or strain when maximum strain criterion (Liu and Yuan 2015) adopted; m is the shape parameter or

a homogeneous index of Weibull distribution; F_0 is the scale parameter of the Weibull distribution.

Assuming N is the number of all microscopic elements within the rock and n denotes the number of failed microscopic elements under a certain external load, the damage variable D (between 0 and 1) can be directly defined as (Tang and Kaiser 1998):

$$D = \frac{n}{N} \tag{5.2}$$

When the stress level F increases to F+dF, the number of failed microscopic elements increases by $NP(F)$dF. If all microscopic elements are subjected to the same local stress F, the total number of failed microscopic elements n can be calculated as:

$$n = N\int_0^F P(F)dF = N\left\{1 - exp\left[-\left(\frac{F}{F_0}\right)^m\right]\right\} \tag{5.3}$$

i.e., the damage variable D can be expressed as:

$$D = 1 - exp\left[-\left(\frac{F}{F_0}\right)^m\right] \tag{5.4}$$

To define the mechanical damage for rock material, the concept of effective stress (σ_i^*), i.e., the stress acting on the undamaged area of the rock material, is used to represent the nominal stress (σ_i). According to the strain equivalent principle, the strain induced by σ_i on the whole material is equal to the strain induced by σ_i^* on the undamaged material. Therefore, two effective stresses (σ_1^*, σ_3^*) of the rock mass can be expressed using nominal stresses (σ_1, σ_3) under biaxial compression:

$$\sigma_i^* = \sigma_i/(1 - D) \tag{5.5}$$

with i = 1, 3.

According to the generalized Hooke's law and the damage, the strain can be expressed as:

$$\varepsilon_1 = \frac{1}{E}(\sigma_1^* - \nu\sigma_3^*) = \frac{1}{E(1-D)}(\sigma_1 - \nu\sigma_3) \tag{5.6}$$

where ν is the Poisson's ratio of the material. Substituting Equation (5.4) into Equation (5.6), the stress-strain relationship is obtained on the major principal stress direction:

$$\sigma_1 = E\varepsilon_1 exp\left[-\left(\frac{F}{F_0}\right)^m\right] + \nu\sigma_3 \tag{5.7}$$

As an example to demonstrate this model, the damage variable *D,* *E*=50 GPa, $\sigma_3 = 0$ MPa and F_0=0.01 with maximum strain criterion were adopted here and the results are plotted in Fig. 5.2 for different *m* values. As can be seen, a higher value of *m* corresponds to narrower distribution of the element strengths, hence greater variation in damage variable *D* against strain and a sharper decrease of the stress after the peak load. In other words, when *m* value is increased, the rock behaves in a more brittle fashion, and its strength increases accordingly.

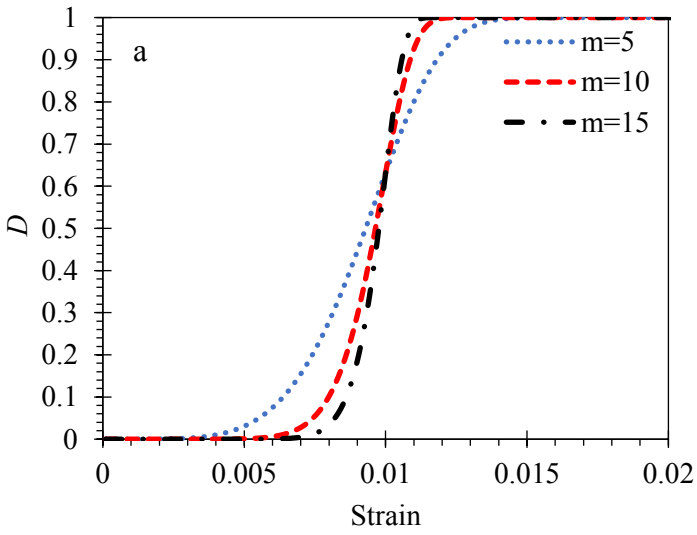

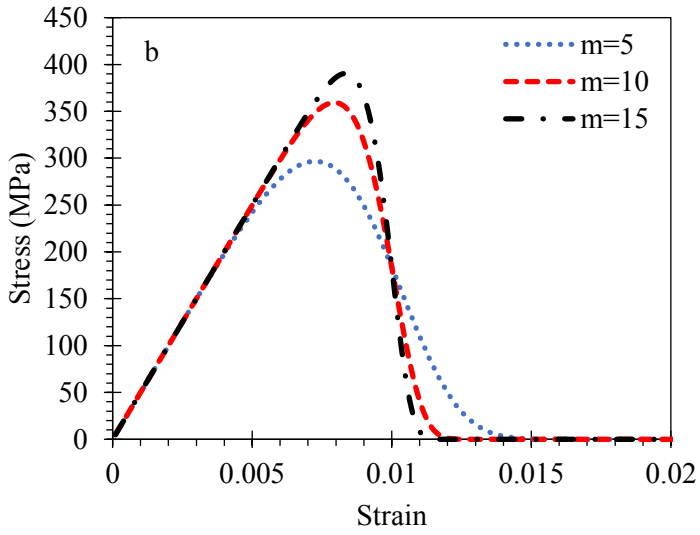

Figure 5.2 Microscopic damage variable and the strength of the intact rock: (a) damage variable vs. strain, (b) corresponding stress-strain response

Next, the strength of microscopic elements must be determined. As shown in Fig. 5.2, the maximum strain criterion can be used to describe the microscopic element strength. However, it could not reflect the influence of complicated stress state of the microscopic element. Therefore, many studies (Deng and Gu 2011; Li et al. 2012; Xu and Karakus 2018) tried to consider the rock failure criterion for a microscopic element in stress space and proposed new expressions for the microscopic element. In general, the failure criterion of the microscopic element can be expressed in the following form:

$$f(\sigma^*) - k_0 = 0 \tag{5.8}$$

where k_0 is a constant value related to the cohesion and internal friction angle of the rock. $F = f(\sigma^*) = \frac{f(\sigma)}{1-D}$ reflects the strength of microscopic element, depending on the failure criteria adopted in the damage model.

Rearranging Equation (5.6), one can obtain:

$$1 - D = \frac{(\sigma_1 - \nu\sigma_3)}{E\varepsilon_1} \tag{5.9}$$

Then substituting Equation (5.9) in Equation (5.8), the following equation can be obtained:

$$F = \frac{f(\sigma)}{\sigma_1 - \nu\sigma_3} E\varepsilon_1 \tag{5.10}$$

To derive the rock mass response and calculate damage variable *D*, the damage parameters m and F_0 should be determined. In this process, the 'Extremum method' was used in previous studies (Cao et al. 2010; Deng and Gu 2011), where the peak point of the measured stress-strain curve can be used. At the peak point, the derivative of σ_1 with corresponding ε_1 should be zero, i.e.:

$$\varepsilon_1 = \varepsilon_{1f}, \sigma_1 = \sigma_{1f} \tag{5.11}$$

$$\frac{d\sigma_1}{d\varepsilon_1} = 0 \tag{5.12}$$

where σ_{1f} and ε_{1f} are stress and strain corresponding to the peak point. Based on the Equation (5.12), one can obtain:

$$m\varepsilon_1 \left(\frac{F}{F_0}\right)^{m-1} \frac{1}{F_0} \frac{dF}{d\varepsilon_1} = 1 \tag{5.13}$$

From Equation (5.9), one can easily obtain the following equation:

$$\frac{dF}{d\varepsilon_1} = \frac{f(\sigma)}{\sigma_1 - \nu\sigma_3} E = \frac{F}{\varepsilon_1} \tag{5.14}$$

Then the distribution parameter *m* and F_0 can be calculated by substituting Equations (5.13) and (5.11) into Equation (5.7):

$$m = \frac{1}{ln\left(\frac{E\varepsilon_{1f}}{\sigma_{1f} - \nu\sigma_3}\right)} \tag{5.15}$$

$$F_0 = \sqrt[m]{m}F_f, \varepsilon_1 = \varepsilon_{1f} \tag{5.16}$$

2.2 Implementation of failure criteria into the proposed damage model

Appropriate failure criterion should be determined for the microscopic elements in the damage model (Xu and Karakus 2018). Due to the pre-existing joint, the commonly used failure criteria should be modified to account the influence of joint orientation. Two failure criteria including Jaeger's criterion and Hoek-Brown criterion are discussed in this section.

2.2.1 Jaeger's Failure criterion

We used the Jaeger's failure criterion to derive the damage parameters for the Weibull damage model:

$$\sigma_1 = \begin{cases} \dfrac{1+sin\phi}{1-sin\phi}\sigma_3 + \dfrac{2c\,cos\phi}{1-sin\phi}, & \beta < \phi_j \; or \; \beta = 90° \\ \sigma_3 + \dfrac{2c_j + 2\sigma_3 tan\phi_j}{sin2\beta\left(1 - tan\phi_j tan\beta\right)}, & \phi_j \le \beta < 90° \end{cases} \tag{5.17}$$

where c and ϕ are cohesion and internal friction angle of the rock; c_j and ϕ_j are joint cohesion and friction angle, respectively, and β is the joint orientation (the angle of the joint from the plane perpendicular to the loading direction). Then the strength of microscopic element in stress space can be expressed in the following Equation:

$$\begin{cases} F_1 = \dfrac{\sigma_1 - \dfrac{1+sin\phi}{1-sin\phi}\sigma_3}{\sigma_1 - \nu\sigma_3} E\varepsilon_1, & \beta < \phi_j \; or \; \beta = 90° \\ F_2 = \dfrac{\sigma_1 - \left[1 + \dfrac{2tan\phi_j}{sin2\beta\left(1 - tan\phi_j tan\beta\right)}\right]\sigma_3}{\sigma_1 - \nu\sigma_3} E\varepsilon_1, & \phi_j \le \beta < 90° \end{cases} \tag{5.18}$$

We can derive the stress-strain relationship by substituting Equation (5.18) into Equation (5.7):

$$\sigma_1 = \begin{cases} E\varepsilon_1 exp\left[-\left(\frac{F_1}{F_0}\right)^m\right] + \nu\sigma_3, \beta < \phi_j \; or \; \beta = 90° \\ E\varepsilon_1 exp\left[-\left(\frac{F_2}{F_0}\right)^m\right] + \nu\sigma_3, \qquad \phi_j \leq \beta < 90° \end{cases} \tag{5.19}$$

where F_1 and F_2 are the expression of microscopic strength derived in Equation (5.18).

2.2.2 Modified Hoek-Brown criterion

Here, the modified Hoek-Brown model proposed by Saroglou and Tsiambaos (2008) incorporating the anisotropic parameter k_β of rock mas is used:

$$\sigma_1 = \sigma_3 + \sigma_c \left(k_\beta m_i \frac{\sigma_3}{\sigma_c} + 1\right)^{0.5} \tag{5.20}$$

where m_i is a Hoek-Brown constant, depending on the rock type (texture and mineralogy)(Shen and Karakus 2014), σ_c is the uniaxial compressive strength of the intact rock. Then failure strength of microscopic element using the Hoek-Brown criterion can be expressed in the following equation:

$$F = \frac{\sqrt{(\sigma_1 - \sigma_3)^2 - k_\beta m_i \sigma_c \sigma_3}}{\sigma_1 - \nu\sigma_3} E\varepsilon_1 \tag{5.21}$$

Accordingly, the stress-strain relationship can be expressed as:

$$\sigma_1 = E\varepsilon_1 exp\left[-\left(\frac{\frac{\sqrt{(\sigma_1 - \sigma_3)^2 - k_\beta m_i \sigma_c \sigma_3}}{\sigma_1 - \nu\sigma_3} E\varepsilon_1}{F_0}\right)^m\right] + \nu\sigma_3 \tag{5.22}$$

2.3 Damage model implementation

In order to implement the proposed damage model for further analysis, the basic material parameters such as cohesion (c), internal friction angle (ϕ), joint cohesion (c_j), joint

friction angle (ϕ_j), joint orientation (β) should be identified first. Then the failure stress σ_{1f}, deformation modulus E_β, and failure strain ε_{1f} should be determined to derive the damage distribution parameters *m* and F_0. We can estimate the failure stress σ_{1f} from Equation (5.17) and (5.20). However, the deformation modulus E_β of the jointed rock mass is influenced by the joint orientation, which can be estimated through the following equation (Gao et al. 2016):

$$\frac{1}{E_\beta} = \frac{1}{E} + cos^2\beta\left(\frac{cos^2\beta}{\delta k_n} + \frac{sin^2\beta}{\delta k_s}\right) \tag{5.23}$$

where δ is a mean vertical spacing interval in rock that contains a single set of joints, k_n and k_s are the normal stiffness and shear stiffness on the weak planes, respectively. On the other hand, the failure strain ε_{1f} is related to the failure stress σ_{1f} and the deformation modulus E_β:

$$\varepsilon_{1f} \propto \frac{\sigma_{1f}}{E_\beta} \tag{5.24}$$

Due to the existing crack closure and unstable crack growth stages, the failure strain is larger than $\frac{\sigma_{1f}}{E_\beta}$. Therefore, to better estimate the failure strain, a strain parameter k is introduced here, and the failure strain can be estimated using the following Equation:

$$\varepsilon_{1f} = (1 + k)\frac{\sigma_{1f}}{E_\beta} \tag{5.25}$$

where *k* depends on the plastic strain of the material, which will be discussed in Section 4.

The implementation procedure for the proposed damage model is summarized as follows:

(1) Obtain the basic material parameters: rock cohesion c, internal friction angle ϕ, joint cohesion c_j, joint friction angle ϕ_j and joint orientation β for the damage

model incorporating Jaeger's criterion; anisotropic parameter k_β and Hoek –Brown constantm_i for the damage model incorporating the modified Hoek-Brown criterion;

(2) Estimate failure stress σ_{1f}, deformation modulus E_β and failure strain ε_{1f} through Equations (5.17) or (5.20), (5.23) and (5.25), respectively;

(3) Obtain damage distribution parameters m and F_0 through Equations (5.15) and (5.16);

(4) Substitute damage distribution parameters m and F_0 into Equation (5.17) or (5.22) to obtain the stress-strain response.

3 Validation and verification of the proposed damage model

3.1 Validation of the proposed damage model

To validate the proposed damage model, the damage model is applied to a group of published experimental data on jointed basalt (Jin et al. 2016) using modified Hoek-Brown criterion. The results of the damage model, obtained from Equation (5.7), with different joint orientation is presented in Fig. 5.3, and the corresponding experimental results are also shown for comparison purpose. One can see that the proposed model is capable of describing the main deformation and strength properties of the jointed rock mass, especially the pre-peak region. However, the rock mass responses from the proposed damage model cannot capture the rock compaction characteristics in the initial stage of rock mass response when joint orientation $< 30^\circ$.

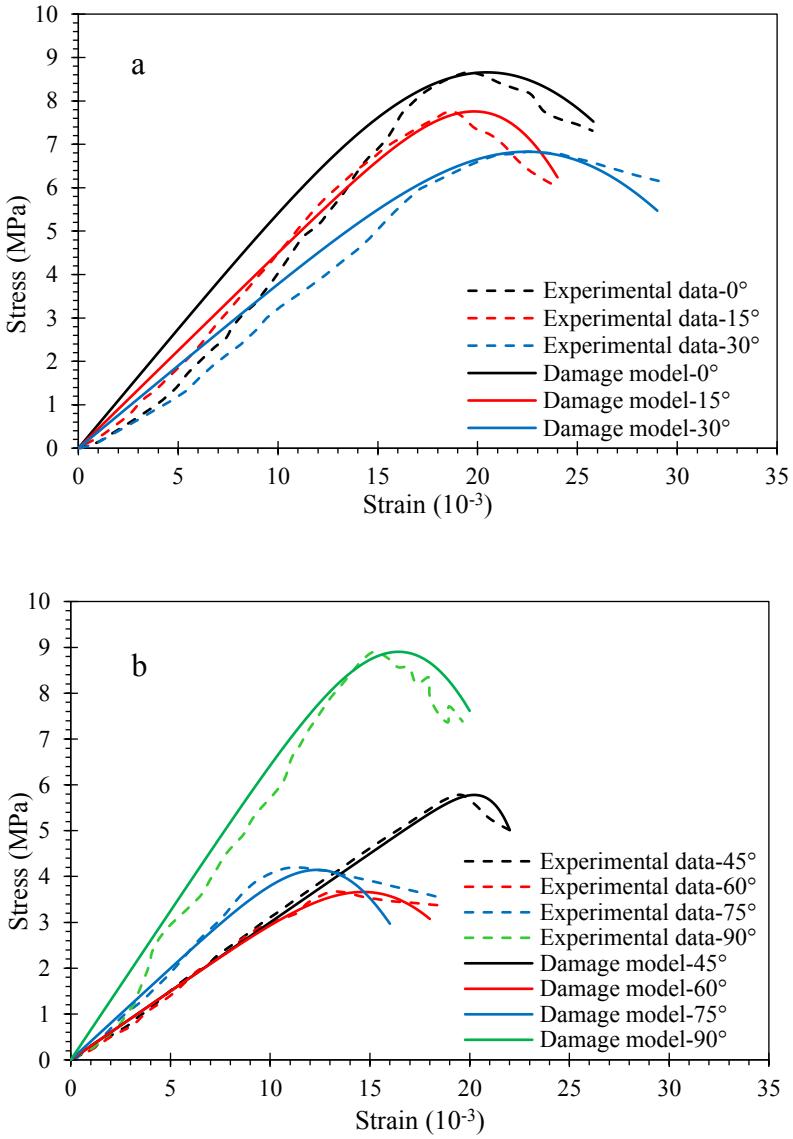

Figure 5.3 Comparison of the proposed damage model and experimental results (Jin et al. 2016) for the jointed rock mass with various joint orientation: (a) Joint orientation 0˚, 15˚ and 30˚; (b) Joint orientation 45˚, 60˚, 75 ˚ and 90˚.

3.2 Verification of the proposed damage model by PFC

The proposed damage model is verified by comparison of the stress-strain response of a rock mass from the proposed model and results obtained from the bonded particle model, PFC in this study. The synthetic rock mass (SRM) model consists of two components to represent intact rock and discontinuities (Mas Ivars et al. 2011). Intact rock can be

represented by bonded particle model (BPM) (Potyondy and Cundall 2004) material which is non-uniform circles or particles assembly connected through contacts. For the current study, the flat joint model (FJM) is employed to simulate a more realistic intact rock, especially for brittle rocks (Vallejos et al. 2016). On the other hand, smooth joint model (SJM) is implemented into the flat joint contacts to represent joint in PFC.

3.2.1 Intact rock representation

In this study, the Hawkesbury sandstone was chosen for the verification study. A rectangular numerical model of 54mm×108mm containing random non-uniform particles assembly was subjected to uniaxial compression tests to obtain macro-properties for calibration. The loading rate is set to small enough (0.02 m/s) to ensure the quasi-static loading condition (Zhang and Wong 2013, 2014).

The PFC parameters calibrated using experimental data reported by Wasantha et al. (2013), and are given in Table 5.2. A good agreement between experimental and PFC model results was achieved, where the coefficient of variation (COV) was found to be less 1%. The calibrated micro-parameters for Hawkesbury sandstone are summarized in Table 5.3. Fig. 5.4 shows the intact rock response of UCS tests conducted in PFC.

Table 5.2 Mechanical properties of Hawkesbury sandstone (Wasantha et al. 2013) and calibrated BPM material

Macro-properties	UCS, MPa	TS, MPa	E, GPa	υ
Experimental results	50.80	4.00	11.00	0.20
PFC results	50.17	4.08	11.02	0.21
COV (%)	0.51	1.40	0.13	0.70

Table 5.3 Basic calibrated micro-parameters for Hawkesbury sandstone

Groups	Micro-parameters	Description	value
Microstructure parameters	w/d	Ratio of specimen width to the average ball diameter	60
	r_{max}/r_{min}	Ratio of maximum to minimum ball radius	1.66
	g_0	Installation-gap ratio	4e-2
	n_p	Porosity	0.16
	N_r	Number of elements	3
FJM Constitutive	E^*(GPa)	Bond modulus	11.40
	k^*	Stiffness ratio	2.5
	μ	Friction coefficient	0.77
	t_b (MPa)	Bond tensile strength	7.10
	c_b (MPa)	Bond cohesion	28.20
	Φ_b (degree)	Bond friction angle	25

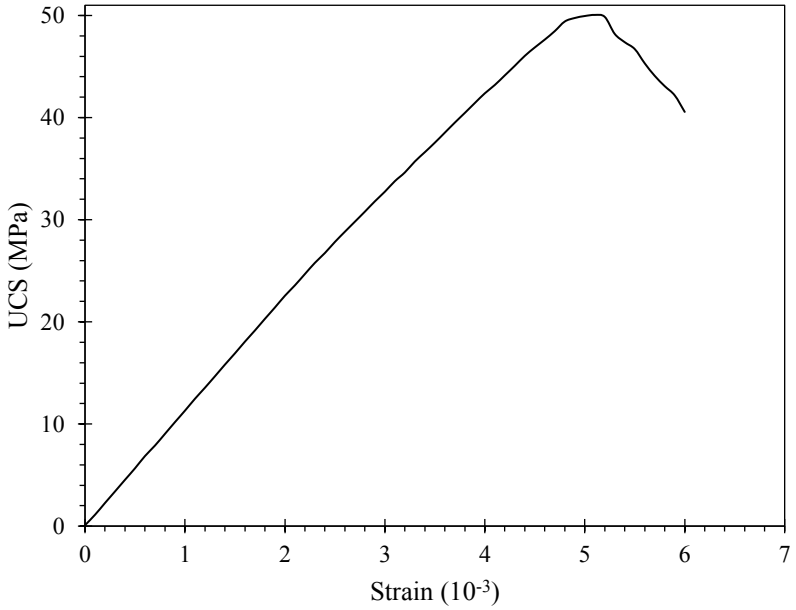

Figure 5.4 Intact rock behaviour under uniaxial compression in PFC

3.2.2 Joint representation

To simulate the behaviour of the joint within a rock mass, the smooth joint contact model was proposed by Pierce et al. (2007) and explored in detail by Mas Ivars et al. (2008). The smooth joint model provides the behaviour of a planar interface with dilation regardless of

the local particle contact orientations along the interface. The two particles using smooth joint contact model may slide past each other instead of moving around each other of FJM.

Generally, these macro-properties include normal stiffness, shear stiffness, cohesion and friction angle, and are governed by smooth joint micro-parameters such as bond normal stiffness, bond shear stiffness, bond cohesion and friction angle at the particle level. Bahaaddini et al. (2013) proposed a two-stage calibration procedure: normal deformability test for normal stiffness calibration and direct shear test for the shear stiffness and coefficient of friction calibration, and using the ISRM suggested method (Ulusay 2014) (see Fig. 5.5).

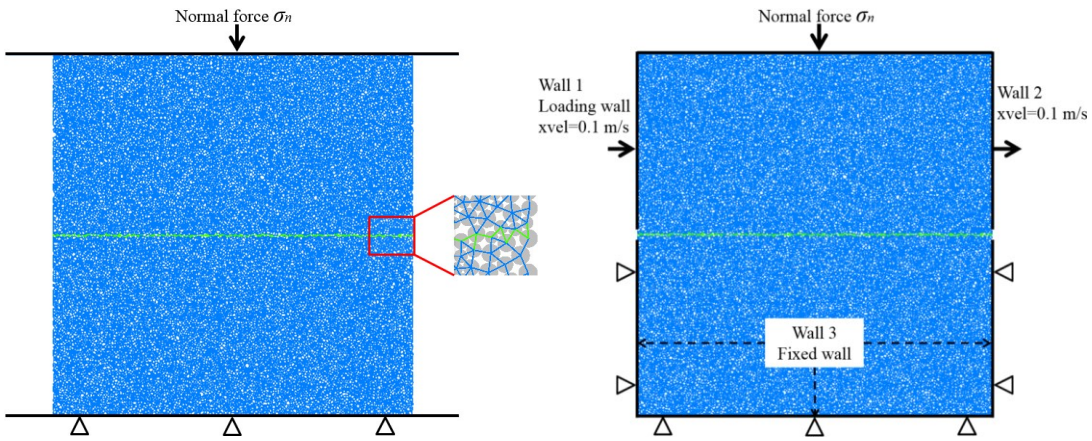

Figure 5.5 Calibration of smooth-joint microparameters for PFC analysis (a) uniaxial compression test and (b) direct shear test

In this study, normal stiffness and shear stiffness are set large to minimise their effect on mechanical properties and the only direct shear test was carried out to match the cohesion and friction angle of Hawkesbury sandstone, which is 2.2 MPa and 32˚. The corresponding calibrated cohesion and joint friction angle are 2.19 MPa and 31.79˚, respectively. And the calibrated micro-parameters for the smooth-joint model are summarized in Table 5.4.

Table 5.4 Calibrated micro-parameters for the smooth-joint model

Calibrated micro-parameters	Normal stiffness (GPa/m)	Shear stiffness (GPa/m)	Friction angle (°)	Cohesion (MPa)	Tensile strength (MPa)
Value	800	200	32	2.20	1

3.2.3 Simulation of a single jointed rock mass by PFC

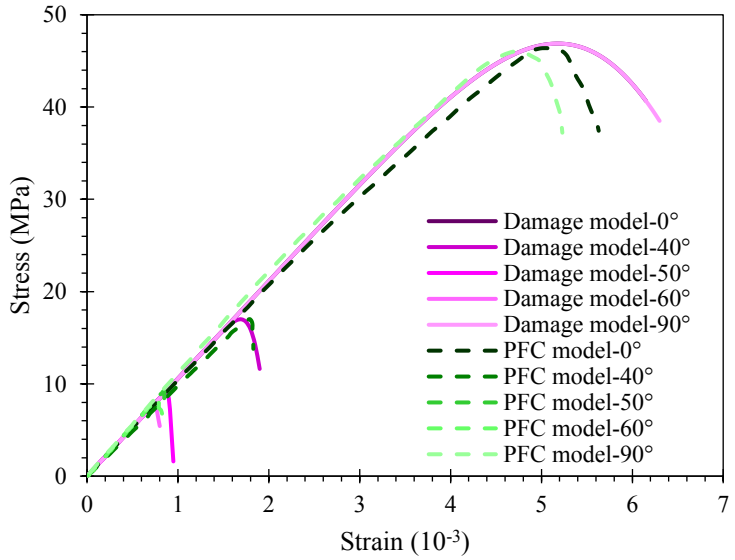

Figure 5.6 Comparison of the proposed damage model and PFC model predictions and proposed damage model for the jointed rock mass with various joint orientation

In order to verify the proposed damage model, the PFC models with different joint orientations using 0º, 40º, 50º, 60º, 90º are subjected to the uniaxial compression tests using Jaeger's criterion. The comparison of the proposed Weibull damage model and the results from the PFC analysis are shown in Fig 5.6.

The failure stress of rock mass model when joint orientation $\beta = 0^{\circ}$ drops to 46.88 MPa, which is consistent with the experimental results (Wasantha et al. 2013) when one persistent joint exists in the intact specimen. The comparison shows that the proposed damage model is in a great agreement with the PFC results at both the pre-peak and post-peak regions. As can be seen from Figure 5.6, the proposed damage model can capture the stress-strain response better at pre-peak region than the post-peak region.

4 Sensitivity analysis of damage distribution parameters and the damage variables and rock mass response

The damage variables in the proposed damage model are largely influenced by the joint orientation based on the analysis presented in section 2. Taking the stress-strain in the direction of the major principal strain as an example, we considered $E = 11.00$ GPa, $\sigma_{(90)} = 46.88$ MPa, $\sigma_3 = 0.00$MPa, $\nu = 0.20$, k =0.2, $c_j = 6.00$ MPa and $\phi_j = 0^{\circ}$as the reference parameters for sensitivity analysis.

4.1 Damage distribution parameters

4.1.1 Damage distribution parameter *m*

As mentioned in Section 2, the damage distribution parameter *m* is an indicator of material brittleness: more brittle as the damage distribution parameter *m* becomes larger. Substituting Equation (25) into Equation (15), we can see that the damage distribution parameter only depends on parameter *k*:

$$m = \frac{1}{ln(1+k)} \tag{5.26}$$

The result (see Fig. 5.7), shows that damage distribution parameter *m* is nonlinear and indirectly proportional to the strain parameter *k* for the jointed rock mass. As the parameter *k* is directly proportional to the increase of the failure strain, we confirm that the material

becomes more brittle as the failure strain becomes smaller. The parameter k should be carefully chosen according to the material brittleness when the failure strain data is not available.

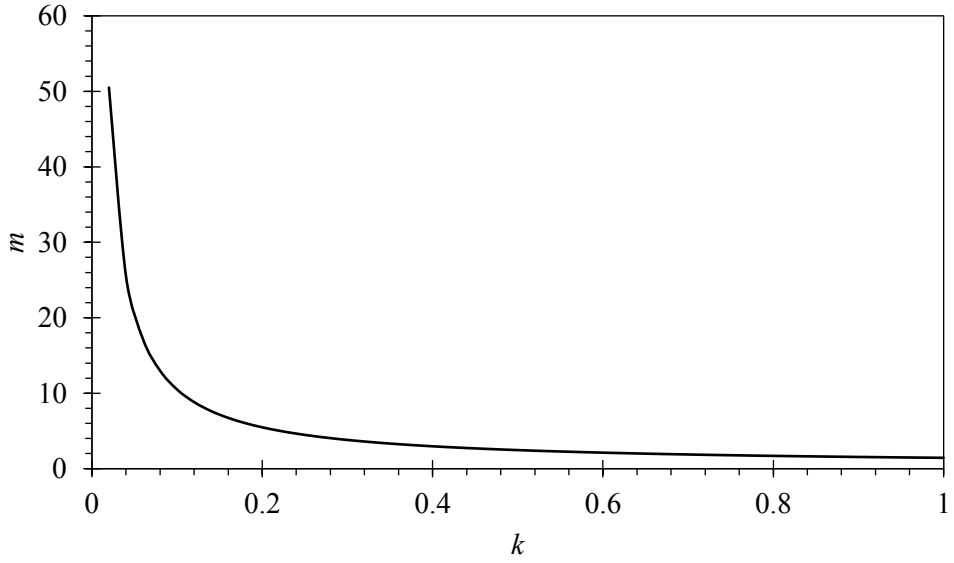

Figure 5.7 Damage distribution parameter m versus parameter k

4.1.2 Damage distribution parameter F_0

The influence of the model parameters listed as the reference parameters previously on the damage distribution parameter F_0 is analysed by changing one of the corresponding parameters and leaving the other parameters constant.

The effects of confining stress, joint cohesion and joint friction angle on the damage distribution parameter F_0 is demonstrated in the Fig. 5.8 (a), Fig. 5.8 (b) and Fig. 5.8 (c), respectively. The results show that the damage distribution parameter F_0 follows the 'U' shape with various joint orientation, reaching the minimum value when joint orientation equals to $45° + \phi_j/2$.

The confining stress can increase the level of damage distribution parameter as confining stress increases from 0 to 20 MPa, see Fig. 5.8 (a). However, it has a larger influence on F_0 when joint orientation $\beta = 0^\circ$ and $\beta = 90^\circ$ but less influence when joint orientation $0^\circ < \beta < 90^\circ$. This is due to the fact that two failure modes occur: shear failure when joint orientation $\beta = 0^\circ$ and $\beta = 90^\circ$ and sliding failure when joint orientation $0^\circ < \beta < 90^\circ$.

The joint cohesion effect on F_0 is investigated by increasing cohesion from 2 to 10 MPa, see Fig. 5.8 (b). The maximum value of F_0 is independent with different joint cohesion as the maximum failure strength keeps unchanged with a certain confining condition. On the other hand, the joint cohesion can increase the values of F_0 when it is less than the maximum value of F_0. As joint cohesion increases, the gradually reaches to the maximum value of F_0 from the model with smaller and larger joint orientation.

The joint friction angle effect on F_0 is analysed by varying from 0˚ to 40˚, see Fig. 5.8 (c). Similarly, the joint friction angle has no influence on the maximum value of F_0. The interval of 'U' shape narrows from smaller joint orientation as joint friction angle increases. At the same time, the joint friction angle can increase the value of F_0 when it is less than the maximum value. Overall, the F_0 can be regarded as a strength parameter, indirectly related to the failure strength of the jointed rock masses.

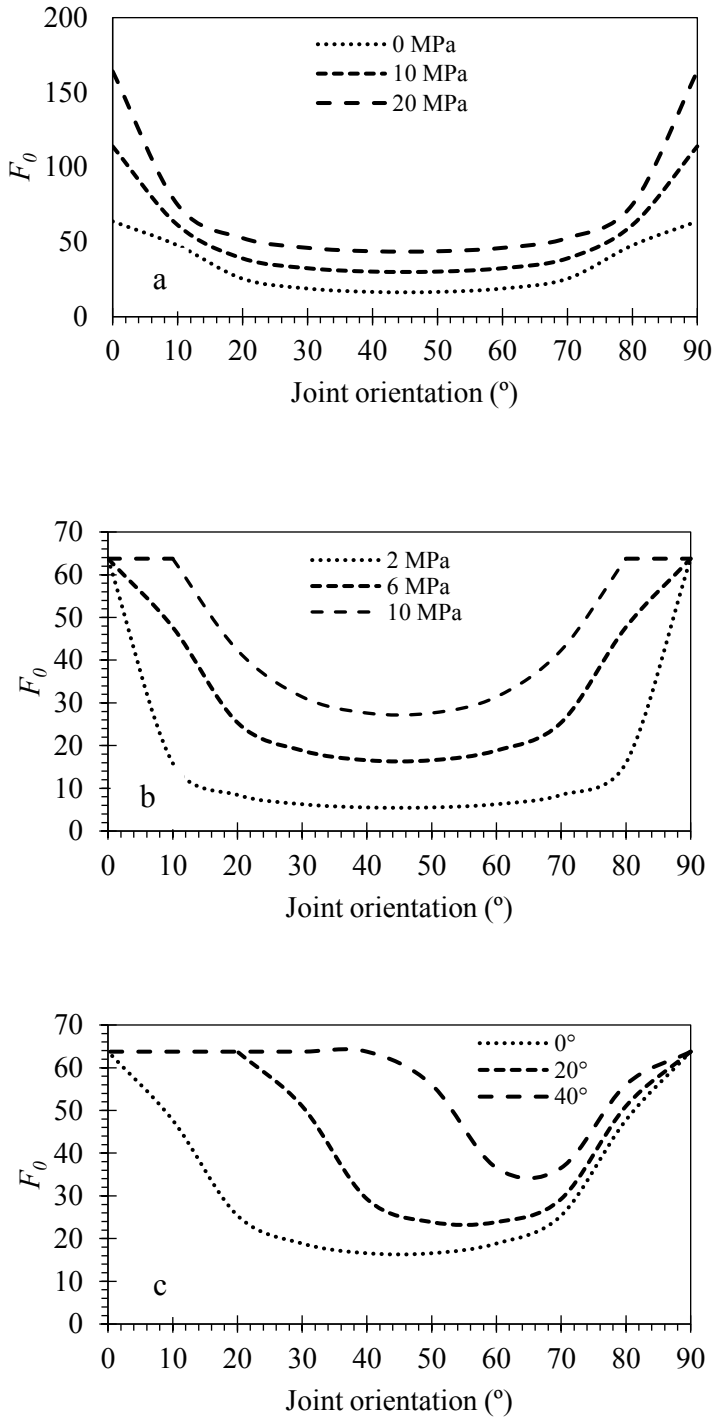

Figure 5.8 Influence of (a) confining stress (b) cohesion (c) Joint friction angle on the damage distribution parameter F_0

4.2 Influence of joint stiffness on the damage variable and rock mass response

Based on derived damage distribution parameters m and F_0, the rock mass response will be influenced by the joint orientation. However, as pointed out earlier in Section 2.3, the joint stiffness may have effects on the rock mass response, which was ignored by the previous studies (Liu and Yuan 2015; Zhang et al. 2015).

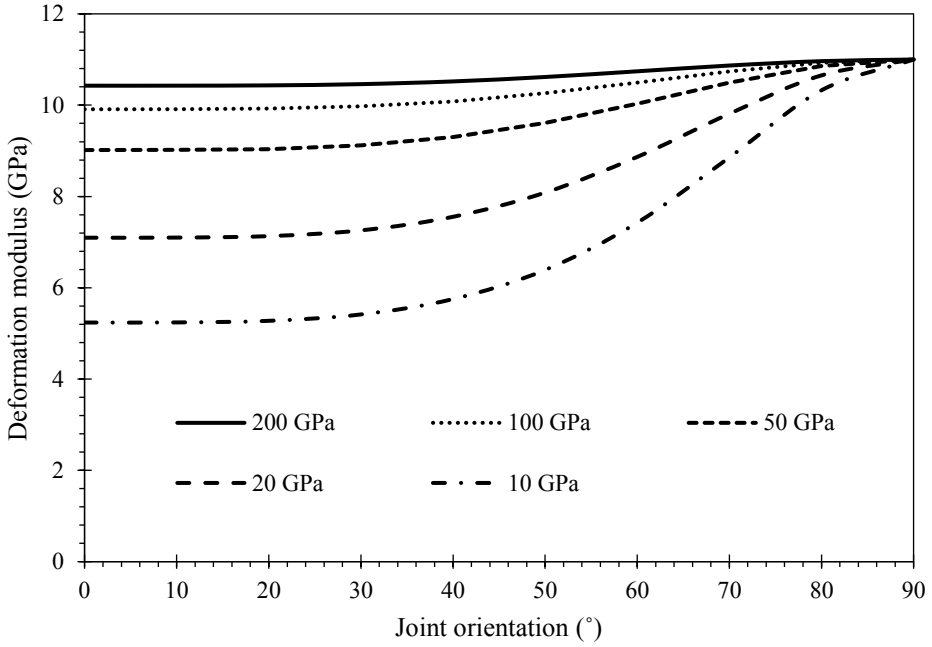

Figure 5.9 Influence of Joint stiffness on the deformation modulus of the rock masses

Invoking Equation (23), the deformation modulus of the rock masses varies with joint orientation. When the δ and stiffness ratio (normal stiffness/shear stiffness) is set to 1 m and 0.5, respectively, we plot the deformation modulus versus joint orientation as the normal stiffness increases from 10 GPa to 200 GPa, see Fig. 5.9. The results show that the deformation modulus decreases as the joint becomes weaker. The joint stiffness has a larger influence on the deformation modulus when the jointed rock mass with small joint orientation than those with larger joint orientation, even has no influence when the joint orientation equals to 90°.

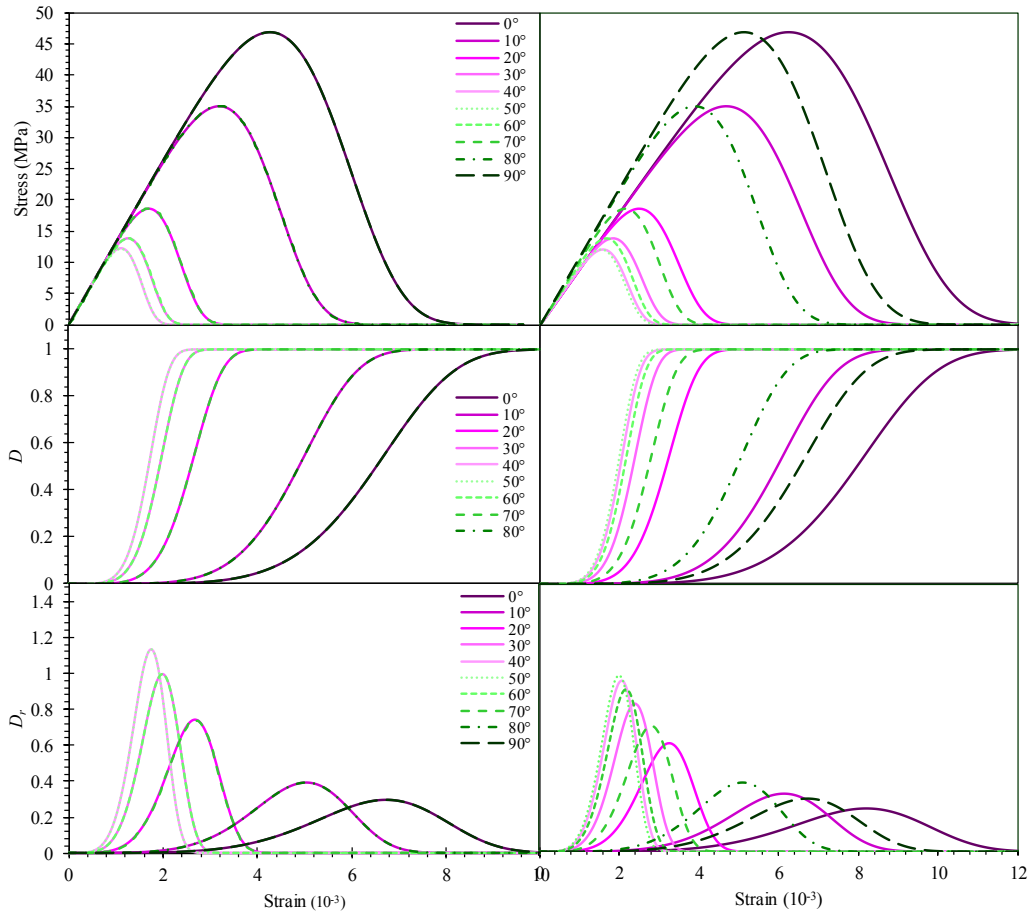

Figure 5.10 Influence of joint stiffness on rock mass response, damage variable D and damage evolution rate D_r for rock masses with different joint orientation: without joint stiffness (left) and with joint stiffness (right)

To better investigate the joint stiffness effect, based on the theoretical analysis, using the references parameters, the rock mass response, damage variable D and damage evolution rate D_r curves with and without considering the joint stiffness are plotted in Fig. 5.10. When the joint stiffness effect on the D, D_r, and rock mass response is ignored, the deformation modulus of the jointed rock mass equals to Young's modulus of intact rock. The results reveal that all the damage variable D, damage evolution rate D_r and rock mass response curves of the model with 0˚, 10˚, 20˚, 30˚, 40˚ overlap with those models with 90˚, 80˚, 70˚,

60˚, 50˚, respectively. The failure strength varies with varying joint orientation when deformation modulus kept constant. The damage variable D curve becomes steeper and the starting damage point appears earlier as joint orientation approaching 40˚ and 50˚. Correspondingly, the maximum value of D_r becomes smaller as joint orientation approaching 40˚ and 50˚.

The joint normal stiffness is set to 50 GPa when considering the joint stiffness. One can easily see that the deformation modulus varies from the stress-strain curves, consisting of the experimental results given in Section 3.1. The results demonstrate that damage variable D curve becomes steeper and the starting point of damage variable D appears earlier as the joint stiffness increases. Additionally, the peak value of damage evolution rate D_r becomes larger with increasing joint stiffness. Therefore, the proposed damage model considering joint stiffness can better capture the deformation and strength behaviours compared with the damage model without considering joint stiffness.

5 Conclusions

In this paper, we proposed a new damage model which uses the Jaeger's and modified Hoek-Brown criteria. The damage distribution parameters m and F_0 were modified to reflect the effect of joint orientation on the rock mass failure behaviour. This way, we can simulate the jointed rock mass behaviours with various joint orientation realistically. Additionally, the deformation modulus variation caused by the joint stiffness can be considered in the damage model by introducing the deformation modulus from Equation (5.23). Based on this research, the following conclusions are obtained:

(1) The shape parameter m was only related to the introduced strain parameter k, reflecting the brittleness of the anisotropic rock mass;

(2) The damage variable D and rock mass response demonstrated an anisotropic characteristic for the damage models with various joint orientation. The damage variable and stress-strain curves for models with 0˚, 10˚, 20˚, 30˚, 40˚ overlapped with those models with 90˚, 80˚, 70˚, 60˚, 50˚, respectively, when joint stiffness was ignored in the proposed damage model.

(3) The proposed damage model improves the prediction of rock mass response significantly, thus the proposed model can be used to simulate anisotropic rock mass behaviour accurately.

Acknowledgement

The PhD scholarship provided by the China Scholarship Council (CSC) to the first author is gratefully acknowledged.

References

Bahaaddini M, Sharrock G, Hebblewhite BK (2013) Numerical direct shear tests to model the shear behaviour of rock joints. Comput Geotech 51:101–115.

Cao W, Zhao H, Li X, Zhang Y (2010) Statistical damage model with strain softening and hardening for rocks under the influence of voids and volume changes. Can Geotech J 47:857–871.

Cauvin A, Testa RB (1999) Damage mechanics: Basic variables in continuum theories. Int J Solids Struct 36:747–761.

Chen L, Shao JF, Zhu QZ, Duveau G (2012) Induced anisotropic damage and plasticity in initially anisotropic sedimentary rocks. Int J Rock Mech Min Sci 51:13–23.

Chen YF, Wei K, Liu W, Hu SH, Hu R, Zhou CB (2016) Experimental characterization and micromechanical modelling of anisotropic slates. Rock Mech Rock Eng 49:3541–3557.

Chow CL, Wang J (1987) An anisotropic theory of continuum damage mechanics for ductile fracture. Eng Fract Mech 27:547–558.

Colak K, Unlu T (2004) Effect of transverse anisotropy on the Hoek-Brown strength parameter “mi” for intact rocks. Int J Rock Mech Min Sci 41:1045–1052.

Deng J, Gu D (2011) On a statistical damage constitutive model for rock materials. Comput Geosci 37:122–128.

Donath F (1961) Experimental study of shear failure in anisotropic rocks. Geol Soc Am Bull 72:985–990.

Dragon A, Halm D, Désoyer T (2000) Anisotropic damage in quasi-brittle solids:

Modelling, computational issues and applications. Comput Methods Appl Mech Eng 183:331–352.

Duveau G, Shao JF, Henry JP (1998) Assessment of some failure criteria for strongly anisotropic geomaterials. Mech Cohesive-Frictional Mater 3:1–26.

Fjær E, Nes OM (2014) The impact of heterogeneity on the anisotropic strength of an outcrop shale. Rock Mech Rock Eng 47:1603–1611.

Gao C, Xie LZ, Xie HP, He B, Jin WC, Li F, Yang ZP, Sun YZ (2016) Estimation of the equivalent elastic modulus in shale formation: theoretical model and experiment. J Pet Sci Eng 151:468–479.

Guo S, Qi S, Zhan Z, Zheng B (2017) Plastic-strain-dependent strength model to simulate the cracking process of brittle rocks with an existing non-persistent joint. Eng Geol 231:114–125.

Halakatevakis N, Sofianos AI (2010) Strength of a blocky rock mass based on an extended plane of weakness theory. Int J Rock Mech Min Sci 47:568–582.

Halm D, Dragon A (1998) An anisotropic model of damage and frictional sliding for brittle materials. Eur J Mech A/Solids 17:439–460.

Hoek E (1964) Fracture of anisotropic rock. J South African Inst Min Metall 64:501–518

Hoek E, Martin CD (2014) Fracture initiation and propagation in intact rock – A review. J Rock Mech Geotech Eng 6:287–300.

Jaeger JC (1959) The frictional properties of joints in rock. Pure Appl Geophys 43:148–158.

Jaeger JC (1960) Shear failure of anisotropic rocks. Geol Mag 97:65–72.

Jiang Q, Feng XT, Hatzor YH, Hao XJ, Li SJ (2014) Mechanical anisotropy of columnar jointed basalts: An example from the Baihetan hydropower station, China. Eng Geol 175:35–45.

Jin C, Li S, Liu J (2016) Anisotropic mechanical behaviors of columnar jointed basalt under compression. Bull Eng Geol Environ 77:1–14.

Kawamoto T, Ichikawa Y, Kyoya A (1988) Deformation and fracturing behaviour of discontinuous rock mass and damage mechanics theory. Int J Numer Anal Methods Geomech 12:1–30.

Kishta E, Richard B, Giry C, Ragueneau F (2017) Strong discontinuity analysis of a class of anisotropic continuum damage constitutive models – Part II: Concrete material application. Mech Res Commun 86:27–31.

Li X, Cao W, Su Y (2012) A statistical damage constitutive model for softening behavior of rocks. Eng Geol 143–144:1–17.

Liu H, Yuan X (2015) A damage constitutive model for rock mass with persistent joints considering joint shear strength. Can Geotech J 52:1136–1143.

Ivars DM, Pierce ME, Darcel C, Reyes-Montes J, Potyondy DO, Young RP, Cundall PA (2011) The synthetic rock mass approach for jointed rock mass modelling. Int J Rock Mech Min Sci 48:219–244.

Mas Ivars D, Potyondy D, Pierce M, Cundall P (2008) The smooth-joint contact model. In: Proceedings of WCCM8-ECCOMAS, 2008, 8th. Venice, Italy.

Mclamore R, Gray KE (1967) The mechanical behavior of anisotropic sedimentary rocks. J Eng Ind 89:62–73.

Ortiz M (1985) A constitutive theory for the inelastic behavior of concrete. Mech Mater 4:67–93.

Peng J, Rong G, Cai M, Zhou CB (2015) A model for characterizing crack closure effect of rocks. Eng Geol 189:48–57.

Pierce M, Cundall P, Potyondy D, Mas Ivars D (2007) A synthetic rock mass model for jointed rock. In: Meeting Society's Challenges and Demands, 1st Canada-US Rock Mechanics Symposium, Vancouver. pp 341–349.

Pituba JJC, Fernandes GR (2011) Anisotropic damage model for concrete. J Eng Mech 137:610–624.

Potyondy DO, Cundall PA (2004) A bonded-particle model for rock. Int J Rock Mech Min Sci 41:1329–1364.

Prudencio M, Van Sint Jan M (2007) Strength and failure modes of rock mass models with non-persistent joints. Int J Rock Mech Min Sci 44:890–902.

Ramamurthy T, Rao G, Singh J (1988) A strength criterion for anisotropic rocks. In: Fifth Australia-New Zealand Conference on Geomechanics. pp 253–257. Institution of Engineers, Australia.

Richard B, Kishta E, Giry C, Ragueneau F (2017) Strong discontinuity analysis of a class of anisotropic continuum damage constitutive models – Part I: Theoretical considerations. Mech Res Commun 86:32–36.

Saroglou H, Tsiambaos G (2008) A modified Hoek-Brown failure criterion for anisotropic intact rock. Int J Rock Mech Min Sci 45:223–234.

Shao JF, Ata N, Ozanam O (2005) Study of desaturation and resaturation in brittle rock

with anisotropic damage. Eng Geol 81:341–352.

Shen J, Karakus M (2014) Simplified method for estimating the Hoek-Brown constant for intact rocks. J Geotech Geoenvironmental Eng 140:04014025.

Shi X, Yang X, Meng Y, Li G (2016) Modified Hoek–Brown failure criterion for anisotropic rocks. Environ Earth Sci 75:1–11.

Swoboda G, Shen XP, Rosas L (1998) Damage model for jointed rock mass and its application to tunnelling. Comput Geotech 22:183–203.

Tang CA, Kaiser PK (1998) Numerical simulation of cumulative damage and seismic energy release during brittle rock failure—part I: fundamentals. Int. J. Rock Mech. Min. Sci. 35:113–121.

Tien YM, Kuo MC (2001) A failure criterion for transversely isotropic rocks. Int J Rock Mech Min Sci 38:399–412.

Tien YM, Tsao PF (2000) Preparation and mechanical properties of artificial transversely isotropic rock. Int J Rock Mech Min Sci 37:1001–1012.

Tiwari RP, Rao KS (2006) Post failure behaviour of a rock mass under the influence of triaxial and true triaxial confinement. Eng Geol 84:112–129.

Ulusay R (2014) The ISRM suggested methods for rock characterization, testing and monitoring: 2007-2014. Springer.

Vallejos JA, Salinas JM, Delonca A, Mas Ivars D (2016) Calibration and verification of two bonded-particle models for simulation of intact rock behavior. Int J Geomech 17:06016030.

Wasantha PLP, Ranjith PG, Viete DR (2013) Specimen slenderness and the influence of

joint orientation on the uniaxial compressive strength of singly jointed rock. J Mater Civ Eng 26:06014002.

Wasantha PLP, Ranjith PG, Zhang QB, Xu T (2015) Do joint geometrical properties influence the fracturing behaviour of jointed rock? An investigation through joint orientation. Geomech Geophys Geo-Energy Geo-Resources 1:3–14.

Xu XL, Karakus M (2018) A coupled thermo-mechanical damage model for granite. Int J Rock Mech Min Sci 103:195–204.

Yang ZY, Chen JM, Huang TH (1998) Effect of joint sets on the strength and deformation of rock mass models. Int J Rock Mech Min Sci 35:75–84.

Zhang L, Hou S, Liu H (2015) A uniaxial compressive damage constitutive model for rock mass with persistent joints considering the joint shear strength. Electron J Geotech Eng 20:5927–5941.

Zhang XP, Wong LNY (2013) Loading rate effects on cracking behavior of flaw-contained specimens under uniaxial compression. Int J Fract 180:93–110.

Zhang XP, Wong LNY (2014) Choosing a proper loading rate for bonded-particle model of intact rock. Int J Fract 189:163–179.

Zhou C, Xu C, Karakus M, Shen J (2018) A systematic approach to the calibration of micro-parameters for the flat-jointed bonded particle model. Geomech Eng 16:471–482.

Zhou SW, Xia CC, Zhao HB, Mei SH, Zhou Y (2017) Statistical damage constitutive model for rocks subjected to cyclic stress and cyclic temperature. Acta Geophys 65:893–906.

Zhou Y, Wu SC, Gao YT, Misra A (2014) Macro and meso analysis of jointed rock mass triaxial compression test by using equivalent rock mass (ERM) technique. J Cent

South Univ 21:1125–1135.

Zhu Q, Kondo D, Shao J, Pensee V (2008) Micromechanical modelling of anisotropic damage in brittle rocks and application. Int J Rock Mech Min Sci 45:467–477.

Chapter 6 Conclusions and Recommendations for Further Work

6.1 Conclusions and summary

The current thesis presents a systematic study of the anisotropy characteristics of the jointed rock mass at both static and dynamic conditions. After a brief introduction of the anisotropic jointed rock mass and critical review of current literature, a serious of studies have been carried out to achieve the aims listed in the introduction section. In the following section, the overall conclusions are summarized:

1. Based on the dimensionless analysis, sensitivity analysis, regression analysis and numerical simulation results, four relationships were setup between micro-parameters of FJM and the macro-rock properties such as uniaxial compressive strength (UCS), tensile strength (TS), Young's modulus (E) and Poisson's ratio (v). These relationships provide an effective tool to determine the micro-parameters for the flat-joint BPM without going through the time-consuming trial-and-error process using the traditional approach. After the structural parameters (such as N_r , n, r_{max}/r_{min} and w/d) are determined, k^* should be determined first based on the Poisson's ratio v. E^* is then determined to match the Young's modulus E of the rock material. t is derived based on the tensile strength TS of the rock, and finally, c is determined to match the rock uniaxial compressive strength UCS.
2. Based on the simulation results and previous experimental data, the bonded particle model (BPM) was demonstrated to be capable of modelling the strain rate-dependent mechanical properties and behaviours of rock materials. These mechanical properties

include uniaxial compressive strength, fragmentation characteristic and the features of micro-cracking within the rock specimen.

3. BPM was used further in this study to investigate the dynamic behaviours of jointed rocks. A dynamic strength relationship was established for a rock mass with a persistent joint based on numerical simulation results, which can be used to predict the dynamic UCS of the rock mass with a joint at different orientations. The results indicated that the dynamic behaviour of a jointed rock is more sensitive to the strain rate when tensile and shearing failure modes within the part of intact rock are more dominant, corresponding to cases when the joint is at low or high angles with respect to the principal loading direction.
4. A new damage model was proposed by incorporating Jaeger's criterion and modified Hoek-Brown criterion. The damage distribution parameters m and F_0 were modified to reflect the effects of joint orientation on the rock mass failure behaviours. The shape parameter m was only related to the introduced strain parameter k, which is directly proportional to the increase of the failure strain. The proposed damage model can be used to model the anisotropic behaviour of jointed rock masses. In addition, the effects of the joint stiffness on the deformation modulus of the jointed rock can also be considered in the proposed damage model. The damage model considering the joint stiffness can better capture the deformation and strength of the jointed rock compared with that without considering the joint stiffness.
5. In the proposed damage model, the damage variable D and stress-strain curve show significant anisotropic characteristics for the rocks with different joint orientations. The damage variable and stress-strain curve for rocks with joint orientations at 0˚, 10˚, 20˚, 30˚, 40˚ are identical to those at 90˚, 80˚, 70˚, 60˚, 50˚, respectively, when the joint stiffness was ignored in the damage model.

6.2 Recommendations for future work

Although the results in this study give more insights of the mechanical behaviours of anisotropic rock masses, there are limitations. Recommendations for further studies are summarized below:

1. The systematic calibration approach proposed in Section 3 mainly focused on two-dimensional bonded particle model under uniaxial compression condition to match the uniaxial compressive strength (UCS), tensile strength (TS), Young's modulus (E) and Poisson's ratio (ν), however, the intrinsic mechanical properties such as cohesion and internal friction angle may not match. Therefore, a calibration procedure under triaxial compression condition in three dimensional highly recommended in the future study.
2. The study should be extended to cover jointed rocks with more than one fractures, perhaps randomly distributed.
3. Current study only deals with jointed rocks with a persistent joint. An obvious extension is to cover the mechanical behaviours of jointed rocks containing a non-persistent joint, which remains a challenging task, both theoretically and numerically.
4. The proposed damage model only considers the jointed rock mass with persistent joints. To model the mechanical behaviours of jointed rocks with random cracks, it may become necessary to incorporate the geological strength index (GSI) into the model.
5. In the current study, the joint roughness is only indirectly considered through the joint friction angle in the numerical model. However, in practical applications, it may be necessary to consider the joint surface profile and surface roughness explicitly so a model more closely reflecting the mechanical behaviour of joints can be obtained.